FERMILAB-THESIS-2025-15

Measurement of the Triple-Differential Cross Section of Muon Neutrino Charged Current Interactions with Low Hadronic Activity in the NOνA Near Detector

by
James R. Lesmeister

A Dissertation submitted to the Department of Physics,
College of Natural Sciences and Mathematics
in partial fulfillment of the requirements for the degree of

Doctor of Philosophy
in Physics

Chair of Committee: Lisa Koerner

Committee Member: Daniel Cherdack

Committee Member: Rene Bellwied

Committee Member: Ricardo Vilalta

University of Houston
December 2025

ACKNOWLEDGMENTS

To my father, who was the finest Physics teacher I've ever had. To my grandmother, who helped with the construction of Fermilab. To my mother who provided for me. To my family in Illinois who took care of me while I studied at Fermilab.

ABSTRACT

This dissertation describes the analysis and measurement of the triple-differential cross-section of the $\nu_\mu CC$ interaction with Low Hadronic Activity (maximum kinetic energy of 250 MeV for protons and 175 MeV for pions) in the NOvA Near Detector. This cross-section is reported in bins of Muon Kinematics and available hadronic energy. The data corresponds to an accumulated 14.2×10^{20} protons-on-target (POT) in the neutrino mode of the NuMI beam, with a narrow band of neutrino energies peaked at 1.8 GeV. The analysis provides a sample of neutrino–nucleus interactions with an enhanced fraction of quasi-elastic (QE) and two-particle-two-hole (2p2h) interactions and a suppression of resonant pion production (RES) and deep inelastic scattering (DIS) interactions. This enhancement of QE and 2p2h allows for quantitative comparisons with various models of these processes. We find strong disagreement between data and theory-based models in the forward muon direction, especially for the 0.2-0.4 GeV available hadronic energy region.

TABLE OF CONTENTS

LIST OF TABLES

LIST OF FIGURES

1 Neutrinos

A neutrino is a point particle with extremely low mass and neutral electric charge that only interacts via the Weak Nuclear Force.

1.1 Neutrino History

In the 1930s, a problem arose in the study of β^- decay, that is decay where a parent nucleus emits an electron (the β^- particle) and becomes a slightly lighter nucleus:

$$A \to B + e^- \tag{1}$$

Unlike α decay (where a positive particle is emitted) or γ decay (where a photon is emitted), which follow two-body decay dynamics, β^- decay acted differently.

In two body decays, the outgoing energies are kinematically determined in the center of mass frame so that if parent particle "A" is at rest and daughter particles "B" and "e" (in the case of β^- decay, the electron) have equal and opposite momentum (due to conversation of momentum), then conservation of energy dictates that the energy of the electron "E" is given by:

$$E = \left(\frac{m_A^2 - m_B^2 + m_e^2}{2m_A} \right) c^2 \tag{2}$$

where E is fixed and only dependent on the masses of the particles [1]. However, experiments were carried out and this value E represented the maximum energy value of the electron, whose actual energy could vary [1].

Wolfgang Pauli proposed the idea that an additional particle was emitted alongside the electron: a particle that was neutral in charge, to conserve total charge in the decay, that carried off energy so that the total energy was conserved [1]. He called this invisible neutral particle the "neutron" [1].

In 1933, Enrico Fermi incorporated Pauli's proposed particle in his theory of β^- decay, giving it the name "neutrino" (as James Chadwick used the name neutron the previous year) [1]. With

modern information this theory becomes:

$$n \rightarrow p^{+} + e^{-} + \overline{\nu_e} \tag{3}$$

where the bar indicates it's an antiparticle and the "e" indicates the flavor, but at the time neutrino anti-particles and flavors had yet to be discovered.

A group lead by C. F. Powell discovered the decay of the pion to a muon:

$$\pi \rightarrow \mu + \nu \tag{4}$$

and subsequently the decay of a muon to an electron:

$$\mu \rightarrow e + 2\nu \tag{5}$$

where the variable energy of the electron produced led to the conclusion of there being two neutrinos in the muon decay, just as the original β^{-} decay problem led to the idea of the neutrino to begin with [1].

Experimental evidence of the neutrino would come in the 1950's. Clyde Cowan and Frederick Reines conducted an experiment at the Savannah River nuclear reactor in South Carolina [1]. They studied the inverse beta-decay reaction:

$$\overline{\nu} + p^{+} \rightarrow n + e^{+} \tag{6}$$

They set up a large tank of water and watched for this reaction to occur; they calculated the antineutrino flux to be 5×10^{13} particles per square centimeter per second, but only expected two or three events per hour [1]. However, they were able to measure the outgoing positrons, providing confirmation of the neutrino's existence [1].

Raymond Davis Jr. and Don Harmer would measure whether or not neutrinos and antineutrinos were the same particle by measuring whether or not the following two reactions occurred at about

the same rate:

$$\nu + n \rightarrow p^+ + e^- \tag{7}$$

$$\overline{\nu} + n \rightarrow p^+ + e^- \tag{8}$$

They found that the latter reaction did not occur, establishing a distinction between neutrinos and antineutrinos [1]. This discovery, plus the lack of experimental observation of muons decaying to an electron plus a photon (as opposed to the observed decay of a muon to an electron plus two neutrinos) led to the idea of conservation of lepton flavor [1]. That is, that the neutrinos had some property of a corresponding charged lepton (that is $\nu_e \rightarrow e^-, \nu_\mu \rightarrow \mu^-, \nu_\tau \rightarrow \tau^-$ and their corresponding antiparticles), so that the total of number of charged lepton plus the number of corresponding neutrinos must be conserved.

For example in the β^- decay described above, there are initially zero leptons, thus the particles produced (the electron and the electron antineutrino) have opposite lepton flavor so that the final state has the same lepton flavor as the initial state.

1.2 Standard Model

There are four fundamental forces (gravity, strong nuclear force, weak nuclear force, and electromagnetism). The Standard Model of particle physics comprises the unified theory of the electroweak interaction and the strong nuclear force [2]. The strong force, weak force and electromagnetism are mediated by vector bosons [2]. A table of the interactions and their interactions can be seen in Table 1. The vector bosons have spin 1 and either positive or negative parity, which can be seen in the column labeled J^P where J represents spin (intrinsic component of a particles angular momentum [1]) and P represents parity (whether or not the sign of the wave function flips under reflection [2]).

Table 1: Fundamental forces of the standard model (barring gravity) and their exchange particles [2]

Interaction	couples to	Exchange particles(s)	Mass (GeV/c^2)	J^P
strong	color charge	8 gluons (γ)	0	1^-
electromagnetic	electric charge	photon (γ)	0	1^-
weak	weak charge	$W^{\pm}, Z^0$	$\approx 10^2$	1

In addition to the exchange bosons, the known fundamental particles are the quarks and the leptons, all of which are fermions with spin 1/2, grouped into three "families" [2]. A table of the quarks and leptons can be seen in Table 2.

Table 2: The known fundamental particles of the standard model; all are fermions of spin 1/2 [2]

Fermions	Family			Electric Charge	Color	Weak Isospin		Spin
	1	2	3			left handed	right handed	
Leptons	ν_e	ν_μ	ν_τ	0	-	1/2	-	1/2
	e	μ	τ	-1	-	1/2	0	1/2
Quarks	u	c	t	+2/3	r,b,g	1/2	0	1/2
	d	s	b	-1/3	r,b,g	1/2	0	1/2

Each fermion has an associated anti-fermion with the same mass, opposite electric charge, color, and third component of weak isospin [2].

In all three interactions, energy, momentum, angular momentum, charge, color, baryon number and all three lepton numbers (L_e, L_μ, L_τ) are all conserved [2]. The lepton number is the same for a charged lepton and its corresponding neutrino.

The weak force can be divided into two types of interactions, neutral current (NC) and charged current (CC). Neutral current interactions involve the exchange of the Z^0 boson and do not involve the exchange of charge, while the charged current interaction involves the exchange of a $W^{\pm}$ boson and involves the exchange of a charge.

Parity (P) and charge (C) are conserved by the electromagnetic and strong interactions but not by the weak interaction; for the charged-current weak interaction parity violation is maximal [2]. The charged-current couples to only left-handed fermions or right-handed anti-fermions [2]. The neutral-current of the weak interaction is partly parity violating, coupling to both left and right-handed fermions and anti-fermions, but with different strengths [2].

Only the charged current of the weak interaction can change a quark into another type of quark or a lepton into another type of lepton (this analysis will cover the charged current transforming a lepton) [2].

In the Standard Model, neutrinos are massless [3]. However neutrinos were found to evolve in time as they propagate, which necessitates that they have mass. This implies physics that is beyond the Standard Model. The next section covers a phenomena that occurs when neutrinos propagate.

1.3 Solar and Atmospheric Neutrino Measurements

In the 1960s, the Homestake solar neutrino experiment, led by Raymond Davis Jr., discovered a phenomena regarding neutrinos from the sun [3]. Electron neutrinos are released by the sun undergoing nuclear processes, and the Solar Standard Model (SSM) is used to predict the flux of electron neutrinos hitting the Earth from the Sun based on inputs such as the mass, luminosity, radius, surface temperature, age, and surface elemental abundances of the Sun, in addition to knowledge of the rate of nuclear processes in the Sun [3]. The Homestake experiment sought to experimentally measure the flux of the solar neutrinos by measuring occurrences of the reaction $\nu_e + {}^{37}\mathrm{Cl} \rightarrow e^- + {}^{37}\mathrm{Ar}$ [3]. The flux measured from this experiment, however, was about one-third of the flux predicted from the SSM [3]. This became known as the solar neutrino problem.

Atmospheric neutrinos are produced by the decay of pions and kaons that come from the interaction of cosmic rays and nucleons in the Earth's atmosphere [3]. These decays produce all flavors of neutrinos and antineutrinos at a broad range of energies; these neutrinos travel long ranges ($\sim 10\,\mathrm{km} - \sim 10^4\,\mathrm{km}$) [3]. Based on the dominate production modes of the pion and kaon

decays, a ratio of the expected flux of muon and electron neutrinos can be calculated.

The Kamiokande experiment and its successor, the Super-Kamiokande (Super-K) experiment were water-Cherenkov detector based experiments that observed neutrinos using $\nu - e$ elastic scattering (ES): $\nu_x + e^- \rightarrow \nu_x + e^-$ [3]. This procedure occurs for all neutrino flavors, however muon and tau neutrinos only experience the neutral current interaction of the ES, while electron neutrinos can also experience the charge current interaction of the ES. Consequently, electron neutrinos can be expected to interact about six times more than muon or tau neutrinos for the same neutrino flux. The results from both experiments showed a significantly smaller solar neutrino flux compared to theoretical predictions. Super-K observed a solar neutrino flux of $(2.345 \pm 0.014 \pm 0.036) \times 10^6\,\mathrm{cm}^{-2}\mathrm{s}^{-1}$ compared to predictions based on the SSM of $(5.46 \pm 0.66) \times 10^6\,\mathrm{cm}^{-2}\mathrm{s}^{-1}$ [3]. Furthermore, the Kamiokande experiment, measuring interactions of muon neutrinos with nucleons, reported a deficit in the muon neutrino flux of the atmospheric neutrinos, and found that the muon neutrino disappearance had a zenith angle dependence (which meant a dependence on the travel distance of the neutrinos) [3]. In 1998, the Super-K provided a solution to the atmospheric neutrino problem. The zenith angle distribution showed a deficit for upward going events in muon-like interactions compared to downward going events, while no such asymmetry occurred for electron-like interactions [3]. Super-K looked for the appearance of tau neutrinos to support the hypothesis that the disappearance of muon neutrinos was due to transitions from muon to tau neutrinos. The Super-K found evidence of tau neutrino appearance with 4.6σ significance; the OPERA and IceCube experiments would provide definite observations of tau neutrino appearance [3]. This would become evidence of the phenomena called neutrino oscillation which will be explained in the next section.

The Sudbury Neutrino Observatory (SNO) experiment provided measurements that would solve the solar ne problem [3]. The SNO experiment was sensitive to three reactions: neutrino-electron scattering (ES), the charged current neutrino-deuterium interaction $v_e + d \rightarrow e^- + p + p$, and the neutral current neutrino-deuterium interaction $\nu_x + d \rightarrow \nu_x + p + n$ [3]. This last interaction is sensitive to all types of neutrinos with equal chance of occurring for each type of neutrino, therefore comparing the observed number of this type of interaction due to the solar neutrinos compared

to the other interactions [3]. The results of the experiment showed direct evidence for a non-ν_e component of the solar neutrino flux, and the ν_e flux combined with contributions from ν_μ and ν_τ were enough to be consistent with SSM predictions of the neutrino flux [3].

The results from SNO and Super-K became direct evidence of a non-ν_e component in the solar neutrino flux [3]. Together with the results from the reactor experiment KamLAND, the solution of the solar neutrino problem was found to be flavor transitions in the solar matter [3].

1.4 Neutrino Oscillation

Neutrino oscillation is the process in which lepton number is not conserved as neutrinos propagate [3]. For the flavor eigenstates, ν_α, where a charged current (CC) weak interaction will produce charged lepton l_α, they can be written as a superposition of mass eigenstates (ν_i) that govern kinematical processes, which neutrinos propagate through space as, like the following:

$$|\nu_\alpha\rangle = \sum_{i=1}^{n} U_{\alpha i}^{*} \, |\nu_i\rangle$$

where U represents a mixing matrix, and n is the number of light neutrino species [3]. After traveling a distance $L \approx ct$ (for relativistic particles) the state evolves as:

$$|\nu_\alpha(t)\rangle = \sum_{i=1}^{n} U_{\alpha i}^{*} \, |\nu_i(t)\rangle$$

The probability that the charged lepton observed after a weak CC event after the neutrino traveled this distance will be in state l_β so that $\nu_\alpha N \to l_\beta N'$ is:

$$P_{\alpha\beta} = |\, \langle \nu_\beta | \nu_\alpha(t) | \nu_\beta | \nu_\alpha(t) \rangle \,|^2 = |\sum_{i=1}^{n}\sum_{j=1}^{n} U_{\alpha i}^{*} U_{\beta j} \, \langle \nu_j | \nu_i(t) | \nu_j | \nu_i(t) \rangle \,|^2$$

Assuming that $|\nu\rangle$ is a plane wave [3], then:

$$|\nu_i(t)\rangle = e^{-iE_i t}\,|\nu_i(0)\rangle$$

with $E_i = \sqrt{p_i^2 + m_i^2}$, with E_i, p_i and m_i being the energy, momentum and mass of the neutrino mass eigenstate ν_i. For all cases, the neutrinos are highly relativistic so that $p_i \approx p_j \equiv p \approx E$. The neutrino mass state are orthogonal ($\langle\nu_j|\nu_i|\nu_j|\nu_i\rangle = \delta_{ij}$), which leads to an expression for $P_{\alpha\beta}$ of:

$$P_{\alpha\beta} = \delta_{\alpha\beta} - 4\sum_{i<j}^{n} \mathrm{Re}[U_{\alpha i}U_{\beta i}^{*}U_{\alpha j}^{*}U_{\beta j}]\sin^2 X_{ij} + 2\sum_{i<j}^{n} \mathrm{Im}[U_{\alpha i}U_{\beta i}^{*}U_{\alpha j}^{*}U_{\beta j}]\sin 2X_{ij}$$

where X_{ij}

$$X_{ij} = \frac{(m_i^2 - m_j^2)L}{4E} = 1.267\frac{\Delta m_{ij}^2}{\mathrm{eV}^2}\frac{L/E}{m/\mathrm{MeV}}$$

For antineutrinos, the result would be same but $U \to U^*$. This would lead to the real term of $P_{\alpha\beta}$ being the same, but the imaginary term would have opposite sign. This makes the first term the charge-parity conserving term and the latter the charge-parity violating term [3]. For neutrino oscillation experiments, it's important to note that this probability is dependent on the distance traveled and the neutrino energy; controlling these parameters will lead to maximizing the effects of neutrino oscillation.

For the case where $n = 3$, U is a 3x3 matrix. For the case of Majorana neutrinos (where a neutrino is its own antiparticle), U is dependent on six independent parameters: three mixing angles and three phases [3]. For this case the mixing matrix can be parameterized as:

$$U = \begin{bmatrix} 1 & 0 & 0 \\ 0 & c_{23} & s_{23} \\ 0 & -s_{23} & c_{23} \end{bmatrix} \begin{bmatrix} c_{13} & 0 & s_{13}e^{-i\delta_{CP}} \\ 0 & 1 & 0 \\ -s_{13}e^{i\delta_{CP}} & 0 & c_{13} \end{bmatrix} \begin{bmatrix} c_{12} & s_{12} & 0 \\ -s_{12} & c_{12} & 0 \\ 0 & 0 & 1 \end{bmatrix} \begin{bmatrix} e^{i\eta_1} & 0 & 0 \\ 0 & e^{i\eta_2} & 0 \\ 0 & 0 & 1 \end{bmatrix} \tag{9}$$

where $c_{ij} \equiv \cos\theta_{ij}$ and $s_{ij} \equiv \sin\theta_{ij}$. The mixing angles can be taken without loss of generality to be in the first quadrant, and the phases between 0 and 2π. In the case of Dirac neutrinos (where a neutrino and its antiparticle are different) the Majorana phases (η_1 and η_2) can be absorbed into the neutrino states, leaving the mixing matrix as:

$$U = \begin{bmatrix} c_{12}c_{13} & s_{12}c_{13} & s_{13}e^{-i\delta_{CP}} \\ -s_{12}c_{23} - c_{12}s_{13}s_{23}e^{i\delta_{CP}} & c_{12}c_{23} - s_{12}s_{13}s_{23}e^{i\delta_{CP}} & c_{13}s_{23} \\ s_{12}s_{23} - c_{12}s_{13}c_{23}e^{i\delta_{CP}} & -c_{12}s_{23} - s_{12}s_{13}c_{23}e^{i\delta_{CP}} & c_{13}c_{23} \end{bmatrix} \tag{10}$$

This mixing matrix is known as the Pontecorvo-Maki-Nakagawa-Sakata (PMNS) mixing matrix [3].

2 Muon Neutrino Charged Current Interaction

The muon neutrino charged current interaction ($\nu_\mu CC$) with a nucleus occurs when a Muon Neutrino exchanges a charge with an atomic nuclei, and becomes a muon. The neutrino-nucleus charge current interaction has several modes that depend on the amount of momentum transferred to the nucleus. These modes are characterized by their final state particles.

2.1 Neutrino Charged Current Interaction

Neutrinos interact only via the weak nuclear force. The mediators of the weak force are the massive bosons, Z^0 and $W^\pm$ [1]. The charged current (CC) interaction occurs with the exchange of the charged boson $W^\pm$, while the neutral current (NC) interaction occurs with the exchange of the neutral boson Z^0. Figure 1 shows the most basic Feynman diagrams of a neutrino weakly interacting with a nucleus. The charged current interaction shows a neutrino exchange charge with the nucleus and becoming a charged lepton, while the neutral current interaction shows an elastic interaction with the nucleus.

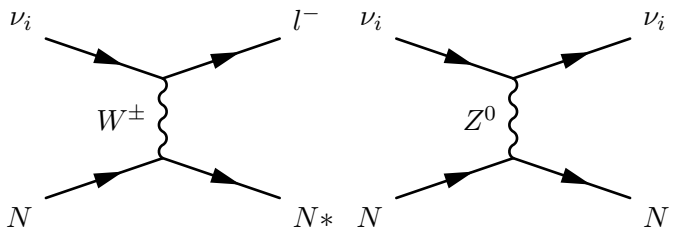

Figure 1: The most basic Feynman diagrams of a neutrino weakly interacting with a nucleus. Left: charged current interaction shows a neutrino exchange charge with the nucleus and becoming a charged lepton. Right: neutral current interaction with an elastic interaction with the nucleus.

2.2 Interaction Modes

The $\nu_\mu CC$ interaction can have different final state particles depending on how much momentum is transferred to the nucleus. The different interaction modes are categorized by their final state particles.

With neutrinos that have less than 2 GeV energy, the neutrino charged current interaction is primarily made of quasi-elastic (QE) interactions [4]. In the QE mode, the neutrinos interact with the whole target nucleon and not with the constituent partons and results in liberating a nucleon from the target [4]. For the muon neutrino QE charged current interaction, the reaction equation looks like:

$$\nu_\mu n \rightarrow \mu^- p \tag{11}$$

A Feynman diagram of the QE interaction can be seen in Figure 2.

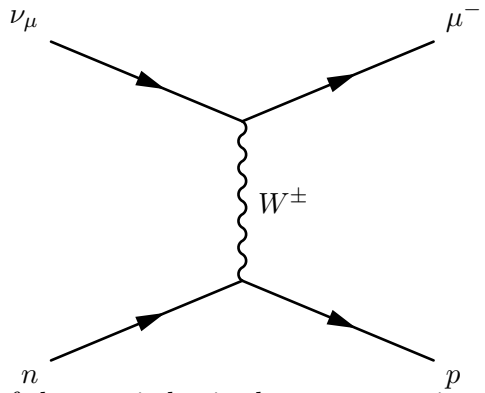

Figure 2: Feynman diagram of the quasi-elastic charge current interaction. In this interaction the neutrino interacts with a single nucleon and generally results in one nucleon being liberated from the target nucleus.

A neutrino can interact with a correlated pair of nucleons, leading to two nucleons getting knocked out of the nucleus, in a process called the 2p2h effect (two particles, two holes) [5]. This primarily occurs by the exchange of a virtual pion, leading to the alternate name meson exchange current (MEC), and is a significant contribution to the total interaction when heavier nuclear targets are used [5]. There are two classes of this interaction mode, depending on with what the boson interacts: in the pion-in-flight class the W boson interacts with the virtual pion being exchanged by the nucleons, while in the contact class the W boson interacts with one of the nucleons [6]. Figures 3 and 4 show Feynman diagrams of the contact class and the pion-in-fight class respectively. Multi-nucleon interactions (more than two nucleons interacting during the neutrino-nucleus interaction) are possible but 2p2h dominates.

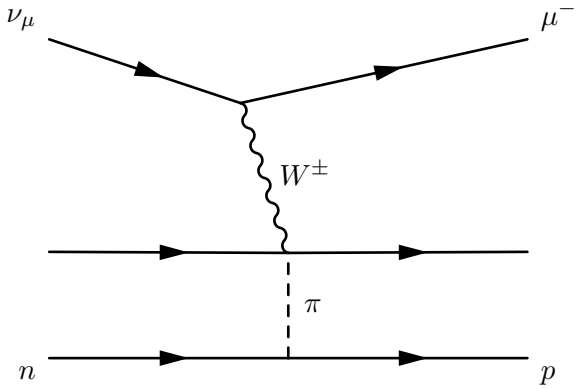

Figure 3: Feynman diagram of the meson exchange current of the $\nu_\mu CC$ interaction with the contact class. In this interaction the neutrino interacts with a pair of correlated nucleons by exchanging a $W^\pm$ boson with one of the nucleons that is exchanging a virtual pion.

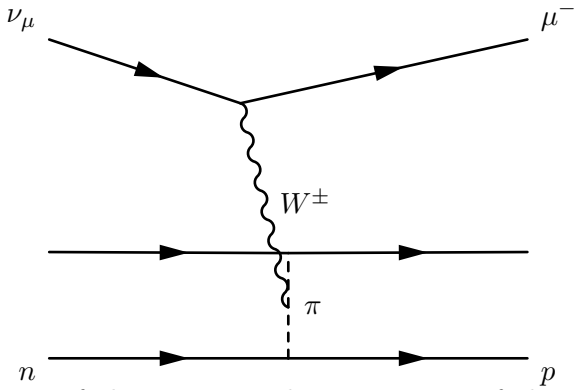

Figure 4: Feynman diagram of the meson exchange current of the $\nu_\mu CC$ interaction with the pion-in-flight class. In this interaction the neutrino interacts with a pair of correlated nucleons by exchanging a $W^\pm$ boson with the virtual pion that is being exchanged by two nucleons.

Neutrinos can excite target nucleons, resulting in a resonant state. The resulting baryonic resonance (Δ) decays to a mesonic state, producing a combination of mesons and nucleons [4]. For a single resonant pion production (referred to here as RES) in the neutrino-nucleus charge current interaction, there are three reaction channels:

$$\nu_\mu p \to \mu^- \pi^+ p \tag{12}$$

$$\nu_\mu n \to \mu^- \pi^0 p \tag{13}$$

$$\nu_\mu n \rightarrow \mu^- \pi^+ n \tag{14}$$

The Feynman diagram, including the intermediate baryon state, can be seen in Figure 5.

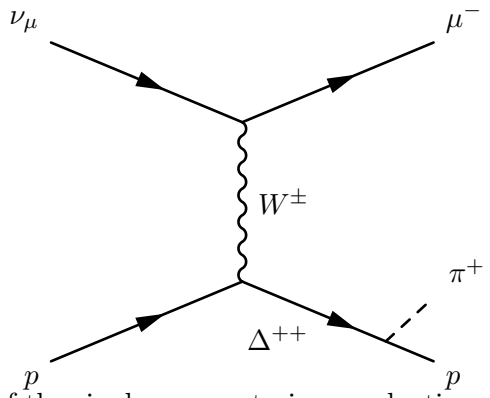

Figure 5: Feynman diagram of the single resonant pion production mode of the $\nu_\mu CC$ Interaction. A nucleon is excited before decaying to a pion and a nucleon.

With enough energy, neutrinos can resolve individual partons of the nucleon. In a process called deep inelastic scattering (DIS), a neutrino will scatter off an individual quark, resulting in a lepton and a hadronic shower in the final state [4]. Both CC and NC processes of DIS are possible, via the exchange of a virtual W or Z boson. Figure 6 shows a Feynman diagram of the DIS interaction mode.

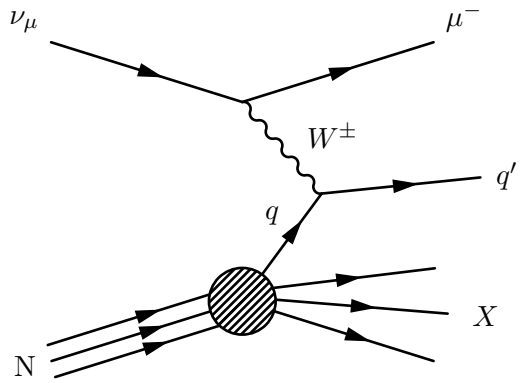

Figure 6: Feynman diagram of the deep inelastic scattering mode of the $\nu_\mu CC$ Interaction. The neutrino has enough energy to scatter off an individual quark, which leads to the nucleus producing a hadronic shower.

2.3 Nuclear Effects

Nuclei are not single particles, but are made of many particles that are capable of interacting with each other. In neutrino-lepton scattering, the neutrino scatters off a point particle. Neutrino-nucleus interactions differ from neutrino-lepton scattering not only due to the target particles not being point particles, but also the influence of particles in the nuclei beyond those the neutrino scatters off of. These are called nuclear effects. MEC, described in the previous section on Interaction modes, is an example of a nuclear effect as it occurs due to interactions between nucleons. This section will go over a couple of these effects that are relevant to this analysis.

A global relativistic Fermi gas (RFG) model is used for the initial state of the nucleus in simulations [7]. Corrections are applied to this model to better match data. One of these corrections is the Random Phase Approximation. The Random Phase Approximation theory (RPA) describes the long-range internucleon interactions [7]; it describes the excitation of many body systems [8]. The effect on the predictions is the suppression of QE events with low four-momentum squared (Q^2) transfer and a slight enhancement of events with high Q^2 transfer. Figure 7 shows the effect of the implementation of RPA on MC predictions.

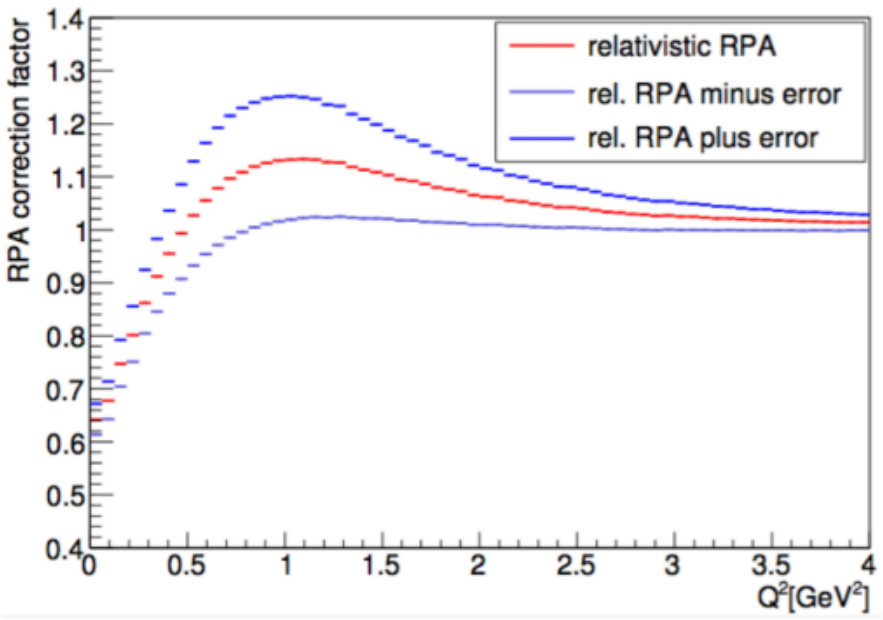

Figure 7: Correction factor on the cross-section predictions of RFG caused by the implementation of RPA, as done by the analysis for the T2K experiment, as a function of Q^2. There is a suppression of events at low Q^2 and a slight enhancement of events at higher Q^2. Image taken from [9]

2.3.1 Final State Interactions

Final state interactions (FSI) occur when the hadronic shower produced from the initial neutrino interaction travels through the dense nuclear matter and re-interacts [10]. FSI can change the energy, angle and charge state of the initially produced hadrons. Figure 8 shows some of the possibilities that can occur with an initially produced pion that lead to various different final states compared to the initially produced pion. This figure assumes that the interaction can be "factorized", that is modeling the neutrino interaction as a two step process where the intermediate boson is absorbed by a hadron followed by hadron rescattering [10]. This picture is justifiable for large enough values of momentum transfer [10].

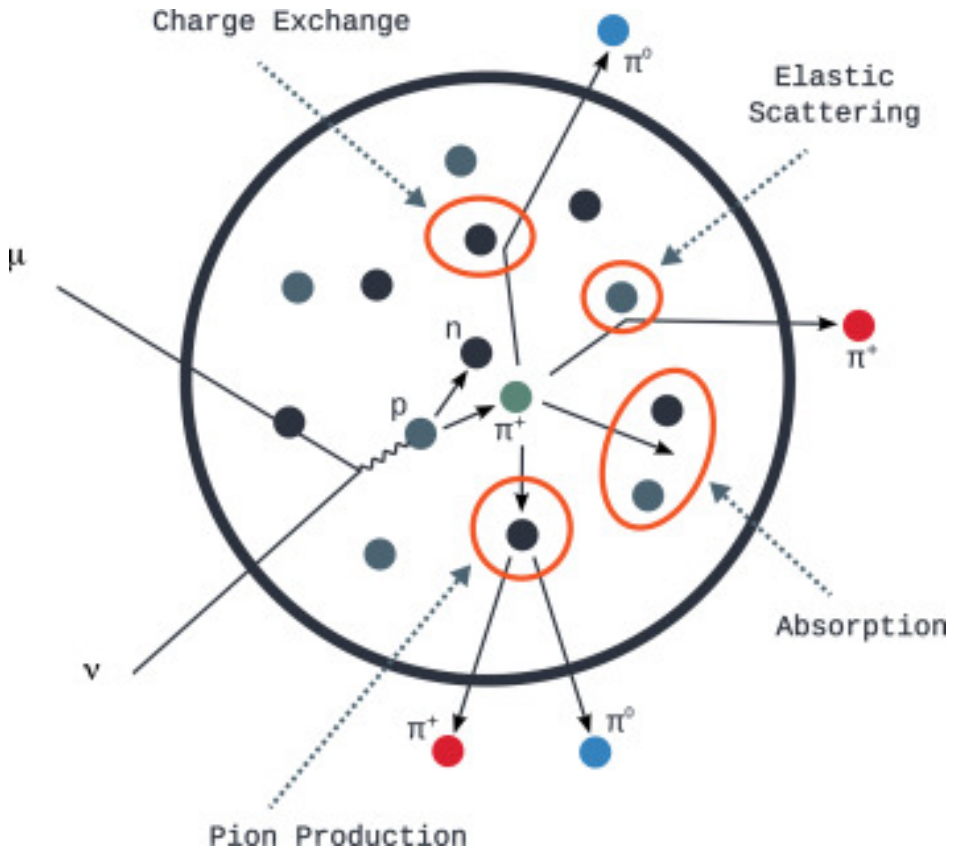

Figure 8: Diagram showing different Final State Interactions that could happen to an initially produced Pion. The charge and direction of the pion or the number of pions that escape the nucleus can be changed compared to the initial interaction depending on how the pion interacts. Image taken from [10].

The interaction modes previously discussed are categorized by their products, however FSI can alter the particles that leave the nucleus, thus changing the signatures left in the detector, and present a problem in the study of neutrino-nucleus scattering.

2.4 Cross-Sections

The measurement of probability that a given interaction will occur is called the Cross-Section [2]. It has units of area. The cross-section is determined by the shape, strength and range of the interaction potential (for neutrinos which only interact with nuclei via the weak interaction, it is much less than for charged leptons which also interact via the electromagnetic interaction) [2]. For a beam experiment, the cross-section can be measured from the reaction rate if the flux of the

incoming beam particles and the area density of the scattering centers are known, as seen in the following equation [2]:

$$\sigma_{tot} = \frac{\text{number of reactions per unit time}}{\text{beam particles per unit time} \quad \text{x} \quad \text{scattering centers per unit area}}. \tag{15}$$

The total cross-section can be broken up into a sum of the cross-section of the different elastic and inelastic processes that occur [2]. For this analysis, the differential cross-section is measured instead of the total. Events are measured in bins of analysis variables, represented by x_i:

$$\frac{d^3\sigma}{dT_\mu d\cos\theta_\mu dE_{avail}} = \frac{N_{interactions}(x_i)}{(\phi)(N_{target})(\Delta x_i)} \tag{16}$$

Δx_i represents the bin volume for the three analysis variables that the differential cross-section is measured in. ϕ represents the beam flux. (N_{target}) represents the number of targets. The choice in variables and bin sizes for this analysis, as well as how the number of interactions is extracted from the detector response will be explained in later chapters.

Accurate measurements of the cross-section are important to understanding neutrino oscillation. In order to extract neutrino oscillation parameters in a long-baseline neutrino experiment, measurements of the event rate distributions are measured at both the near and far detectors. Knowledge of the cross-section of the flavors being measured is necessary to extract the probability of the transition from the event rate distributions [11]. Measuring the CP phase also requires measuring separate cross-sections for neutrinos and antineutrinos, to see the effects oscillation has on their event rates [11].

The $\nu_\mu CC$ inclusive cross-section refers to the cross-section measured for all $\nu_\mu CC$ events. Exclusive is the term used when there is exactly one final state in the analysis. The inclusive cross-section is necessary for oscillation parameter extraction, while exclusive cross-sections are useful for building models and event generators for simulation [12]. This analysis is semi-inclusive, looking at the case where there is a $\nu_\mu CC$ event and one particle visible in the detector. It is called semi-inclusive because it doesn't explicitly require the one visible particle to be a muon. The

development of this choice is explained in future sections.

2.5 Low Hadronic Activity

This analysis is concerned with a particular regime of the $\nu_\mu CC$ interaction. The goal of this regime is to study QE and MEC interactions. QE and MEC interactions are enhanced when there is low hadronic energy in the interaction. The low hadronic activity sample is defined as a $\nu_\mu CC$ interaction where outgoing protons and pions don't have enough kinetic energy to leave tracks in the detector [5]. A thorough explanation of the Low Hadronic Activity regime will be given in Chapter 5.

3 NOνA Experiment

NOνA is short for the NuMI Off-Axis ν_e Appearance experiment. NOνA is an experiment that measures the oscillation of muon neutrinos produced at Fermilab in Illinois to electron neutrinos measured at Ash River, Minnesota.

3.1 NOνA Goals

NOνA was built to observe the oscillation of muon neutrinos to electron neutrinos. To this end, NOνA requires a beam of muon neutrinos and two detectors. One detector to measure the beam of neutrinos before oscillation has a chance to occur and one placed to measure the neutrinos after oscillation has occurred.

Observation of electron neutrino appearance allows NOνA is to study the neutrino mass state ordering. That is, whether or not mass state 3, which is approximately a 50-50 mix of muon and tau states, is lighter or heavier than the other two mass states (mass state 1 being mostly made of the electron neutrino state while mass state 2 is roughly equal between all three flavor states). NOνA also studies CP-violation (charge-parity) between neutrinos and antineutrinos. NOνA can create a beam of either muon neutrinos are muon antineutrinos to study whether there are differences between how the neutrinos and the antineutrinos oscillate.

This analysis seeks to measure the cross-section of the muon neutrino charge-current interaction in a particular regime. Precise measurements of the neutrino Cross-Section is important to the study of neutrino oscillation. The cross-section model informs predictions of how many neutrino events should be observed prior to or in absence of neutrino oscillation and the energy spectra of those events. And by comparing the observed spectrum before and after neutrino oscillation occurs to the predictions in absence of oscillations, the oscillation parameters can be extracted.

3.2 NuMI Beam

The Neutrinos at the Main Injector (NuMI) beam supplies the muon neutrinos for the NOνA experiment. The Fermilab accelerator complex supplies the protons that collide with a graphite

target, which produces the hadrons that decay into the neutrinos.

3.2.1 Proton Generation

Figure 9 shows the Fermilab accelerator complex which produces protons to feed into the NuMI beamline [13]. H^- ions are accelerated to 400 MeV by the Linac, and then converted to protons and accelerated to 8 GeV in the Booster [14]. The Main Injector stores and accelerates the protons to 120 GeV, and directs them to the NuMI target [14].

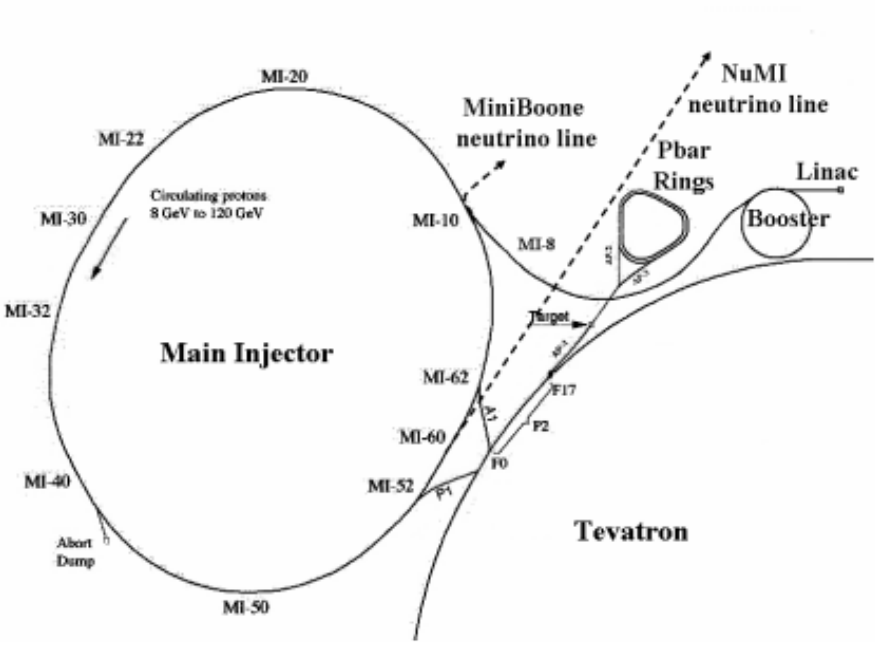

Figure 9: Schematic of the Fermilab accelerator complex. Includes the Main Injector that feeds protons into the NuMI beamline. Figure taken from NOνA Technical Design Report [13].

The NOνA experiment has collected 2.56×10^{21} protons-on-target (POT).

3.2.2 Neutrino Beam

The process by which protons from the Main Injector are used to produce the neutrino beam is shown in Figure 10.

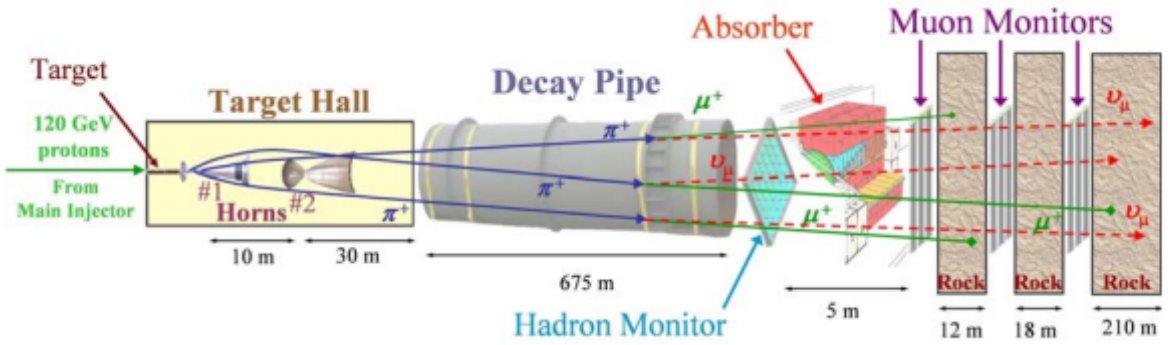

Figure 10: Schematic of the neutrino beamline production. Figure taken from NOνA Technical Design Report [13].

The protons from the Main Injector are directed toward a graphite target; the collision of protons and graphite produces hadrons (primarily pions, followed by kaons) [13]. The resulting hadrons are focused toward the beam axis by two magnetic horns [13]. The magnetic horns allow for charge selection of the hadrons [14]. For this analysis, the Forward Horn Current (FHC) is used to select for positively charged hadrons.

The hadrons of the selected charge enter a 675 meter long decay pipe, where the the hadrons decay. For this analysis where the FHC is used, positively charged hadrons decay to anti-muons and muon neutrinos via $\pi^+ \rightarrow \overline{\mu} + \nu_\mu$ and $K^+ \rightarrow \overline{\mu}^+ + \nu_\mu$.

The remaining hadrons and protons are absorbed by a hadron absorber [13]. The muons are stopped by the Earth, allowing the neutrinos to move on to the detectors [13].

3.2.3 Off-Axis

The Detectors for the NOνA experiment are placed off-center from the beam axis by 14.6 mrad [13].

At small angles, the flux and energy of neutrinos produced from the $\pi \rightarrow \mu + \nu$ decay and captured by a detector of area A at distance z are given by:

$$F = (\frac{2\gamma}{1+\gamma^2\theta^2})^2 \frac{A}{4\pi z^2} \tag{17}$$

$$E_\nu = \frac{0.43 E_\pi}{1 + \gamma^2 \theta^2} \tag{18}$$

where θ is the production angle, E_π is the parent pion energy and γ is the ratio of pion energy to mass [13]. For neutrinos resulting from Kaon decay, the 0.43 is replaced with 0.96, which results in a broader, more energetic distribution for identical meson energies [13].

As can be seen in Figure 11, the energy of neutrinos measured at a site 14 mrads off-axis does not have a strong dependence on the energy of the parent pion. This leaves a narrow energy band around 2 GeV, which is suited to studying the oscillation maximum at 1.6 GeV for $\Delta m^2_{32} = 2.5 \times 10^{-3} \text{eV}^2$ [13] [15].

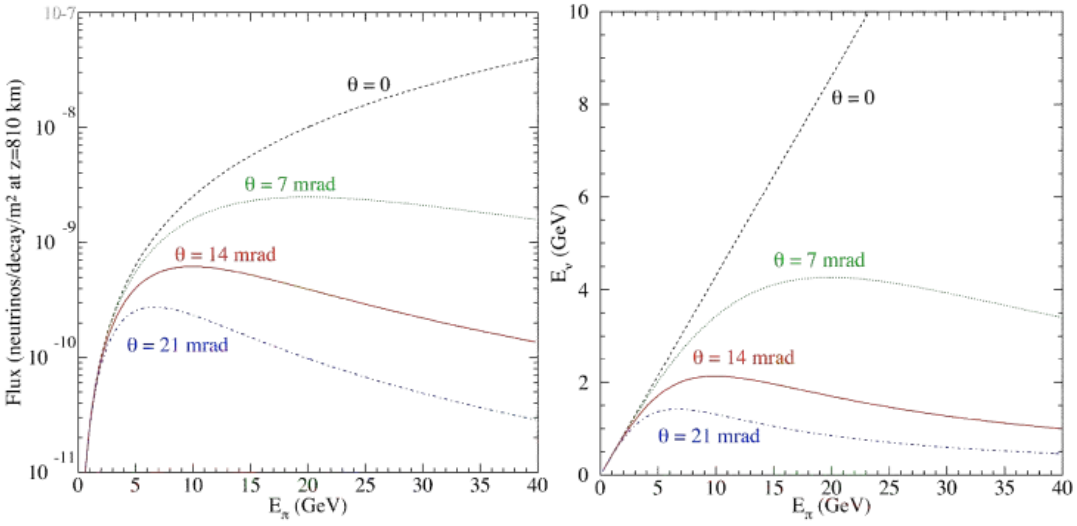

Figure 11: Left: The neutrino flux from a parent pion of energy E_π at sites located at θ degrees off-axis, normalized to a distance of 800 meters. Right: The energies of neutrinos produced at angles θ degrees off-axis as a function of pion energy. Figure taken from NOνA Technical Design Report [13].

Figure 12 shows the neutrino event rate as a function of off-axis angle and neutrino energy [13]. Using the off-axis angle site leads to an increase in the number of neutrino events at the desired energy band and a suppression of higher energy neutrino energies in comparison to the on-axis site [13].

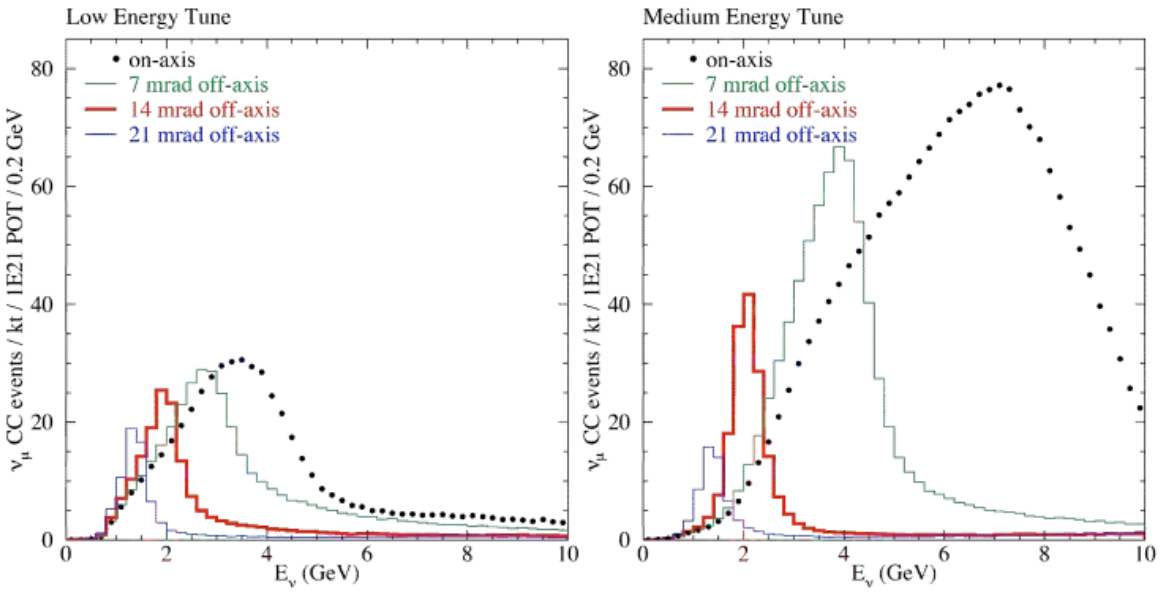

Figure 12: Neutrino event rates prior to oscillation, calculated for a distance of 810 km from Fermilab at various angles off-axis. Left shows the low energy configuration, right shows the medium energy configuration. Figure taken from NOνA Technical Design Report [13].

The suppression of high energy neutrinos leads to background suppression. Sources of these backgrounds compared to neutrino energy can be seen in Figure 13. Hadronic showers in neutral current events where the outgoing neutrino is not observed can fake the electron showers caused by lower energy ν_e charged current events [13]. Choosing a narrower energy band cuts out the higher energy neutrinos which can fake ν_e events in the desired region. This choice also cuts down on the number of ν_e events coming from an intrinsic component of the NuMI beam. The ν_e are mostly produced from three-body decay of the muon and are thus have a broader energy distribution than the ν_μ produced from two-body decay [13].

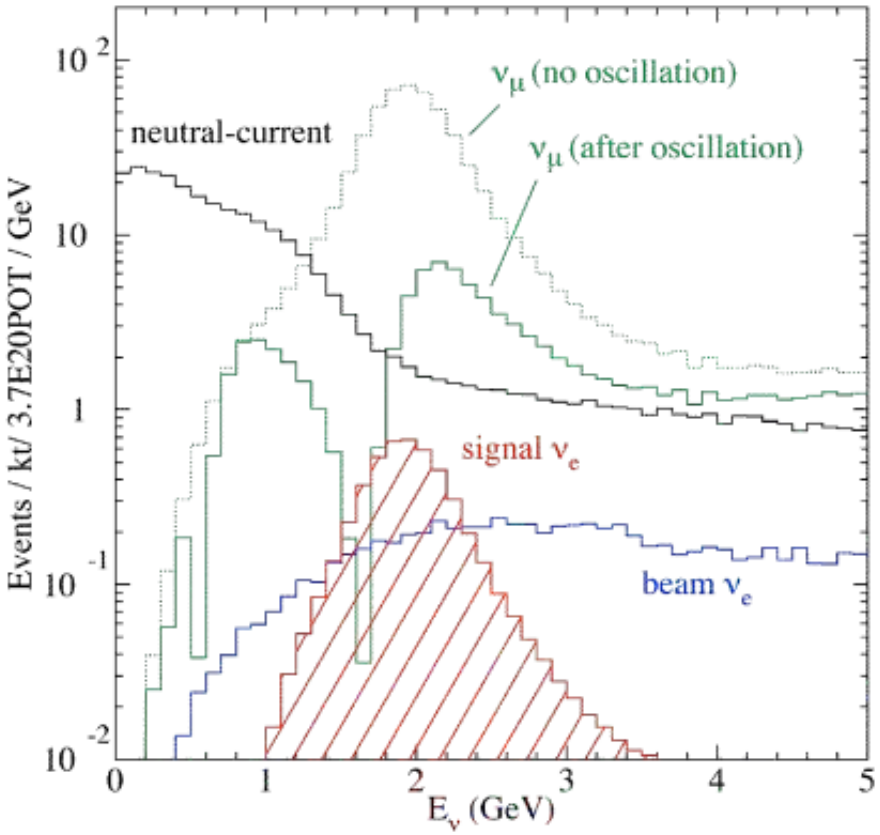

Figure 13: Simulated energy distributions for various neutrino events. These include, ν_μ charged current events (with or without neutrino oscillation), ν_e events that come from neutrino oscillation and those that come from the beam, and neutral current events. Simulation assumes off-axis distance of 12 km at 810 km distance from Fermilab, and values of $\Delta m^2_{23} = 2.5{*}10^{-3} eV^2$, $\sin^2\theta_{23} = 1.0$, and $\sin^2\theta_{13} = 0.10$. Figure taken from NOνA Technical Design Report [13].

3.3 Detectors

NOνA is a two detector experiment. The neutrino beam first passes through the Near Detector (ND) located at Fermilab. The beam then travels to the Far Detector (FD) located in Ash River Minnesota. The two detectors are made of identical components, however they are different sizes.

3.3.1 Detector Cells

The NOνA Detectors are made of many identical cells. A schematic of an individual cell can be in seen in Figure 14. Each cell is rectangular PVC filled with liquid scintillator and a wavelength-shifting fiber [13]. Charged particles travel through the cells primarily along its depth, and light is produced by the scintillating liquid [13]. Light travels until it is either captured by the wavelength-shifting (WLS) fiber or absorbed by the PVC or scintillator [13]. Both ends of the wavelength-shifting fiber are directed to one pixel of an Avalanche-Photodiode (APD) detector array and light is converted into an electric signal [13].

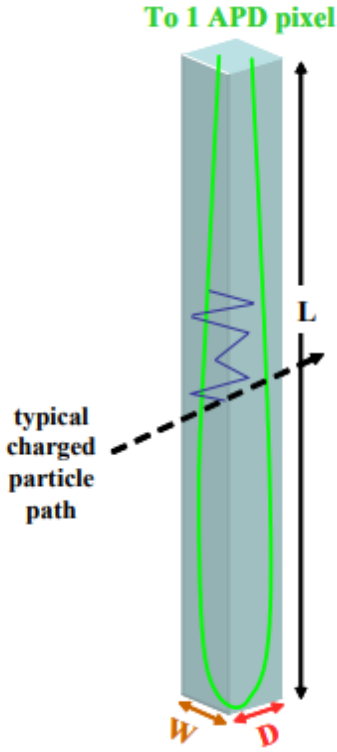

Figure 14: Schematic of an individual cell in one of the NOνA Detectors. Scintillation light produced by a particle interacting in the detector gets carried to the APD by the wavelength-shifting fiber. Figure taken from NOνA Technical Design Report [13].

Approximately 70 percent of the mass of the detectors is the liquid scintillator made of mineral oil with with 4.1 percent pseudocumene [1,2,4-Trimethybenzene] as the scintillant [13]. The

majority of the remaining 30 percent of the mass is due to the rigid PVC extrusion [13].

The wavelength-shifting fibers capture blue light (400 - 450 nm wavelength) from the scintillator and shifts it to green light (490 - 550 nm wavelength) [13]. The fibers are looped in the cells, effectively making each cell having two unlooped fibers with a perfect mirror at the bottom, leading to four times the amount of light being captured compared to a single non-reflecting fiber [13]. Internally reflected light travels to the APDs; the light is attenuated as it travels down the length of the fibers, with red light (520 - 550 nm wavelength) preferentially surviving [13].

Light is absorbed in the collection region of the APDs, electron-hole pairs are generated, and the electrons propagate to the p-n junction under the influence of an applied electric field [13]. At the junction, the electric field is sufficient for avalanche multiplication of the electrons to occur [13]. APDs are packaged in arrays of 32 pixels that correspond to 32 cells in the detector [13]. Both ends of the Wavelength Shifting Fiber lead into the same pixel [13]. The APDs are operated at a gain of 100 times at a voltage of 375 volts and have a quantum efficiency of 85 percent [13]. The signals from the APDs are then digitized by Analog-Digital Converters (ADCs) [13].

The cells are arranged into planes. The planes alternate between horizontal and vertical orientation. When a cell is triggered, a pixel in the APD is triggered, but information of how deep in the cell the particle was is lost. With alternating planes, the 3D path of the particle can be reconstructed.

3.3.2 Near Detector

This analysis concerns measurements in the NOνA Near Detector. This detector is used to measure the NuMI beam before oscillations have occurred. The Near Detector is placed approximately 1 kilometer from the NuMI target and approximately 800 meters from the typical pion decay vertex [13].

The Near Detector's dimensions are 2.8 meters wide, 4.1 meters tall, and 14.5 meters long [13]. The minimum size constraints are that it needs to be large enough for the fiducial volume to have well-defined boundaries, and it needs to be large enough to fully contain events (that is, that no

particle in the event leaves the detector) that occur in the fiducial volume [13]. Simulations have shown that a 70 cm border around the fiducial volume in the transverse dimensions and a 4 meter border around the fiducial volume in the longitudinal dimension provide sufficient containment of the ν_e events [13]. Figure 15 shows how the size of the Near Detector compares to the Far Detector and shows the alternating orientation of the cell planes.

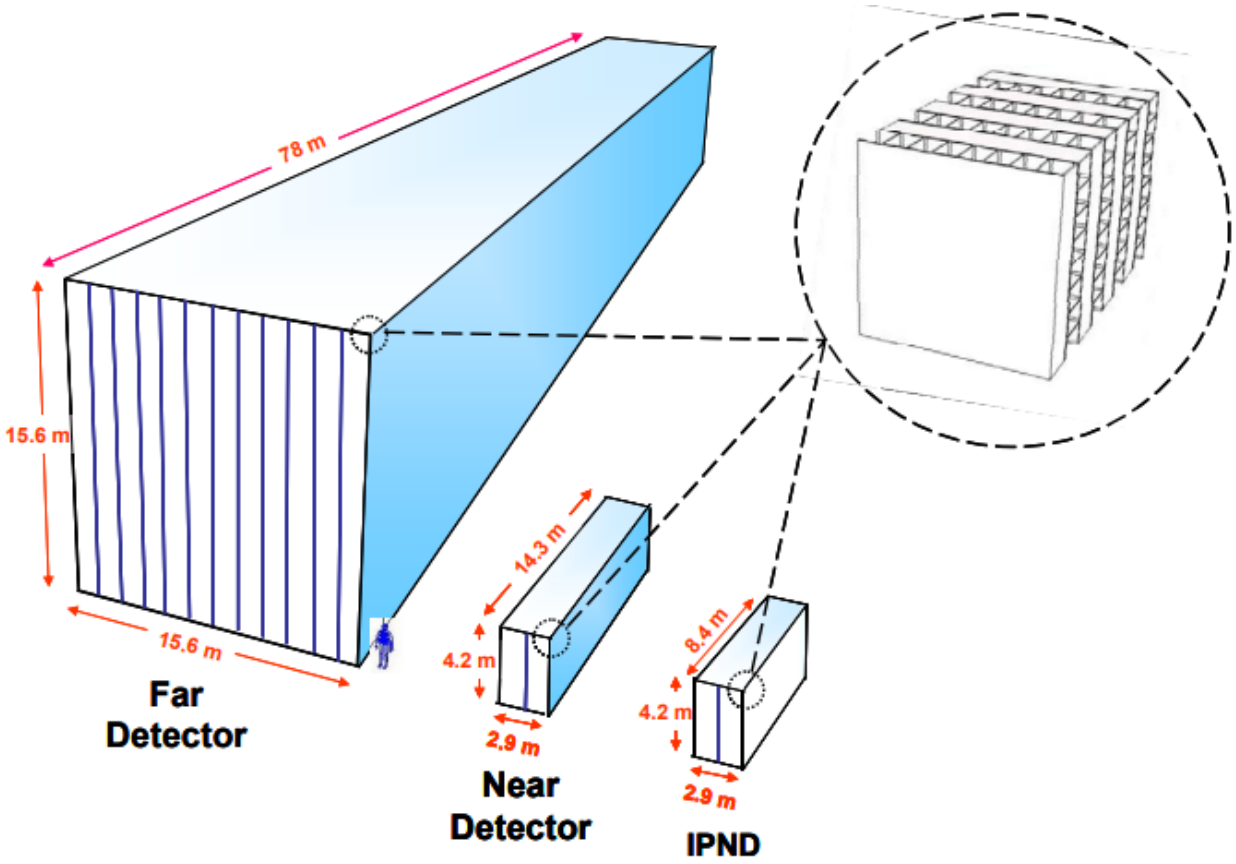

Figure 15: Diagram of the NOνA Detectors, side by side, showing their relative sizes. On the left is the NOνA Far Detector, middle is the NOνA Near Detector, and right is the prototype Near Detector. The different detectors are made of planes of alternating vertical and horizontal cells as shown in the inlet. Figure taken from NOνA Technical Design Report [13].

A diagram of the Near Detector can be seen in Figure 16. The planes are 64 cells wide or 96 cells high depending on orientation [13]. First there are six planes that make up the veto region, followed by the 108 of the fiducial volume, then 72 planes that make up the shower containment region, and then the muon catcher [13].

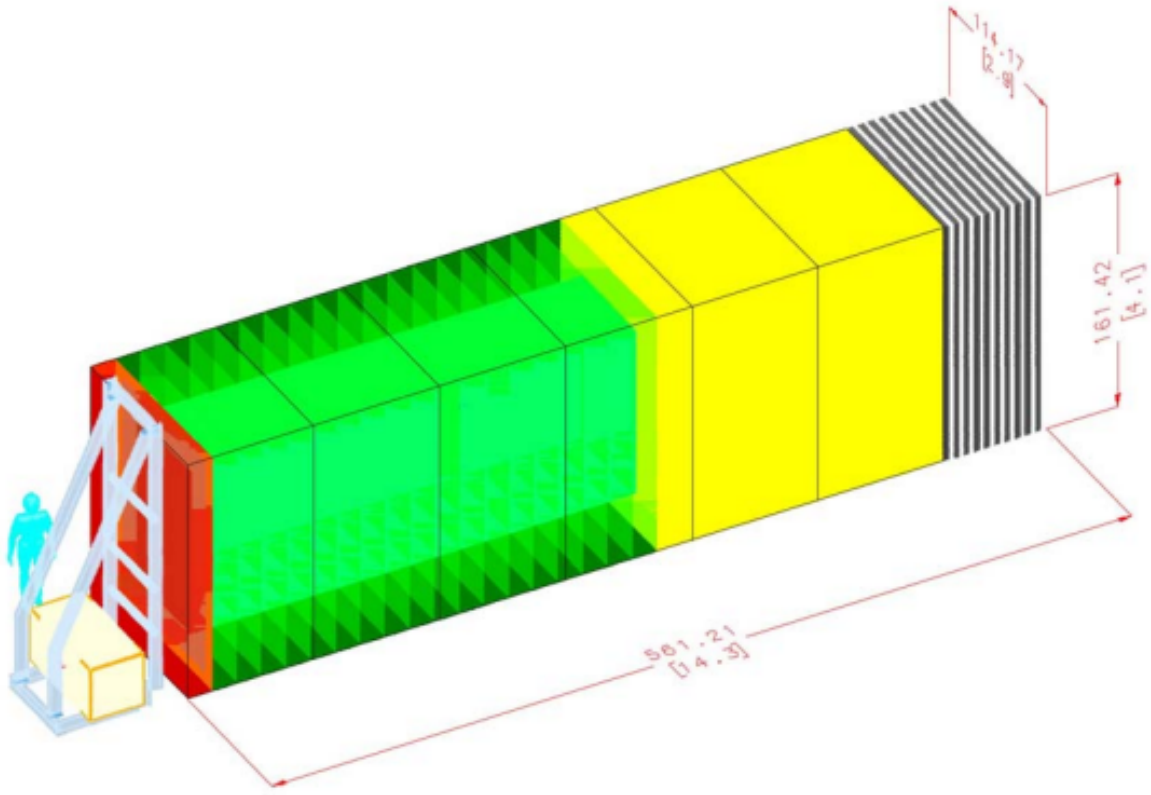

Figure 16: Diagram of the NOνA Near Detector, color coordinated by sections. The Near Detector is made of 6 blocks of 31 planes, followed by a muon catcher. The NuMI beam comes from the lower left in this diagram. The red section represents the veto region, made of 6 planes. The green section represents the fiducial volume, made of 108 planes. The yellow section represents the shower containment region, made of 72 planes. All of these regions are made with fully active liquid scintillator cells. The black and white region is the muon catcher region of steel interspersed with 10 active planes of liquid scintillator. Figure taken from NOνA Technical Design Report [13].

4 NOνA Simulation and Reconstruction

This analysis makes use of simulation to test its procedures before making a measurement of the cross-section of the muon neutrino charged current interaction using NOνA's data. The process of a muon neutrino beam being produced, hitting the detector, colliding with particles in the detector, and the detector's response is simulated by various packages.

For both the simulated and the real detectors, once the detector response has been collected, there is a process, called reconstruction, to make determinations about the underlying neutrino events based on the the detector response.

4.1 Simulation

The simulation process follows the same general process outlined in Chapter 3. The first step to be simulated is the muon neutrino beam. The beam simulation is handled by the FLUKA [16] and FLUGG GEANT4 [17] software packages. FLUKA handles the production and transport of the neutrino beam. This starts with modeling hadron production, focusing in the horns and the decay of pions, kaons, and muons in the decay pipe to determine the production rate and energy spectrum of each flavor of the neutrinos in the beam, while FLUGG models the geometry of the detector [18]. The resulting information is stored in flux files which are then used as input for the neutrino interaction simulation.

After the neutrino beam is simulated, the neutrinos interacting with particles in the detector is simulated. The simulation of neutrino interactions is carried out by the GENIE (Generates Events for Neutrino Interaction Experiments) software package. The GENIE package contains many models to cover the large variety of process involved in neutrino-nucleus interactions [19]. GENIE packages compatible models into groups called "comprehensive model configurations" or CMCs to cover the range of possible of neutrino interaction modes [20]. NOνA made choices about which models to use for QE, MEC, DIS, and RES as well as for which FSI model to use. For the simulation used in this analysis, NOνA uses the Valencia model for QE with Z-expansion

formalism to provide systematic uncertainty coverage [20]; for RES NOνA uses the Berger-Sehgal model [20]; for MEC, NOνA uses the Valencia model [20]. For DIS, NOνA uses the Bodek-Yang (BY) formulation [21]. For FSI models, NOνA uses the "hN" semi-classical cascade model [20].

After the neutrino interaction events are simulated, the detector response to the events is simulated. The detector simulation is carried out by the GEANT4 package. GEANT4 uses the particles lists that are created by GENIE to propagate particles through the detector (e.g. simulating the energy loss of charged particles and simulating scattering of charged and neutral particles produced) and leave energy deposits in the active material [18].

While GEANT4 is capable of simulating the optical processes that take energy deposits in the detector to a readout (i.e. the propagation of light along the WLS fibers), this process is computationally expensive. Instead, driven by the fact that the detector is made of many identical cells, templates are generated to parametrize photon transport [18].

4.1.1 Light Simulation

The number of photons produced by an energy deposition is modeled by the following equation:

$$N_\gamma = F_{view}(Y_s E_{Birks} + \epsilon_c C_\gamma) \tag{19}$$

E_{Birks} is the energy given by Birks' law for a particle traveling through a scintillator, while C_γ is the energy deposited by Cherenkov photons. F_{view} is an overall scaling factor for each view, Y_s is a scaling factor for the scintillation energy, and ϵ_c is a scaling factor for the Cherenkov Energy [22]. There are uncertainties introduced by this choice of light model covered in Chapter 10.

There is also a downward trend in the light level as a function in time, due to an effect called "Detector Aging". A discussion of a corresponding increase in the overall calibration scale and the uncertainties introduced are covered in Chapter 10.

4.2 Reconstruction

Reconstruction is the process of taking the detector response and making determinations about the underlying neutrino events. The procedure is applied to both real and simulated detector output.

A "hit" refers to the information from a single triggered channel, while a "data event" refers to a grouping of hits in an arbitrary time window, currently 550 microseconds [23]. A single interaction event is separated from the larger readout window into a single object called a "slice" [23]. For the NOνA Near Detector, around 4 neutrino interactions are expected in every 10 microsecond beam window [23]. To separate the individual neutrino interactions using spatial and temporal information, a density-based clustering algorithm (DBSCAN) is used [23]. Hits are included in a cluster if they are surrounded to by enough neighbors to be considered a "Core" point or a neighbor to a Core point.

Once a slice has been made, a Multi-Hough transform is used to identify feature guidelines in the slice [23]. A Hough transform is a standard algorithm used to identify features in a 2D image made of points [23]. The Hough transform is applied to pairs of points in each detector view separately [23]. Hits that are associated with the line produced by the Hough transform are removed, and the process is repeated again, until no more lines can be produced [23].

The Elastic Arms method is used to identify the vertex of the interaction [23], the location where the neutrino interaction occurred. It takes the output of the Multi-Hough transform algorithm to use a seed to find the vertex [23]. The vertex is chosen from a list of vertex candidates, based on which candidate minimizes the energy cost function given by the following equation.

$$E = \sum_{i=1}^{N}\sum_{a=1}^{M} V_{ia}M_{ia} + \lambda\sum_{i=1}^{N}(\sum_{a=1}^{M} V_{ia} - 1) + \frac{2}{\lambda_v}(\sum_{a=1}^{M} D_a) \tag{20}$$

E is the energy cost, M_{ia} is the distance between cell hit i and cell arm a, V_{ia} is the strength of association between hit i and arm a, D_a is the measure of distance between the vertex and the first hit in arm a, and λ and λ_v control the strength of the terms. [23]. The first term measures the goodness of fit between the hits and the arms, the second term is a penalty for hits not associated

with any arm, and the the third term is a penalty for arms whose first hit is far from the vertex [23]. V_{ia}, the hit/arm association strength, is given by the following equation.

$$V_{ia} = \frac{e^{-\beta M_{ia}}}{e^{-\beta\lambda} + \sum_{b=1}^{M} e^{-\beta M_{ib}}} \tag{21}$$

β is interpreted as a range over which hits are allowed to be associated with arm a, and $e^{-\beta\lambda}$ represents the likelihood that the hit is noise [23]. For $\nu_\mu CC$ events, 68 percent of the identified vertices are within ten centimeters of the true vertex (within approximately two cell widths) [23].

Once a vertex has been identified, the next step is to identify each prong in the interaction. Each prong represents either a single particle track or shower [23]. A probabilistic fuzzy-k means algorithm is applied to assign the hits to prongs. A k means algorithm places a number of observable events into a number (k) of clusters, in a way that minimizes the variance. "Probabilistic" means that the total probability for each hit to be a member of all prongs does not need to add up to one, leaving the possibility that a hit can be considered noise [23]. Fuzzy means that the number of prongs is not known at the start and a hit is allowed to belong to more than one prong [23]. The fuzzy-k algorithm determines the number of prongs and assigns prong membership to all hits in each view [23]. 'Each view' refers to either the horizontal or vertical planes in the detector. The last step is to match the two detector views to make a 3D object, this is accomplished by comparing every pair of clusters from each view and comparing the cell hit energy distributions as a function of distance along the track [23].

After the event has been reconstructed, the event needs to be identified based on observable characteristics. The goal for this analysis is to identify $\nu_\mu CC$ low hadronic activity events. The process for how these events are identified is described in chapter 5, in the section on selected events.

4.3 Weighting

GENIE contains many models of neutrino interactions. The choice of MEC models was complicated for NOνA, because no current model appropriately matched experimental data [20]. The choice of the Valencia MEC model was motivated to make comparisons to T2K and MINERvA easier since they use the same model [20]. MEC events are generated in GENIE using the Valencia model. Then corrections are made to the MEC model using weights to make the simulation better match NOνA's data. The weights are determined using a double-gaussian fit to the ND Data with thirteen parameters.

Table 3: Results of the double Gaussian fit used for the MEC weights in this analysis [24].

Component	Parameter	Value
Gaussian 1	Normalization	15.0283
	Mean q_o	0.346049
	Mean $\|\vec{q}\|$	0.879167
	Sigma q_o	0.10241
	Sigma $\|\vec{q}\|$	0.385406
	Correlation	0.904447
Gaussian 2	Normalization	140.0
	Mean q_o	0.0341836
	Mean $\|\vec{q}\|$	0.450603
	Sigma q_o	0.0362089
	Sigma $\|\vec{q}\|$	0.257338
	Correlation	0.80864
Base Model	Normalization	-1.02274

A weight is determined based on the fit parameters as follows:

$$weight_{mec} = baseline + gauss_1(|\vec{q}|, q_o) + gauss_1(|\vec{q}|, q_o) \tag{22}$$

The parameter values in this analysis are listed in the table above.

Figure 17 shows the energy and momentum transfer distributions of events in the Near Detector before and after the weighting, as well as the distribution of weights that come from the fits [20]. This analysis is sensitive to the region shown in Figure 17 where the weights are highest, and where there are low statistics in the pre-fit region. This causes issues that will be discussed in Chapter 8.

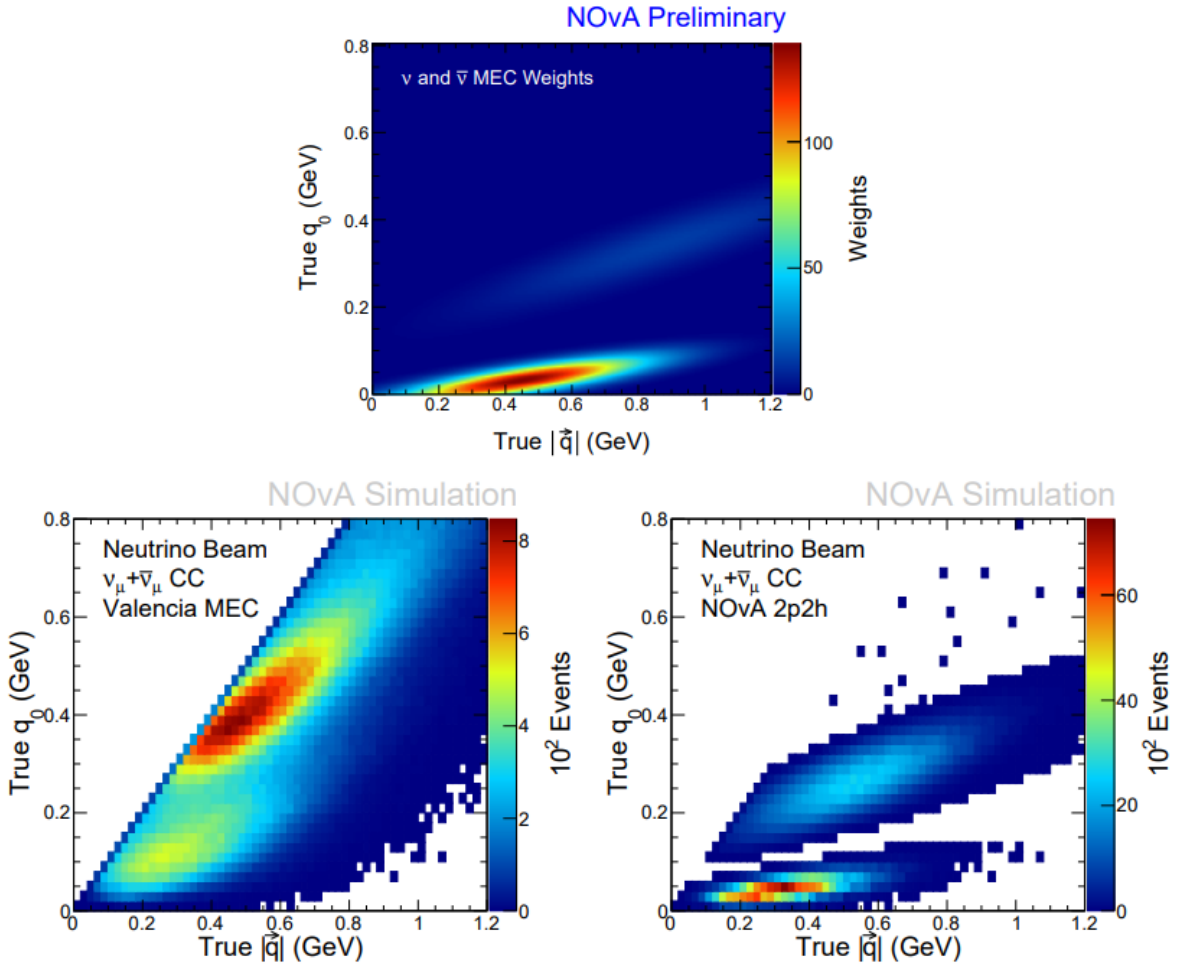

Figure 17: MC in the 2D $(|q|, q_0)$ phase space. Top: Central Value weights. Bottom left: simulated MEC events with the Valencia model. Bottom right: simulated events with weights applied, resulting in NOνA 2p2h. Figure taken from NOνA XSec Tuning Paper [20].

With regards to FSI, NOνA found that the level of agreement between external pion data and GENIE predictions from the hN model required significant adjustment of the tuning parameters

[20]. The pion mean free path (average path traveled by pions before re-interacting) was significantly reduced and there were adjustments in the relative fractions of the various processes available for pion re-interactions (e.g. absorption, QE scattering, charge exchange) [20].

When a new CMC is chosen, new lookup tables (called "splines") containing the parameters used for each process on each target nucleus are produced [24]. However, the new NOνA splines were instead used to configure the previous CMC [24]. The effect was, NOνA was working with the cross-section models that had the kinematics and topologies of the previous tune, while having the cross-sectional energy dependence of the current tune [24]. Instead of going through the time consuming process of regenerating the Monte-Carlo simulation, a new weight was created to fix the issue caused by the so-called GENIE Skew [24]. The parameters from both the FSI weights and the MEC weights were adjusted.

4.4 Detector Calibration

The detectors have to be calibrated so that the amount of energy deposited in a cell can be inferred from the number of photoelectrons captured by the APDs. Hits from cosmic ray muons are used for the calibration process. Cosmic ray muons are used because they are a consistent energy source across the detector [25].

The output from the APDs must first be corrected for differences in output that occur due to where in the detector the hit occurs. As light travels up the wavelength-shifting fiber, it is subject to attenuation. The further it must travel through the cell, the more energy is lost. Therefore for two identical energy deposits occurring at different positions in the cell, there would be two different readings from the ADC [26]. There is also a minimum threshold energy that must be exceeded for it to be recorded. For muons further away from the electronics, more energy is lost during attenuation, and therefore only higher energy depositions are recorded. This means that there is a higher true energy depositions for the reconstructed energy depositions that originate from places further from the electronics in comparison to closer deposits. Lastly there are "shadowing" or "shielding" effects where muons that reach the bottom of the detector have higher energy than those stop near the

top of the detector. Hits near the top of the detector that are associated with muons that reach the bottom of the detector have a higher average dE/dx compared to hits associated with muons that stop near the top of the detector [26]. The process of correcting for these effects is called relative calibration. After the relative calibration, the photoelectrons (PE) in each hit can be converted to a "corrected" photoelectrons value (PE_{corr}) that accounts for the position dependent effects.

The effect of relative calibration can be seen in Figure 18. After the relative calibration there is a long stretch where the PE_{corr}/cm is constant. Near the edges of the cell, however, there are regions where the PE_{corr}/cm is not constant. An additional uncertainty called the "Calibration Shape Uncertainty" is introduced to cover this deficiency [26].

The process of going from the corrected photoelectrons to an amount of energy deposited in a cell measured in GeV is called absolute calibration.

The Bethe-Bloch equation gives the energy loss per path length of particles in the detector [27]. The muons are assumed to be high enough energy to be minimum ionizing particles (MIPs) where the energy per path length can be assumed to be constant [27]. For the stopping cosmic ray muons in liquid scintillator, the $dE/dx \approx 1.9\mathrm{MeV/g} * \mathrm{cm}^2$ [27].

To select for stopping cosmic ray muons, tricell hits (hits in cells that are between adjacent cells that have hits) are chosen in the region of 100 - 200 cm away from the end of a track, and the hits path length through a cell is between 0.1 and 10 cm [25]. The particle energy loss is constant to about 1.8 percent in the 100 - 200 cm region [25].

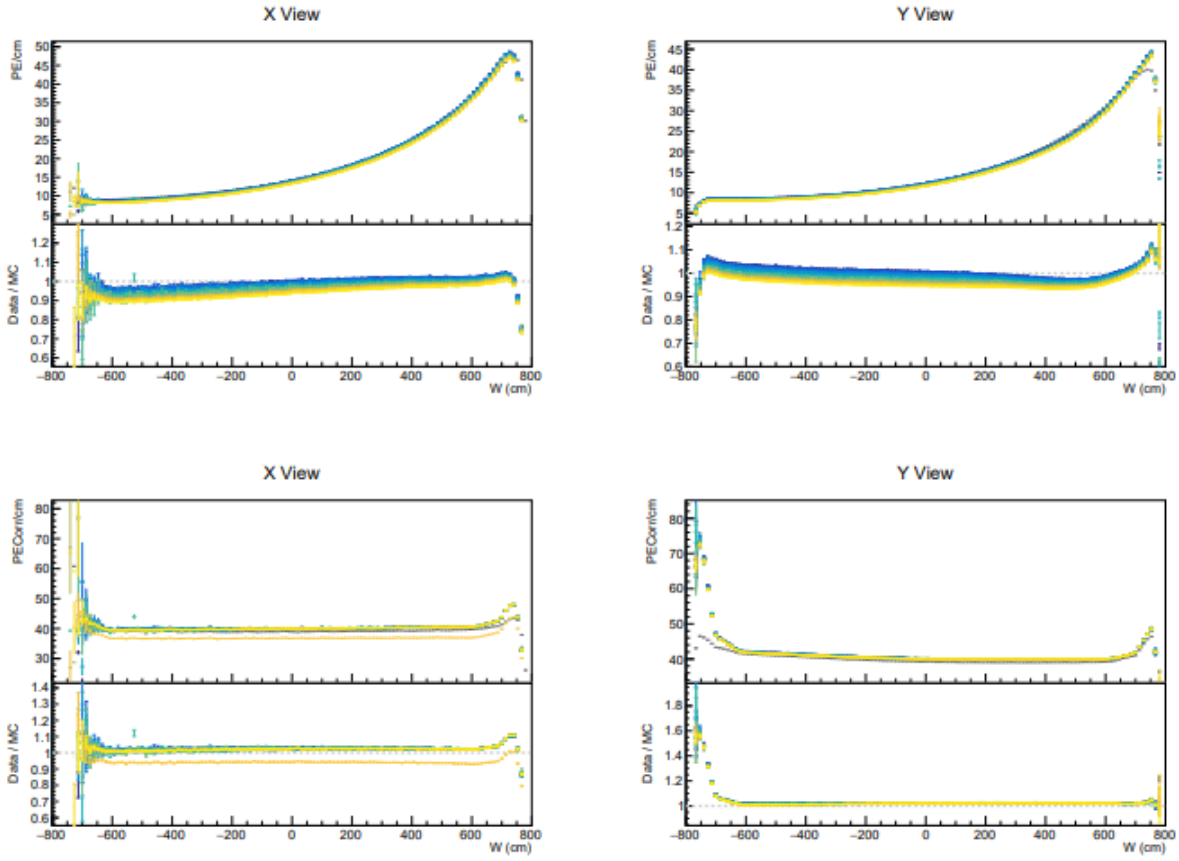

Figure 18: View of PE/cm vs position in the cell. Top pair: before relative calibration. Bottom pair: after relative calibration. Left pair: XZ view of a detector cell. Right pair: YZ view of a detector cell

The results of the absolute calibration are expressed as muon energy units (MEU) [25]. From Figure 18, the mean of the flat region after the relative calibration is finished is measured. This mean is measured for each detector and for each measurement period, for both data and the simulated detectors, and is called MEU_{reco} and is measured in PE_{corr}/cm. The mean of the actual energies of the simulated muons is called MEU_{true} and is measured in MeV/cm. The calibration energy scale is the ratio between them:

$$\text{Calibration energy scale} = \frac{MEU_{truth}}{MEU_{reco}} \tag{23}$$

and is measured in $\text{MeV/PE}_{\text{corr}}$

5 Selection of Charged Current Muon Neutrino Interactions

In order to work with muon neutrino charged current ($\nu_\mu CC$) interactions with low hadronic activity events, selection criteria must be defined. There are selection cuts that are performed based on information from the detector, and signal cuts that are performed based on properties of simulated events. A set of cuts to identify $\nu_\mu CC$ events were developed to minimize the total systematic uncertainty from GENIE and detector systematics, and additional cuts were developed to isolate low hadronic activity events [28]

5.1 Signal Cuts

Events are chosen from simulated events, where the true nature of the interaction is known, as true $\nu_\mu CC$ low hadronic activity events or as background. A set of cuts define an event as a true $\nu_\mu CC$ low hadronic activity event (signal), but they cannot be applied to real data the way selection cuts can, since the true nature of the interaction cannot be known in the real data. The cuts can be split up between those that define a $\nu_\mu CC$ signal event, and the extra condition that make it a low hadronic activity event.

The straightforward conditions to ensure the interaction is a true $\nu_\mu CC$ interaction are that it must be a charged current event, and that there must be a muon produced. To ensure the interaction contains only low hadronic activity, a cap is placed on the kinetic energy of final state protons and pions. The protons can have no more than 250 MeV of kinetic energy and the pions can have no more than 175 MeV. Pions and protons with energy less than these thresholds won't leave tracks in the detector, making these events indistinguishable from events with no pions or protons in the detector.

5.2 Selection Cuts

Selection is the process of choosing events based on properties that can be observed in the detector, whether that be the simulated detector or the actual detector. The selection is designed to find events that are likely to be $\nu_\mu CC$ low hadronic activity events, but are limited by what is actually

observable in the data. The cuts can be split up into two sets: the cuts to find $\nu_\mu CC$ events, and the cuts to find low hadronic activity.

There are four cuts that make up the $\nu_\mu CC$ Inclusive Selection Cuts:

- Reconstruction Quality Cut
- Fiducial Volume Cut
- Muon ID Cut
- Containment Cut

The Reconstruction Quality Cut ensures reconstruction, the process of taking detector information and making determinations about the individual events that caused them. It applies a condition that there must be at least one track with more than twenty hits that goes through more than four continuous planes. Events that have fewer than twenty hits are generally background while the condition on the planes is to exclude vertical muons that are not from neutrinos [29]. Previous analyses have shown that very few $\nu_\mu CC$ events were excluded by the twenty hits condition, and that most muons associated with $\nu_\mu CC$ events leave tracks long enough to satisfy the planes condition [30].

The Fiducial Volume Cut requires that their be at least one Kalman track that lies in the fiducial volume [31]. A group of hits formed by one charged particle passing through the detector is called a track. A Kalman algorithm [32] is used to group hits together in a Kalman track. An object must have enough kinetic energy coming out of the interaction to leave a track in the detector. The fiducial volume was optimized by studying the fractional uncertainty on the cross-section of the $\nu_\mu CC$ inclusive interaction as a function of vertex [33]. It was found the appropriate bounds for the vertex of the track were between the following bounds:

- $-130 < X(cm) < 140$
- $-130 < Y(cm) < 140$

- $100 < Z(cm) < 1000$

The Muon ID Cut requires the particle coming out of the interaction to have some minimum probability of being a muon. The particle coming out of an interaction is given a muon ID score, which corresponds to their probability of being a muon. The algorithm used to assign this score is based on the energy deposition of the particle in the detector and scattering observables [31]. The minimum score that is chosen for this analysis is 0.24.

The Containment Cut requires that none of the particles leave the detector, and that only muons go into the muon catcher. It requires that showering particles are not within twenty centimeters of the edge. And it allows the muon to go into the muon catcher, but not through it. This is to ensure all of the neutrino energy is contained within the detector [31]. The forward projection of the Muon Track cannot be within five cells of the edge of the detector, while the backwards projection of the Muon Track cannot be within ten cells of the edge of the detector. The forward projection condition is to remove events with uncontained Muons, while the backward projection condition is to prevent contamination from neutrino interactions that occur outside the detector [33]. The last condition is to remove all events that could have exited the active region of the detector and re-enter into the Muon Catcher ("air gap events") [33], because they cannot be reconstructed.

The additional condition is the Low Hadronic Activity Selection Cut, which is the requirement that there must be exactly one Kalman track. This analysis looks for $\nu_\mu CC$ events where there is only one particle in the detector that has enough kinetic energy to leave a Track. Taken with the $\nu_\mu CC$ cuts, the Track is the muon candidate.

5.3 Purity and Efficiency

The two main measures of how well the selected events and the signal events match are called purity and efficiency. If a signal event passes selection, then it is called a selected signal event. The ratio of signal events that pass selection is called efficiency.

$$\epsilon = \frac{N_{SS}}{N_{Signal}} \tag{24}$$

where N_{SS} is the number of signal events that are selected and N_{Signal} is the total number of signal events. Purity is the measure of how many of the selected events are actually signal events. It is the ratio of selected signal events over selected events.

$$P = \frac{N_{SS}}{N_{Selected}} \tag{25}$$

where $N_{Selected}$ is the total number of selected events.

The stricter the selection cuts are, the more events will be excluded which will lead to a lower efficiency but a higher purity. Conversely less strict selection cuts will lead to fewer events being excluded, which will lead to a higher efficiency but a lower purity. More events will be selected, but it becomes less certain that a given event is a signal event.

To show this effect, what follows is a series of plots of the purity and efficiency. There will be two plots of the purity and efficiency for each of the selection cuts. One set of plots will use one of the selection cuts established in the previous section as a substitute for the whole selection, and calculate the purity and efficiency using that. The other set of plots will use the whole selection minus one of the cuts. Together, these plots will show the impact of each of the selection cuts.

The first plots to show is the case where there are no Selection cuts. The general expectation for the efficiency is that the number of Selected Signal events and the number of Signal events should be equal, therefore the efficiency should be equal to one. However, a fraction of the neutrino events are lost during reconstruction. The slicer algorithm that finds potential neutrino interactions is not perfectly efficient, therefore some of the neutrinos that did interact in the detector were not found by the algorithm. Therefore the efficiency in this case represents the efficiency of finding a neutrino event occurred. This case will still mark a maximum for the efficiency and a minimum for the purity. In Figure 19, the efficiency is plotted in the analysis bins. Figure 20, shows the purity plotted in the analysis bins The choice of bins and variables (muon kinetic energy, muon angle, and available hadronic energy) will be explained in a later chapter. The overall efficiency is 0.97 and the purity is 0.059.

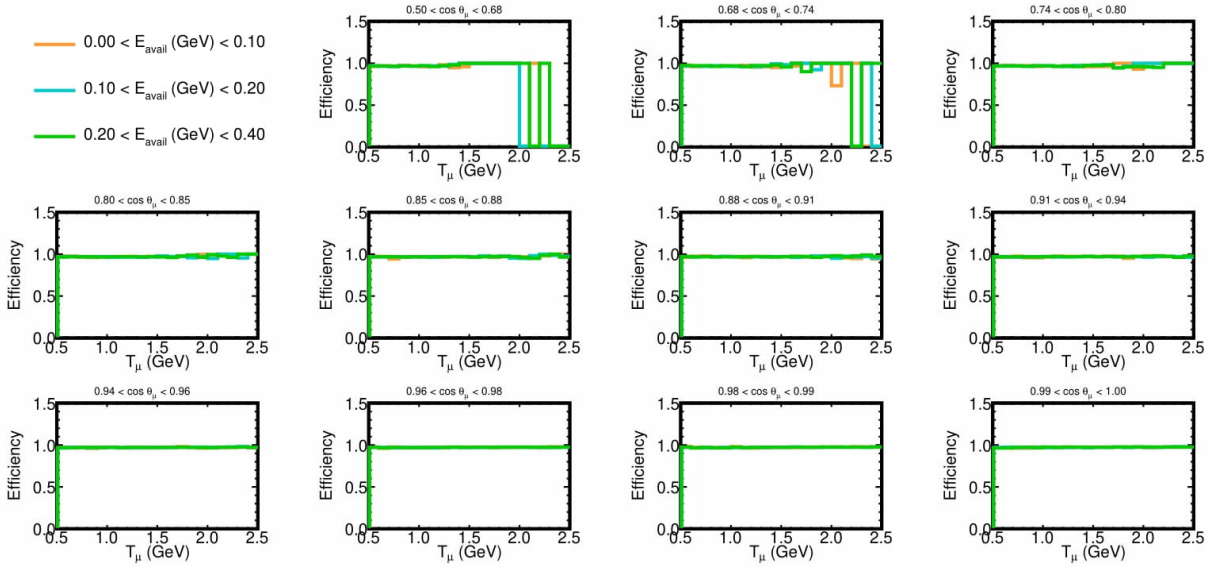

Figure 19: The efficiency when no events are cut due to Selection

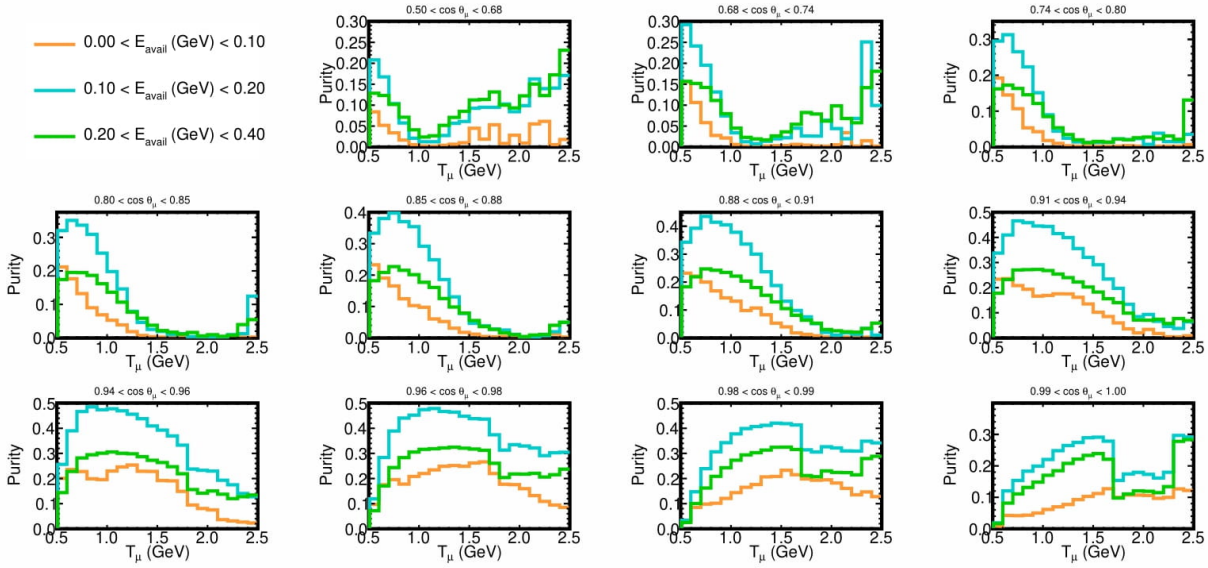

Figure 20: The purity when no events are cut due to Selection

The next case to show will be the full Selection. Here, all of the Selection Cuts are applied and then the purity and efficiency are calculated. This case will have the minimum for efficiency and the maximum for purity. Figures 21 and 22 show the efficiency and purity for this case. The overall efficiency is 0.21 and the purity is 0.80.

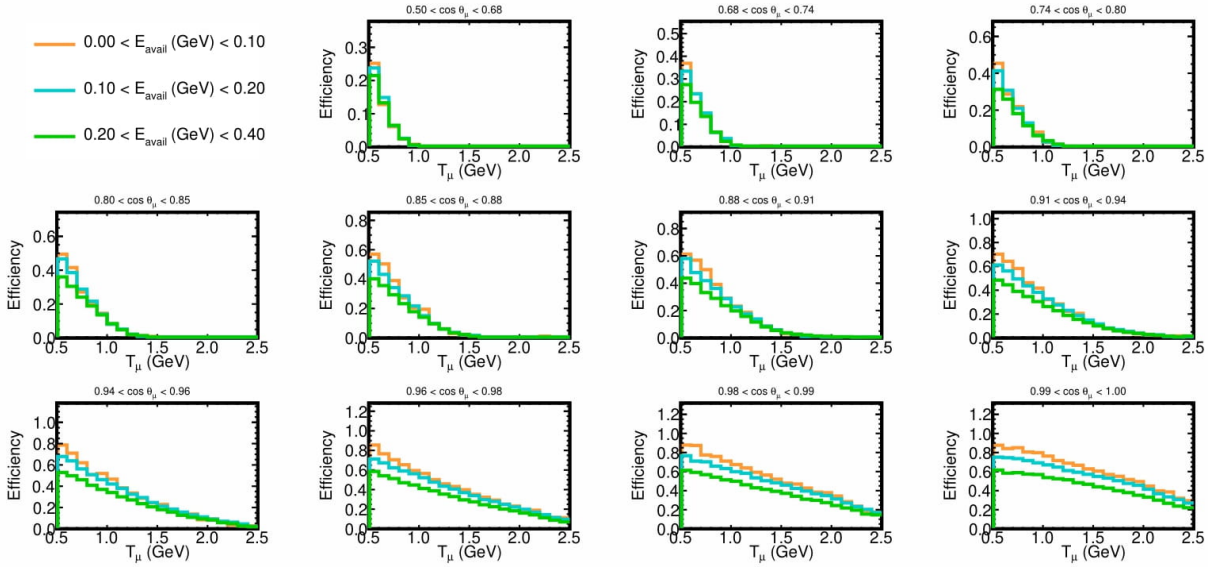

Figure 21: The efficiency when the full Selection is applied

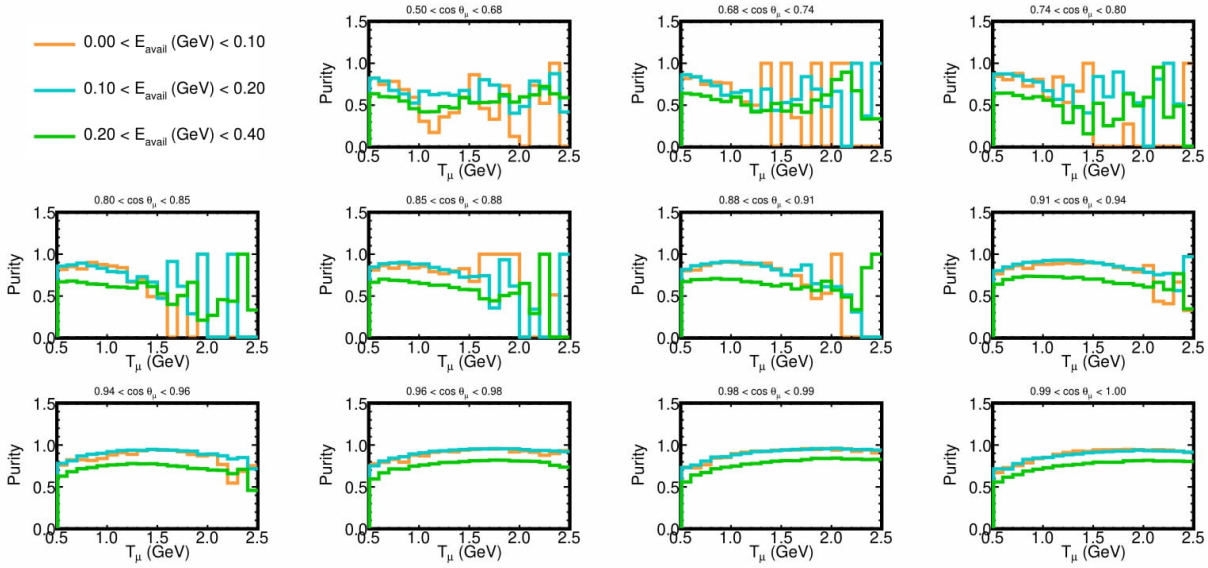

Figure 22: The purity when the full Selection is applied

The first cut applied in the selection during this calculation is the Quality Cut. When only the Quality Cut is applied, the efficiency is 0.94 and the purity is 0.068. When only the Quality Cut is absent, the efficiency is 0.21 and the purity is 0.79. Of all the cuts, the Quality Cut has the smallest impact. Figures 23 and 24 show the efficiency and purity when only the Quality Cut is

applied. Figures 25 and 26 show the efficiency and purity when only the Quality Cut is absent.

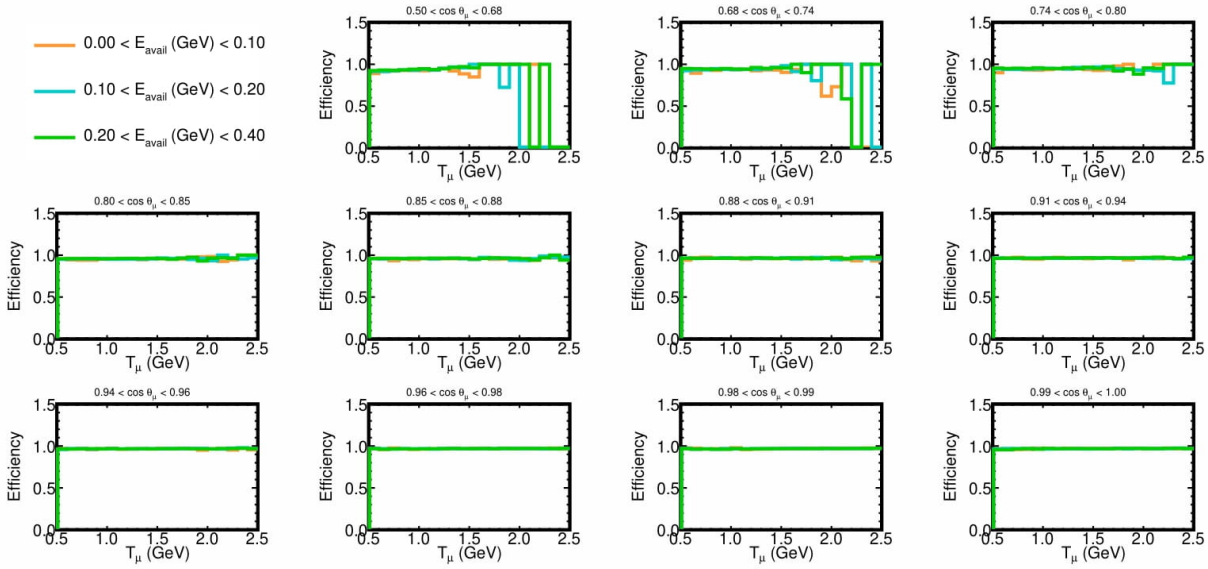

Figure 23: The efficiency when only the Quality Cut is applied

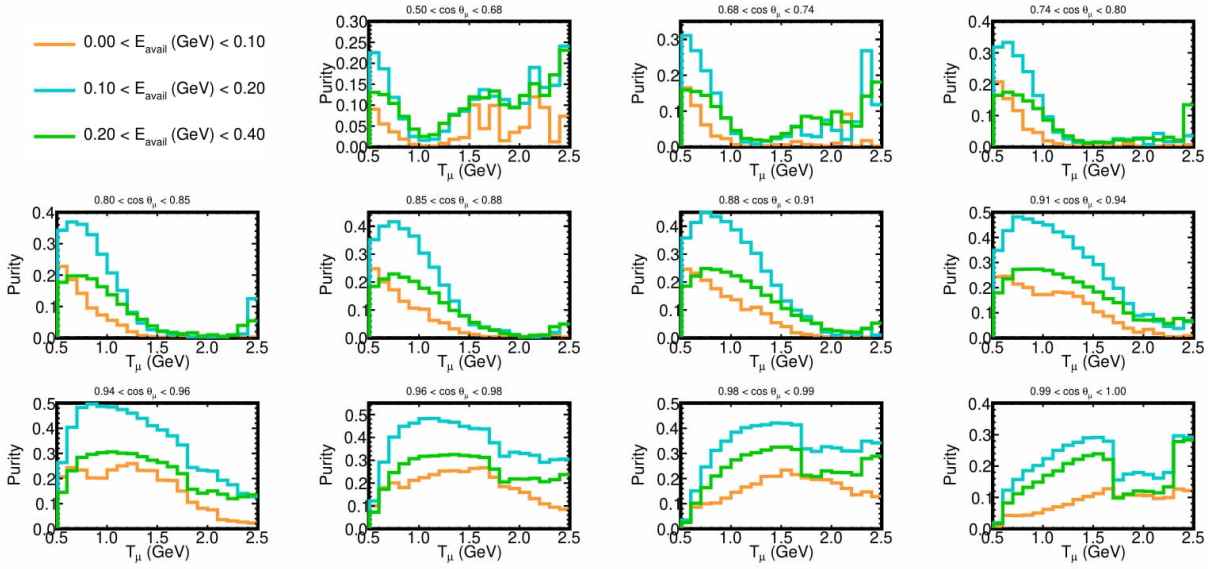

Figure 24: The purity when only the Quality Cut is applied

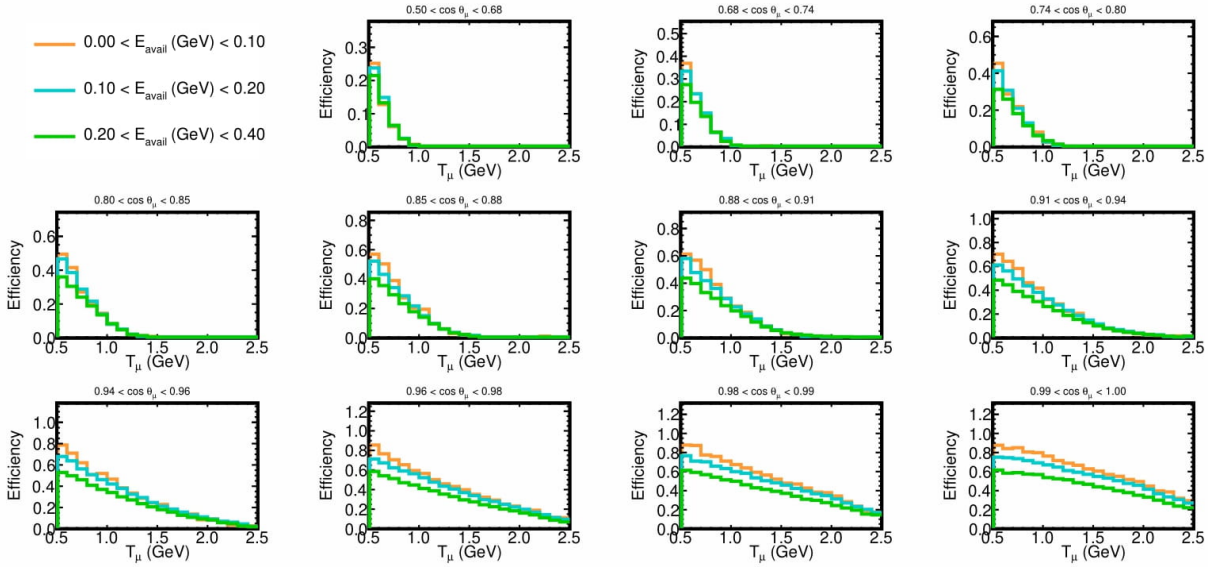

Figure 25: The efficiency when only the Quality Cut is absent

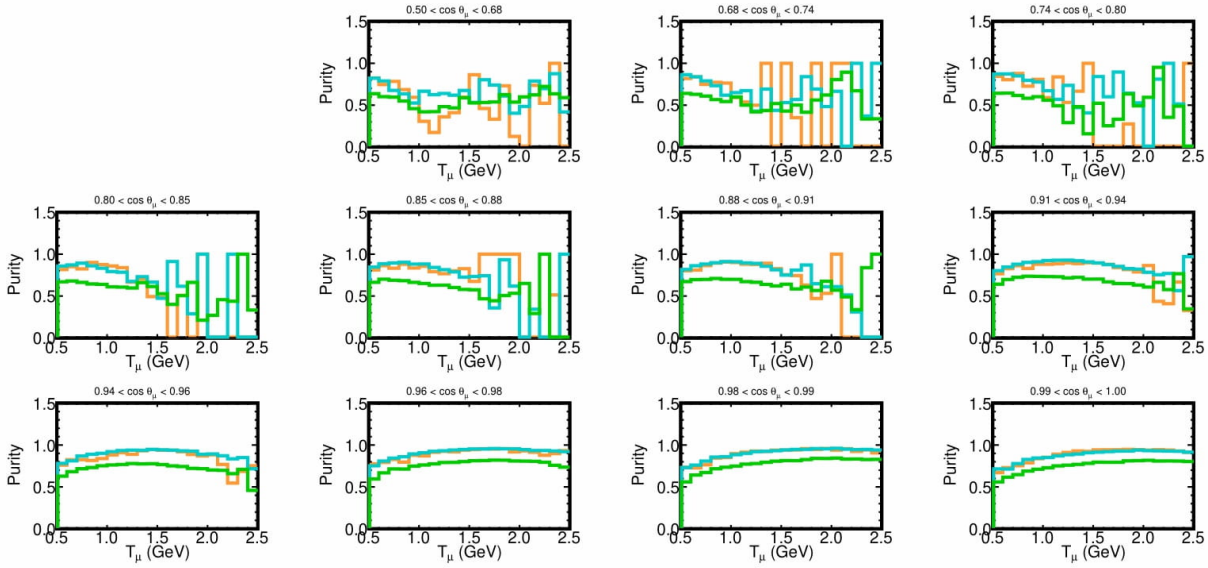

Figure 26: The purity when only the Quality Cut is absent

The second cut applied in the selection during this calculation is the Fiducial Cut. When only the Fiducial Cut is applied, the efficiency is 0.82 and the purity is 0.21. When only the Fiducial Cut is absent, the efficiency is 0.21 and the purity is 0.42. Figures 27 and 28 show the efficiency and purity when only the Fiducial Cut is applied. Figures 29 and 30 show the efficiency and purity

when only the Fiducial Cut is absent.

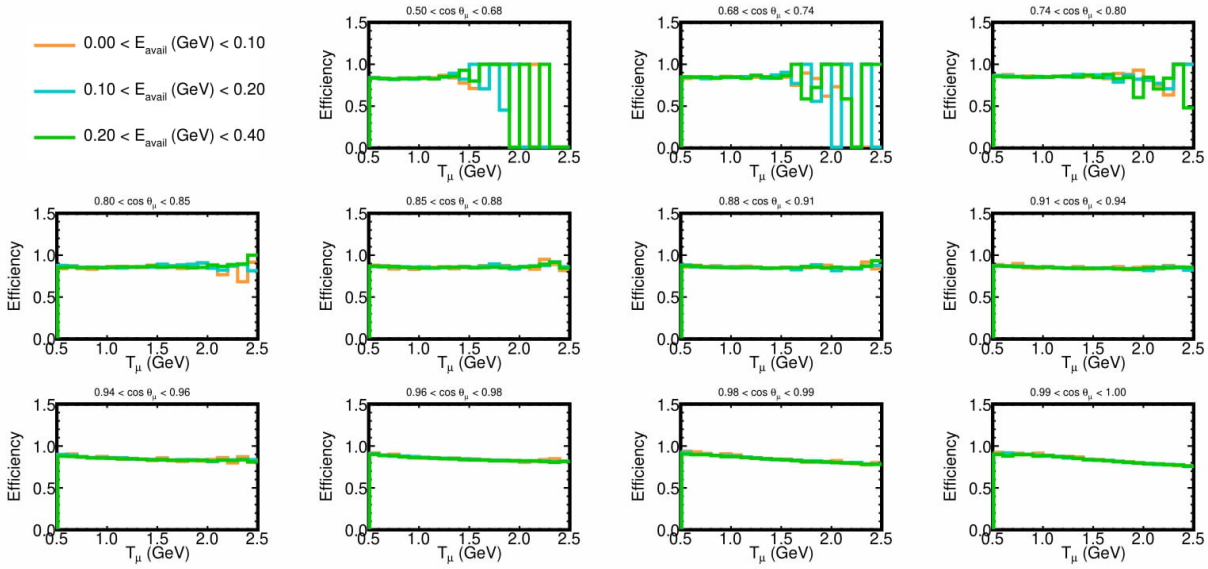

Figure 27: The efficiency when only the Fiducial Cut is applied

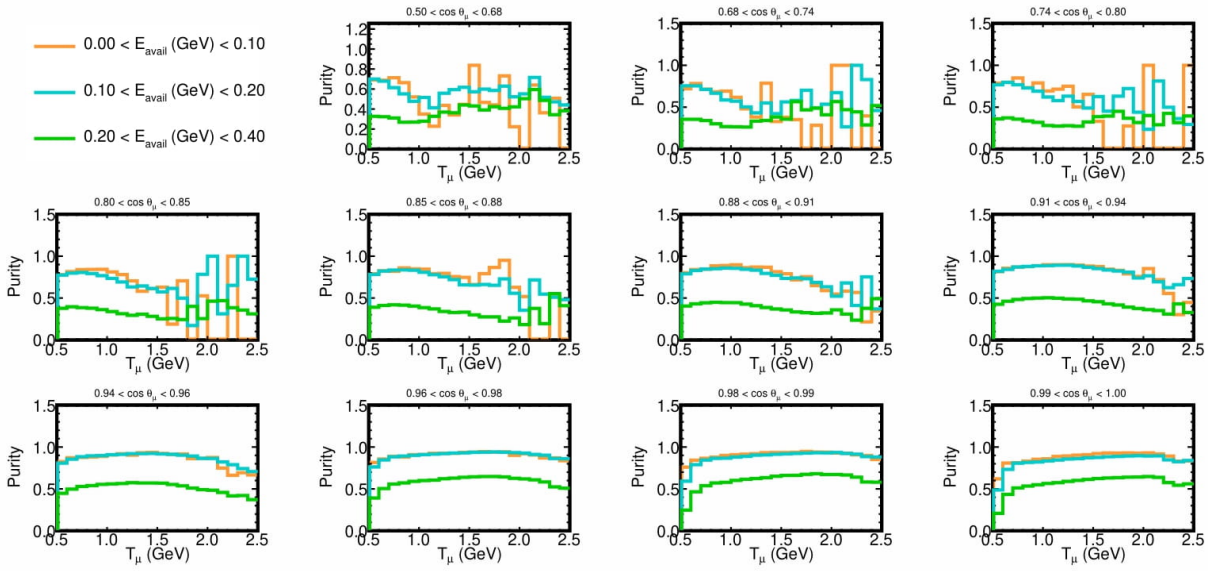

Figure 28: The purity when only the Fiducial Cut is applied

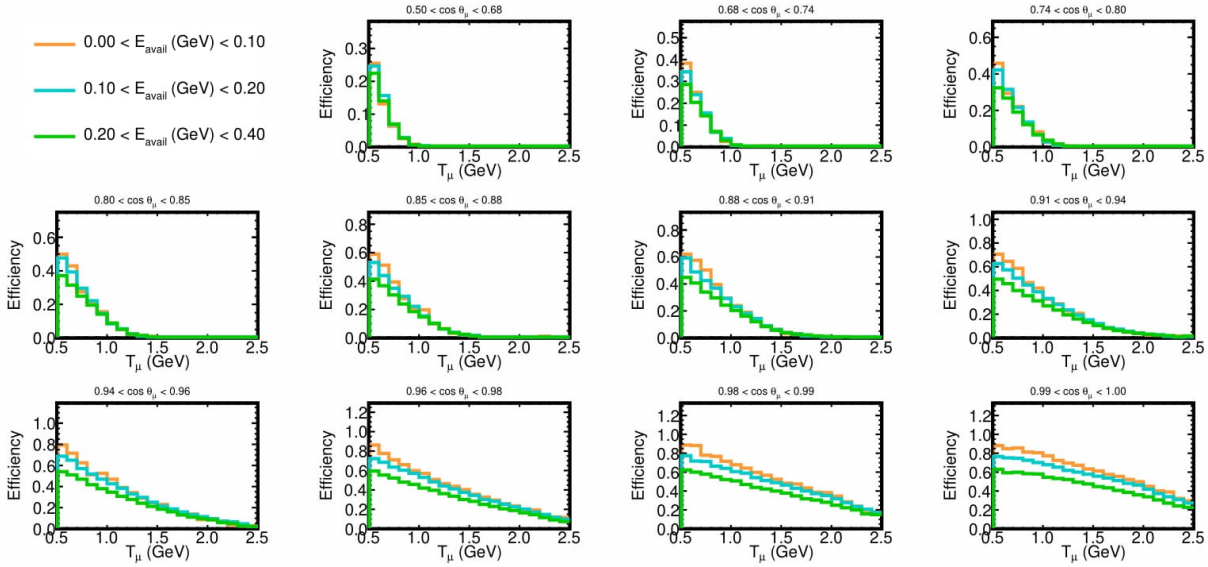

Figure 29: The efficiency when only the Fiducial Cut is absent

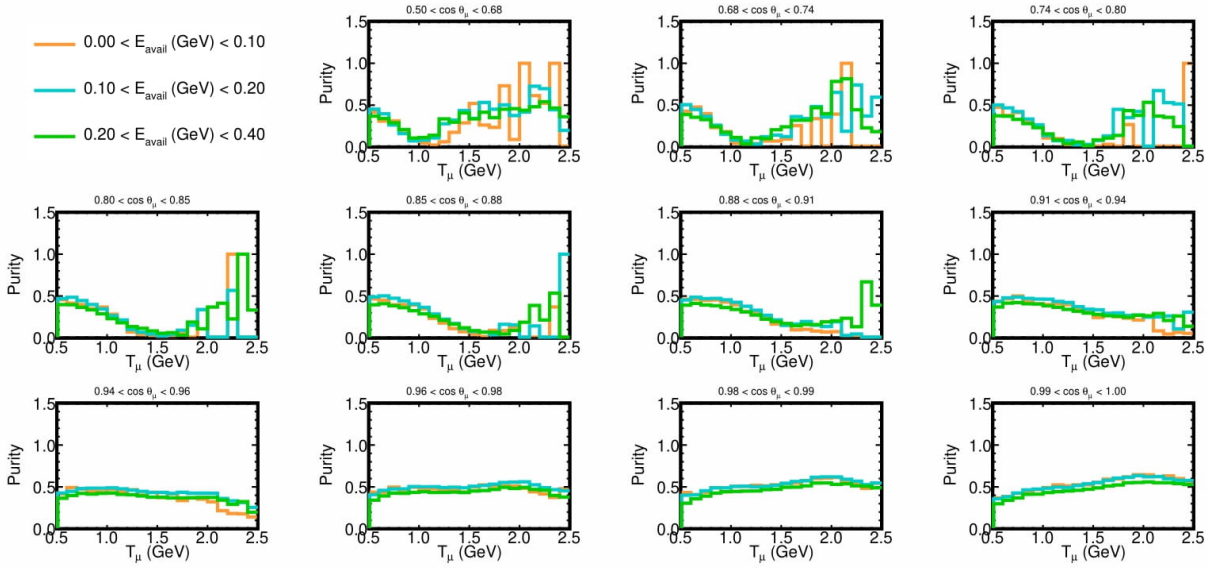

Figure 30: The purity when only the Fiducial Cut is absent

The third cut applied in the selection during this calculation is the Muon ID Cut. When only the Muon ID Cut is applied, the efficiency is 0.78 and the purity is 0.090. When only the Muon ID Cut is absent, the efficiency is 0.21 and the purity is 0.64. Figures 31 and 32 show the efficiency and purity when only the Muon ID Cut is applied. Figures 33 and 34 show the efficiency and purity

when only the Muon ID Cut is absent.

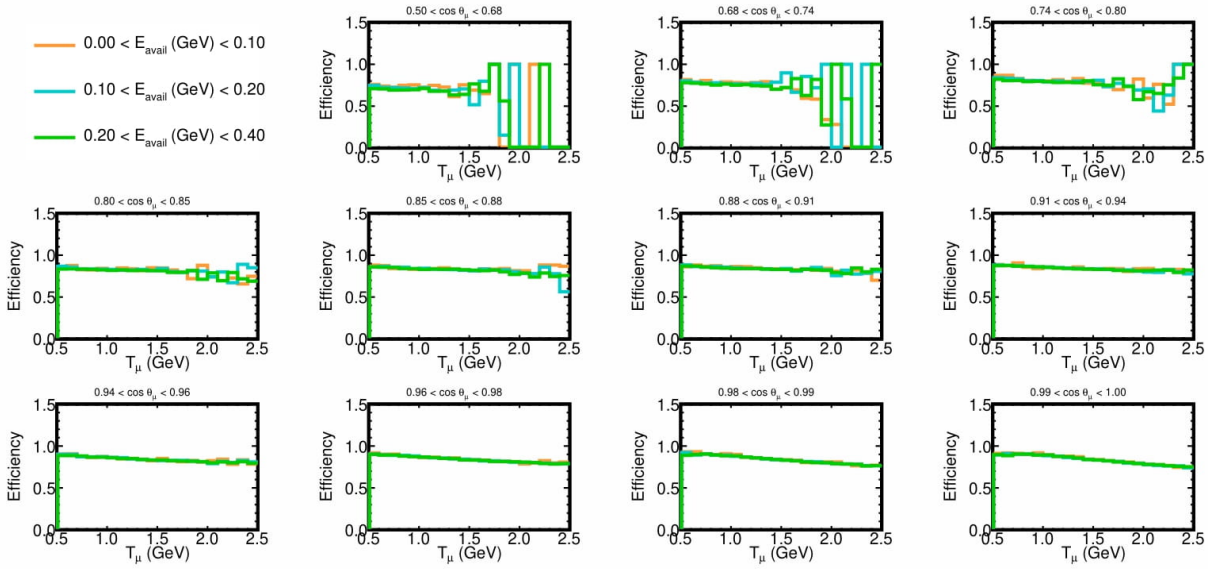

Figure 31: The efficiency when only the Muon ID Cut is applied

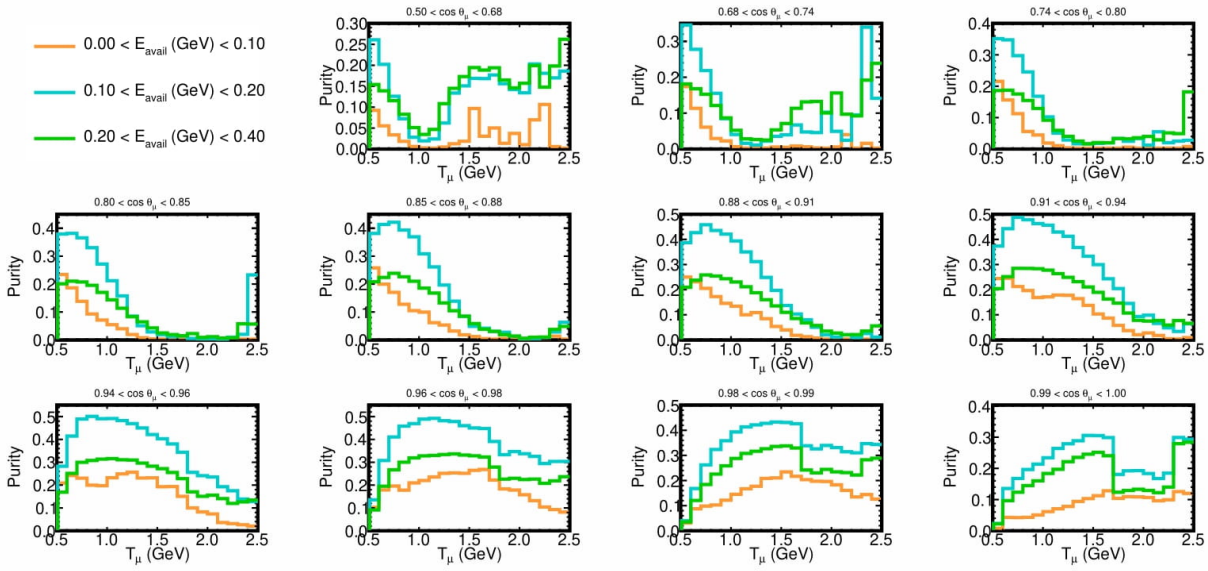

Figure 32: The purity when only the Muon ID Cut is applied

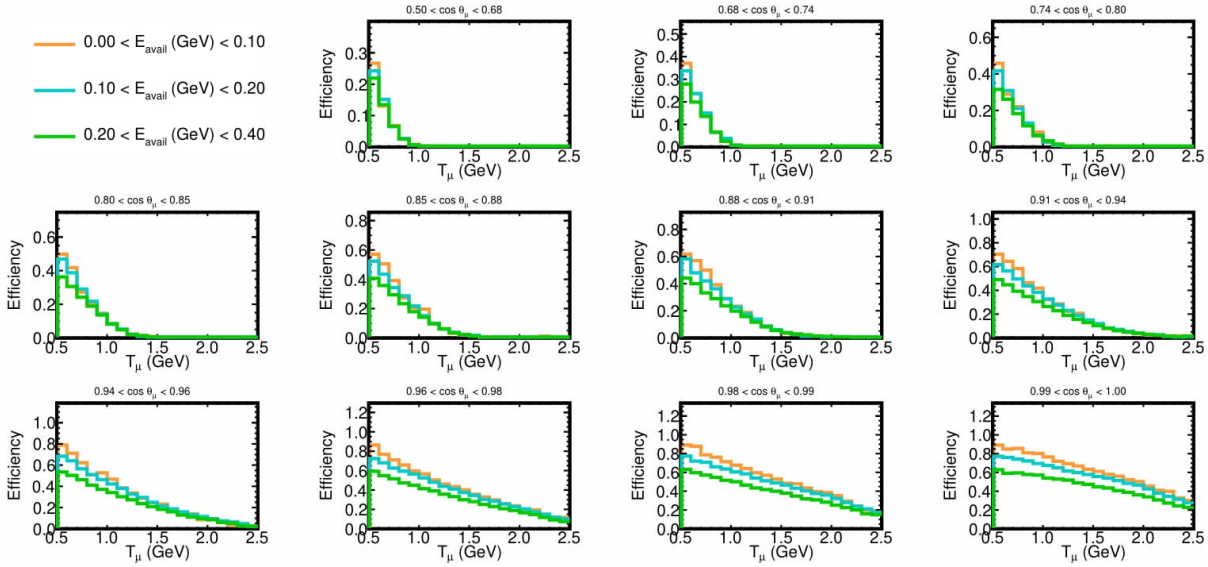

Figure 33: The efficiency when only the Muon ID Cut is absent

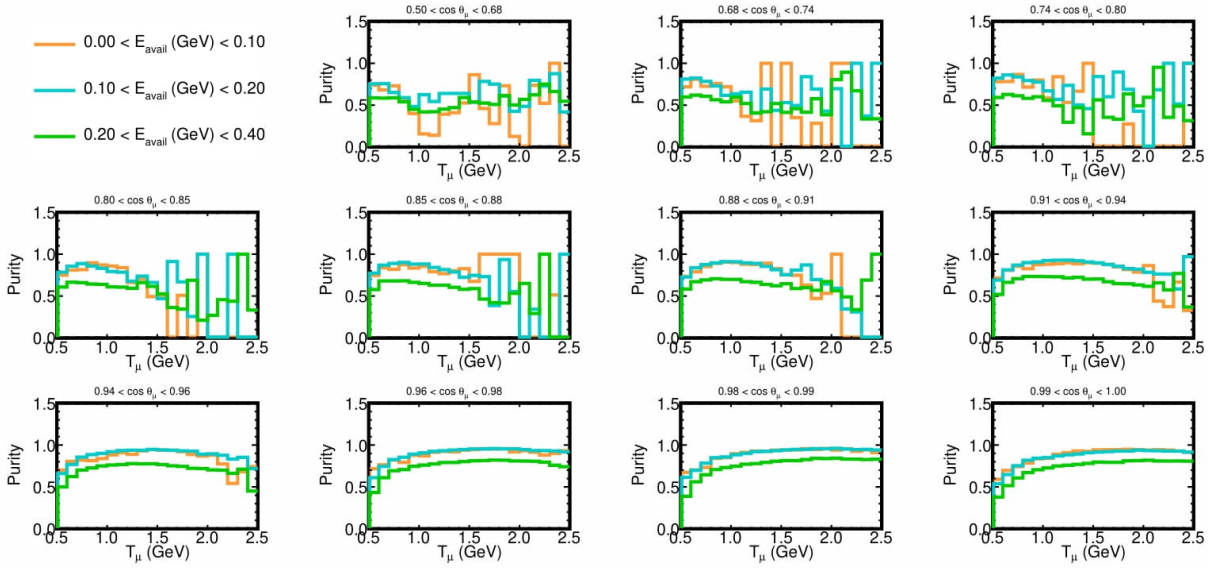

Figure 34: The purity when only the Muon ID Cut is absent

The fourth cut applied in the selection during this calculation is the Containment Cut. When only the Containment Cut is applied, the efficiency is 0.29 and the purity is 0.12. When only the Containment Cut is absent, the efficiency is 0.57 and the purity is 0.77. Figures 35 and 36 show the efficiency and purity when only the Containment Cut is applied. Figures 37 and 38 show the

efficiency and purity when only the Containment Cut is absent.

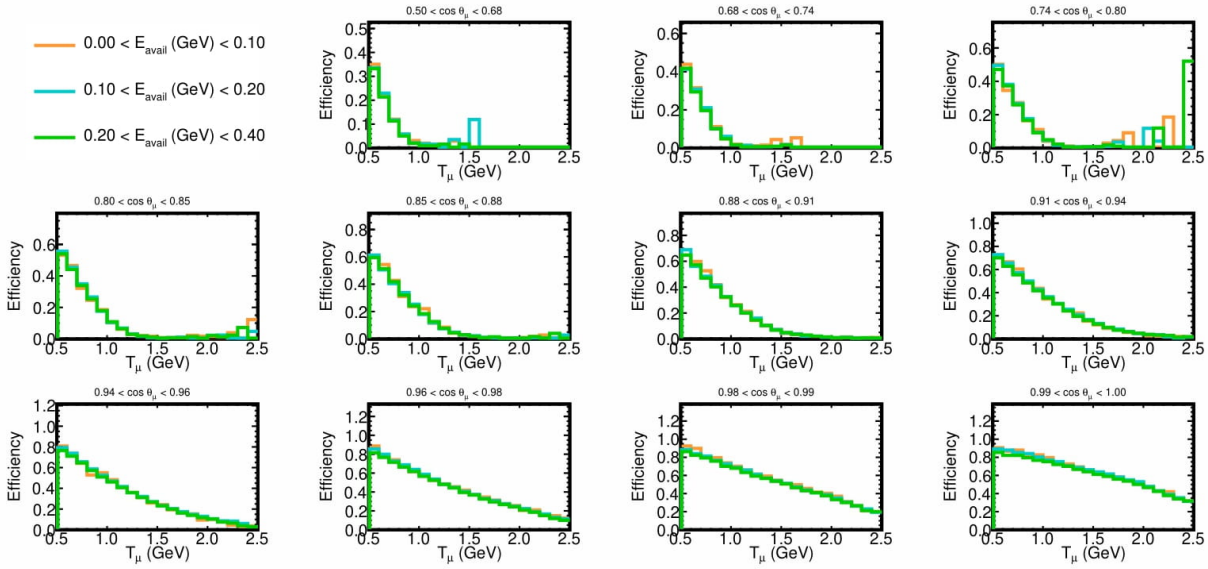

Figure 35: The efficiency when only the Containment Cut is applied

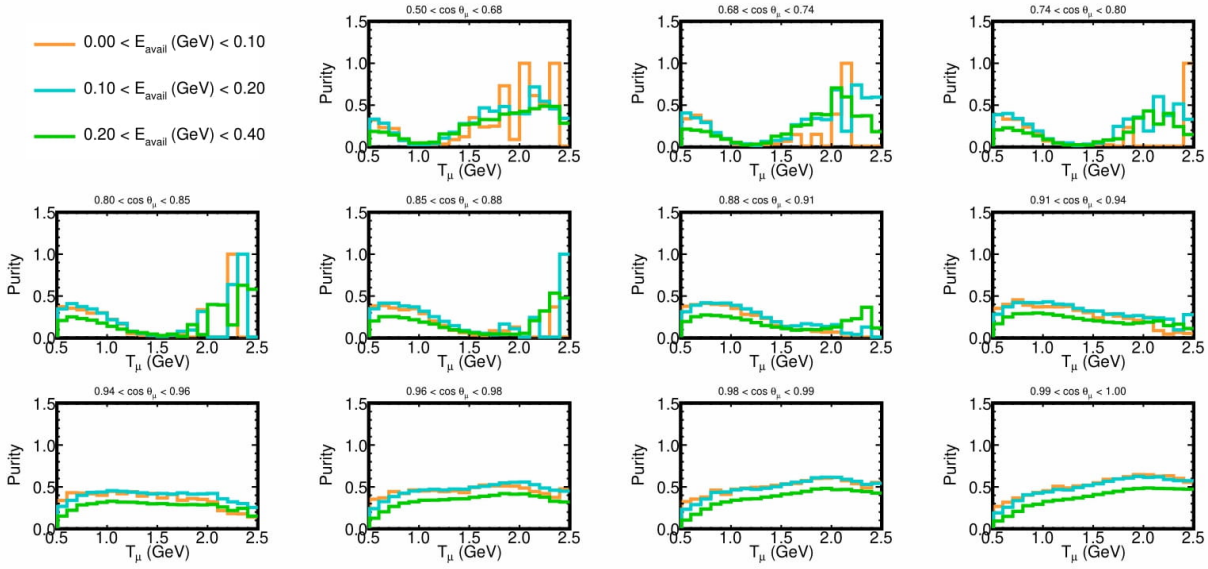

Figure 36: The purity when only the Containment Cut is applied

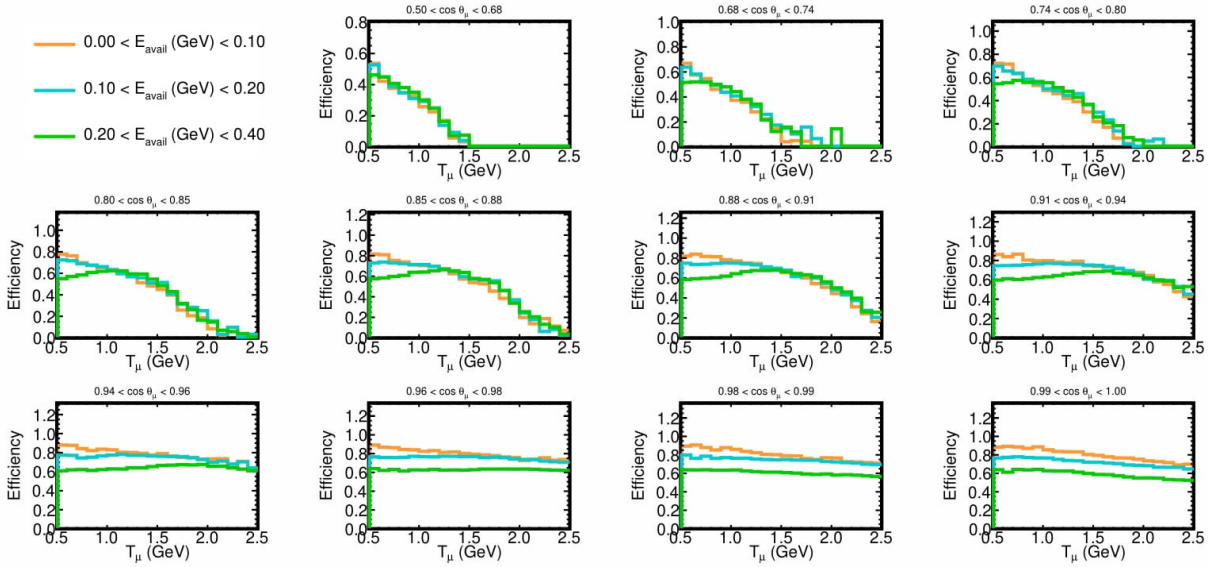

Figure 37: The efficiency when only the Containment Cut is absent

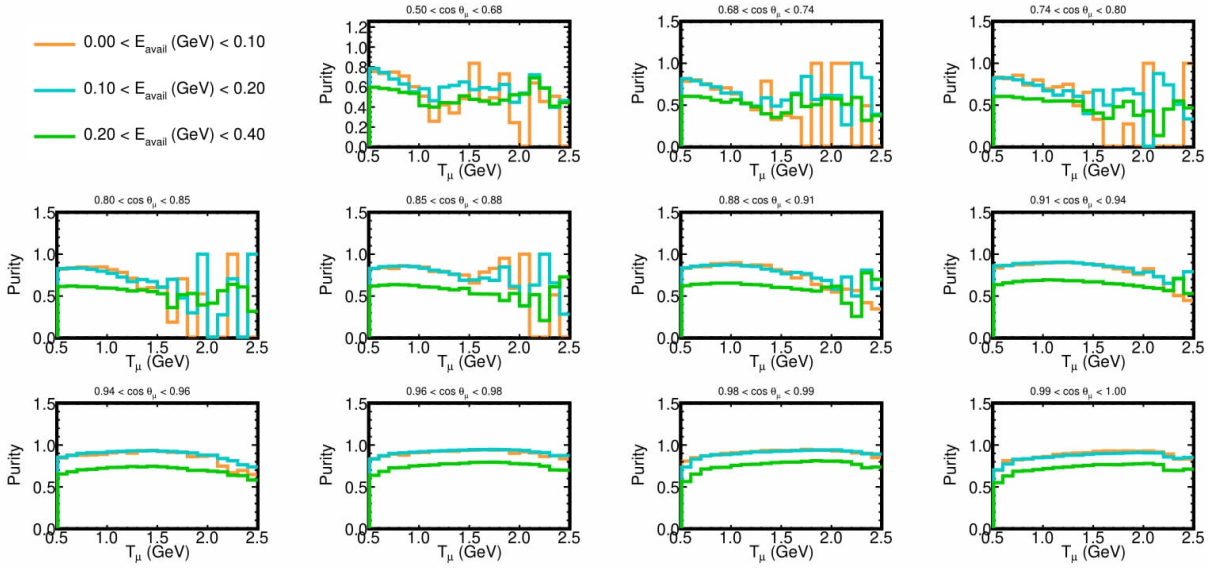

Figure 38: The purity when only the Containment Cut is absent

The fifth cut applied in the Selection during this calculation is the One Track Cut. When only the One Track Cut is applied, the efficiency is 0.70 and the purity is 0.11. When only the One Track Cut is absent, the efficiency is 0.26 and the purity is 0.44. Figures 39 and 40 show the efficiency and purity when only the One Track Cut is applied. Figures 41 and 42 show the efficiency and

purity when only the One Track Cut is absent.

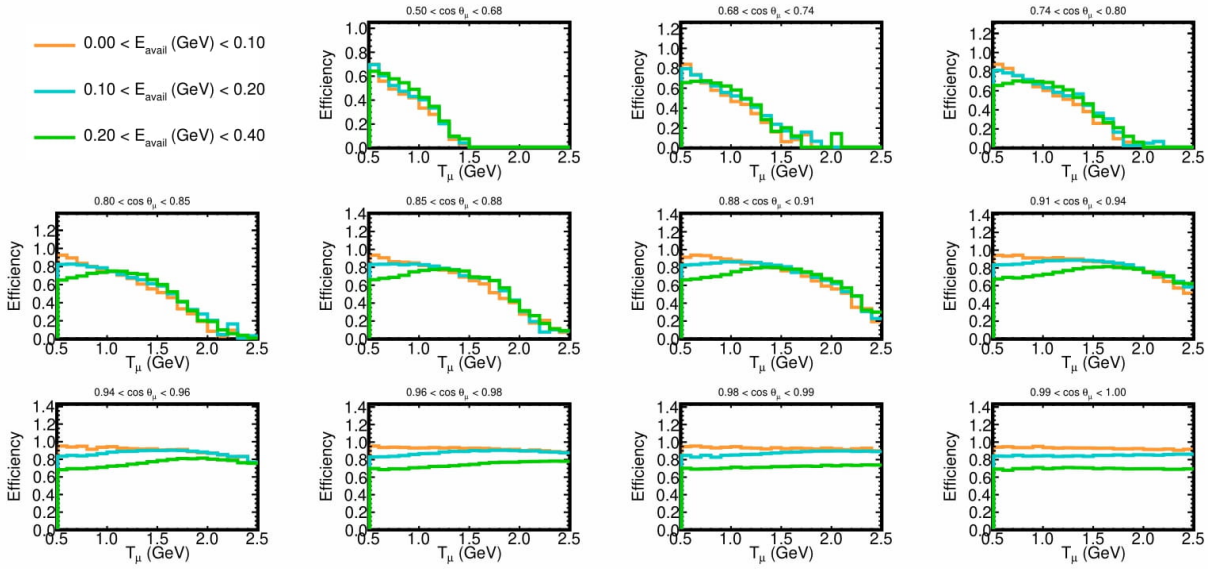

Figure 39: The efficiency when only the One Track Cut is applied

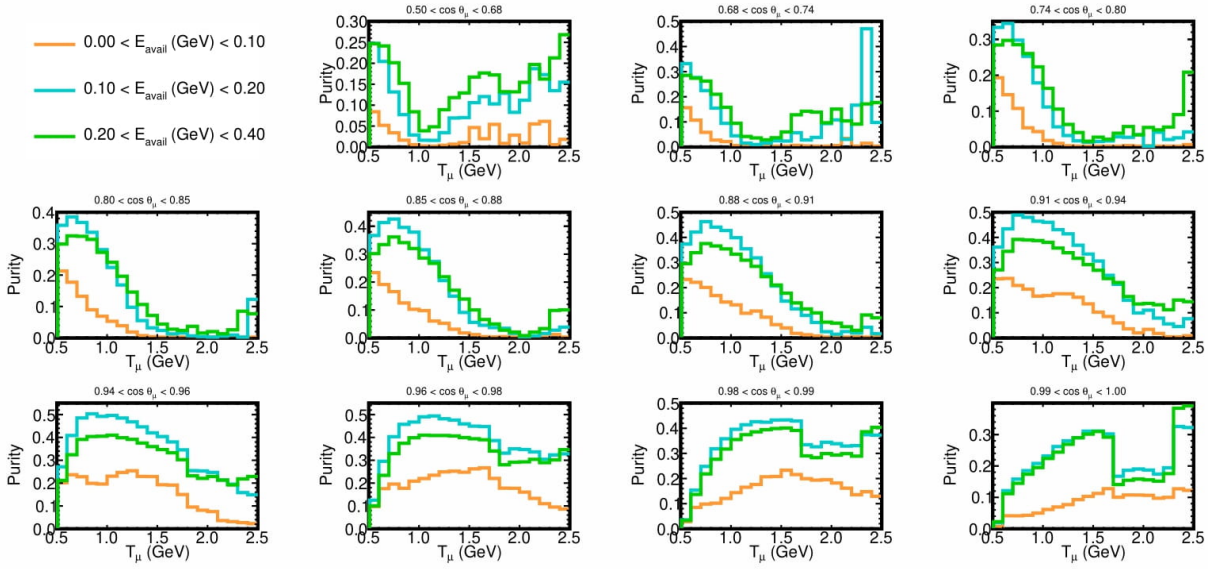

Figure 40: The purity when only the One Track Cut is applied

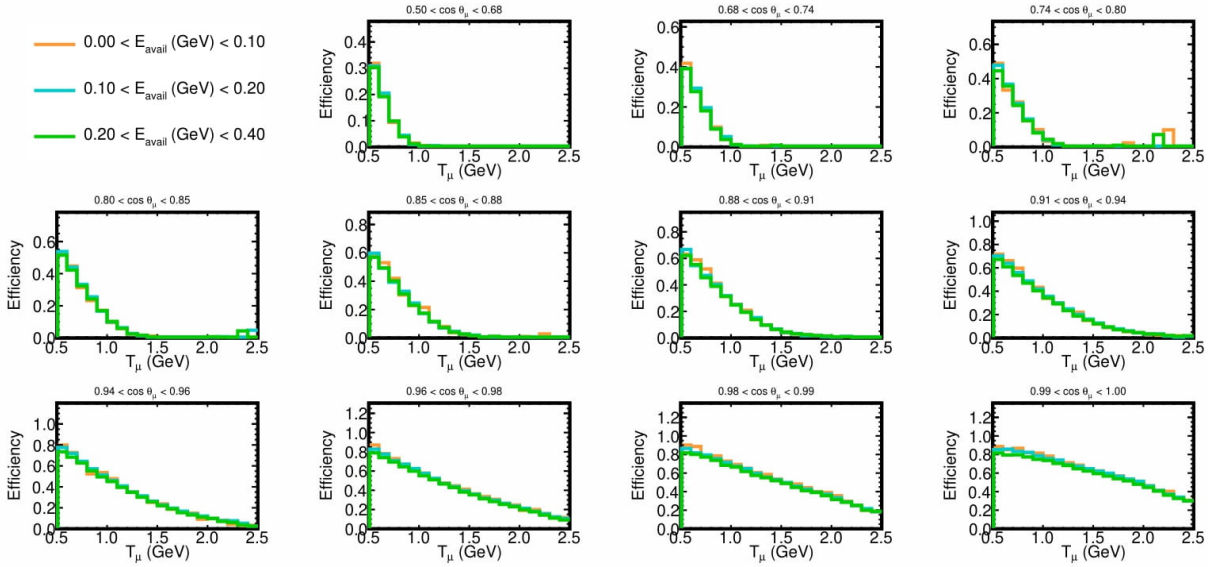

Figure 41: The efficiency when only the One Track Cut is absent

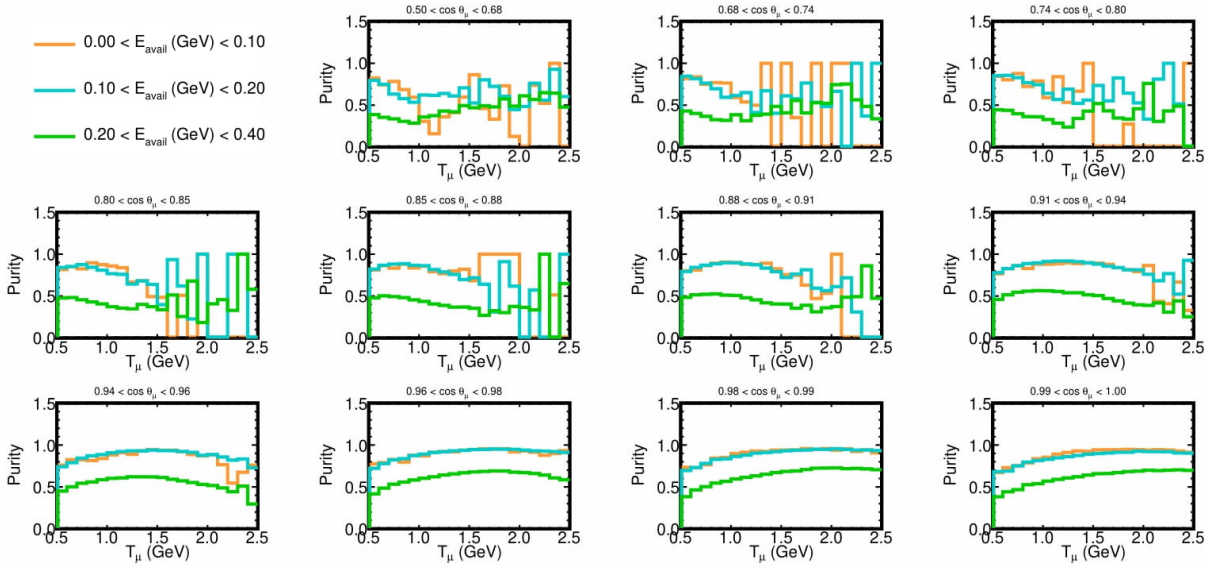

Figure 42: The purity when only the One Track Cut is absent

Table 4 and 5 shows efficiencies and purities of the different cuts respectively. The Containment Cut has the largest impact on the efficiency, but the Fiducial Cut has the largest impact on the Purity.

Table 4: The efficiencies when each cut is sole cut present or absent in the selection.

Cut	Solo Cut Eff.	n - 1 Cuts Eff.
No/Full	0.97	0.21
Quality Cut	0.94	0.21
Fiducial Cut	0.82	0.21
Muon ID Cut	0.78	0.21
Containment Cut	0.29	0.57
Kalman Cut	0.70	0.26

Table 5: The purities when each cut is sole cut present or absent in the selection.

Cut	Solo Cut Pur.	n - 1 Cuts Pur.
No/Full	0.059	0.80
Quality Cut	0.068	0.79
Fiducial Cut	0.21	0.42
Muon ID Cut	0.090	0.64
Containment Cut	0.12	0.77
Kalman Cut	0.11	0.44

5.4 Low Hadronic Activity Development

This analysis is concerned with a particular regime of the $\nu_\mu CC$ interaction. The low hadronic activity sample is defined as a $\nu_\mu CC$ interaction where outgoing protons and pions have capped kinetic energies; the cap is 250 MeV for Protons and 175 MeV for Pions [5].

Previous analysis determined that interaction modes of the $\nu_\mu CC$ interaction are dependent on the hadronic energy, as can be seen in Figure 43.

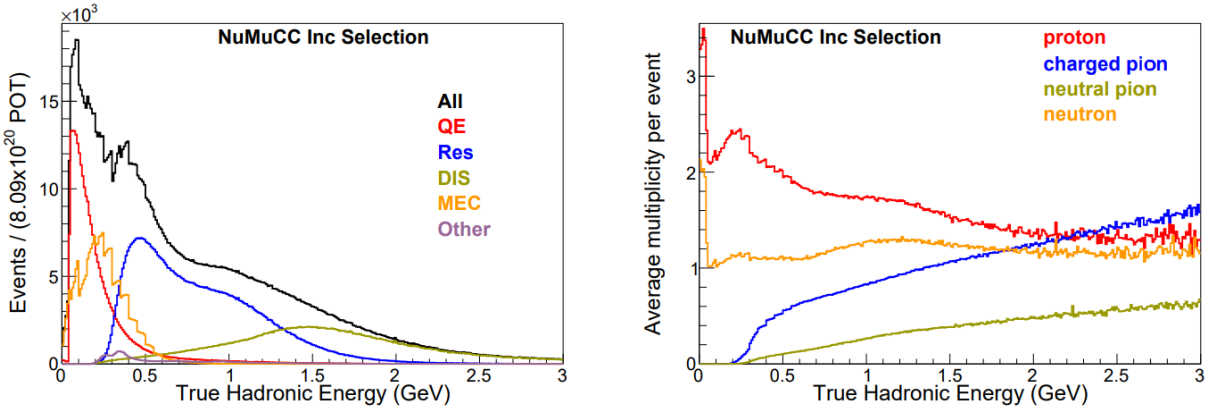

Figure 43: Left: Number of simulated $\nu_\mu CC$ events by interaction mode as a function of the hadronic energy. QE and MEC dominate until about 0.4 GeV. Right: The multiplicity of final state particles for the same events as a function of hadronic energy [28].

A regime to study QE and MEC interactions was desired, but the hadronic energy is not a direct observable, instead a choice on the number of tracks seen in the detector was chosen [28]. More energetic hadrons produce more activity in the detector, which leads to a higher probability of more tracks in the detector [28]. Analysis determined that $\nu_\mu CC$ events with only one track were more likely to be QE or MEC, while events with more than one track were more likely to be RES or DIS, as can be seen in Figure 44.

$\nu_\mu CC$ events with one track became the choice for selection for low hadronic activity sample. The next step was to establish a signal definition (choosing events from simulation that best describe the physical phenomena that the analysis is trying to study) suited to match this definition of selection that would allow for minimal uncertainty on the cross-section [28].

A primary search was done by looking at the kinetic energy of particles in simulated events. Figure 45 shows the kinetic energy of the hadron with the highest kinetic energy in each $\nu_\mu CC$ event. The distribution of events is split between events with only one track and events with two or more tracks, and split further by the type of particle that has the maximum kinetic energy. It can be seen that events that had two or more tracks have a higher maximum kinetic energy for protons or pions than events with only one track. A primary condition of a maximum of 0.5 GeV for proton and pion kinetic energies was made based on this [28].

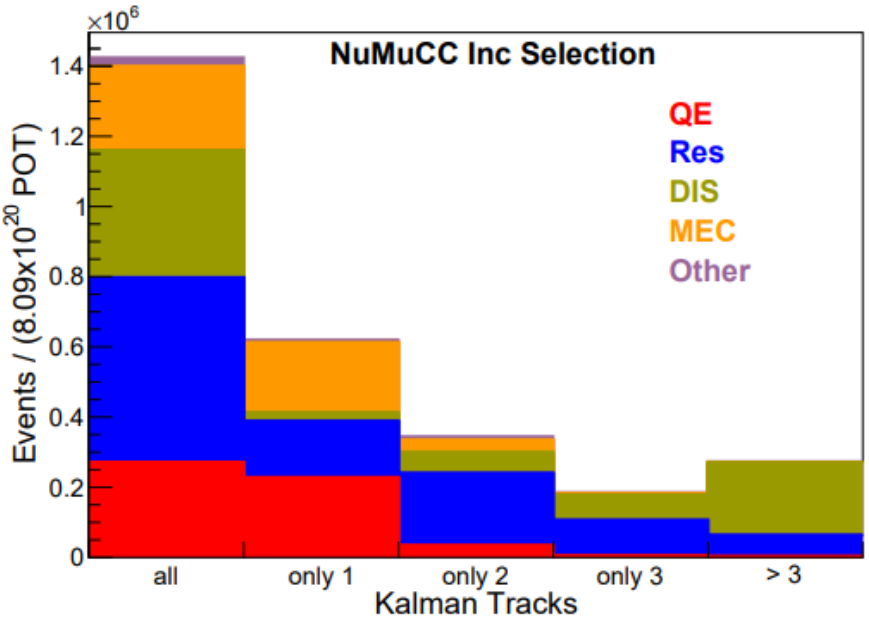

Figure 44: The number of $\nu_\mu CC$ events and the ratios of their interaction modes as a function of the number of particles with high enough energies to be seen in the detector [28].

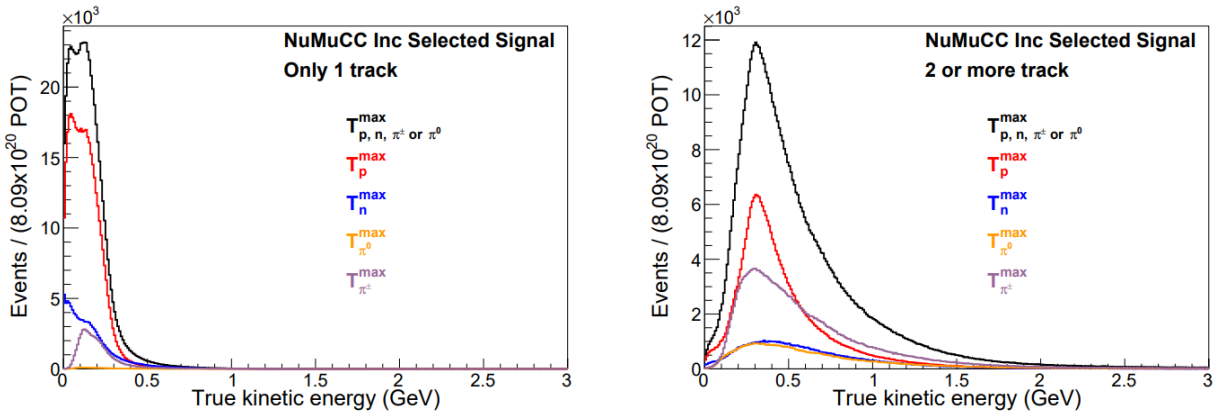

Figure 45: Maximum kinetic energy distribution of the $\nu_\mu CC$ events. Black represents the total number of events, the colored lines represent which particle had the maximum kinetic energy by event. Left: events where only one particle has enough energy to be seen in the detector. Right: events where more than one particle has enough energy to be seen in the detector [28].

Figure 46 shows the relationship between maximum proton and pion kinetic energies allowed for a signal definition in simulated events and the number of Signal $\nu_\mu CC$ events [28]. In the left picture is the total number of Signal $\nu_\mu CC$ events, while on the right is the number of $\nu_\mu CC$ events

that have one track. The number of events increases monotonically with maximum allowed proton kinetic energy, but number of events with one track rises rapidly up until the 0.2-0.3 GeV range where the rise becomes much slower. This means that events above that range are mostly events with more than one track.

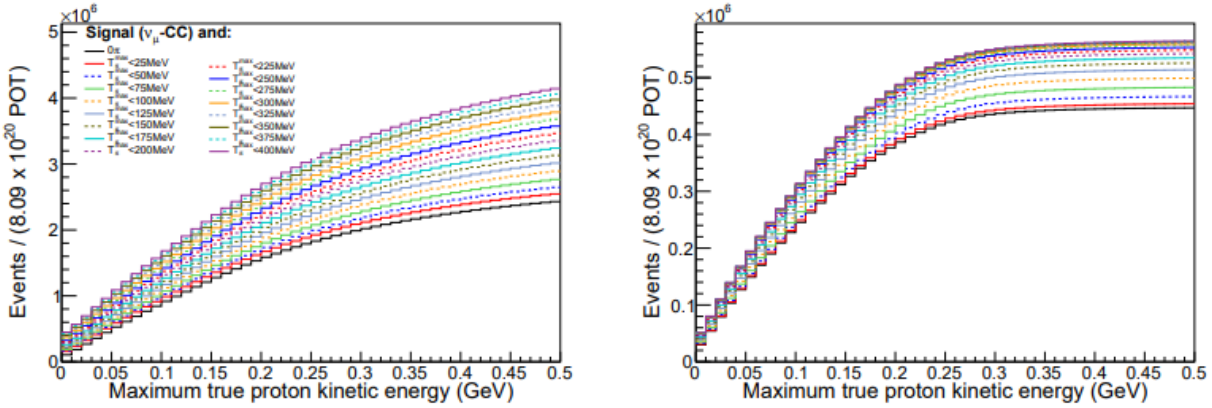

Figure 46: $\nu_\mu CC$ event yields as function of maximum proton kinetic energy. Each line represents event yield for a different maximum pion kinetic energy. Left: All $\nu_\mu CC$ events. Right: $\nu_\mu CC$ events where one particle has enough energy to be seen in the detector [28].

The efficiency (measure of how many Signal events would be selected) and purity (measure of how many selected events are signal) was measured for different maximum kinetic energies for protons and pions. Figure 47 shows the efficiency and expected uncertainty on the efficiency; expected uncertainty is higher for low energies, finds a minimum in the range of 150 - 300 MeV for both particles, and increases at higher ranges.

Figure 48 shows the purity mapping for all choices of maximum kinetic energies for protons and pions [28]. The left picture shows that the purity increases monotonically with increasing maximum kinetic energies. The right picture shows that the uncertainties are higher for lower energies, but becomes almost flat after a maximum of 250 MeV for proton kinetic energy for all pion thresholds.

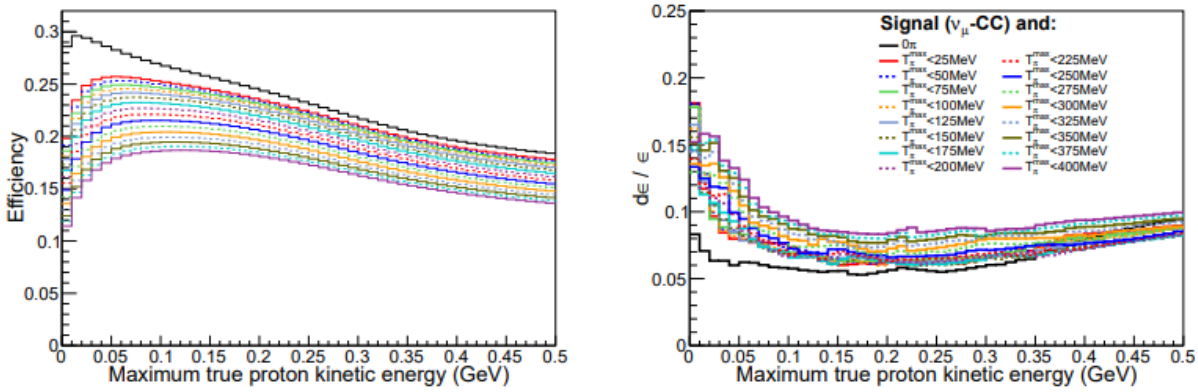

Figure 47: Map of efficiency of different signal definitions for $\nu_\mu CC$ events with one track, based on different maximum values for proton and pion kinetic energies. Left: plot of efficiency, Right: plot of expected systematic uncertainty on the efficiency [28].

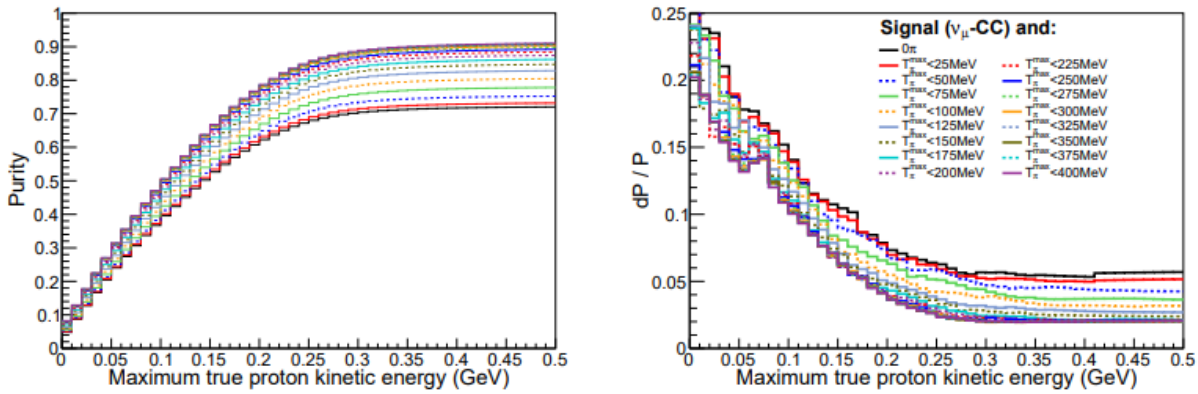

Figure 48: Map of purities of different signal definitions for $\nu_\mu CC$ events with one track, based on different maximum values for proton and pion kinetic energies. Left: plot of purities, Right: plot of expected systematic uncertainty on the purity [28].

The final choice was made based on the expected uncertainty on the cross-section. Figure 49 shows the expected uncertainty based on the maximum allowed values for the proton and pion kinetic energies. For lower energies the purity is the dominant driver of uncertainty, while for higher energies the efficiency is [28]. The uncertainty is minimized in the region where both types of particles have a maximum kinetic energy between 150 MeV and 300 MeV. The combination that produced the minimum value for expected cross-section was a pion maximum kinetic energy of 175 MeV and a proton maximum kinetic energy of 250 MeV. Thus the low hadronic activity signal

definition became a $\nu_\mu CC$ event where all protons and pions produced have less than 250 MeV and 175 MeV kinetic energies respectively [28]

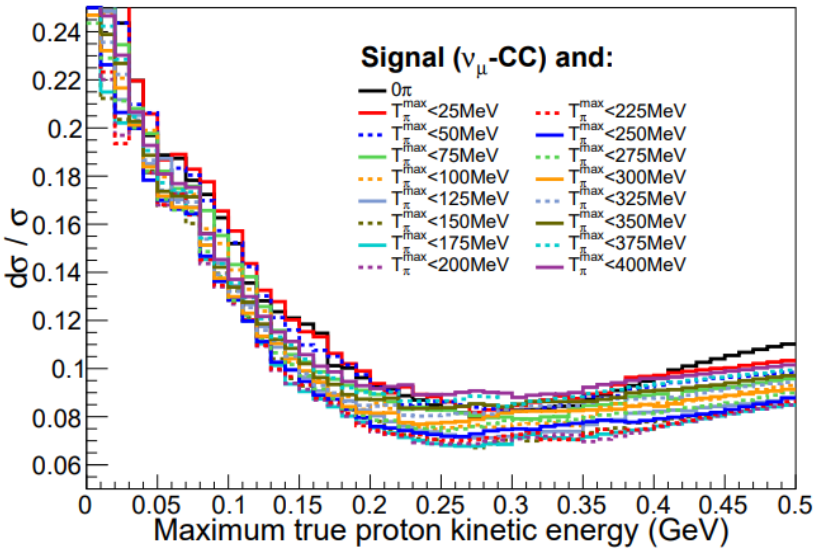

Figure 49: Map of expected uncertainty on the cross-section of different signal definitions for $\nu_\mu CC$ events with one track, based on different maximum values for proton and pion kinetic energies [28].

Figure 50 shows a picture of what a $\nu_\mu CC$ with Low Hadronic Activity event looks like in the NOvA Near Detector. There is a single track left by the muon and no other particle.

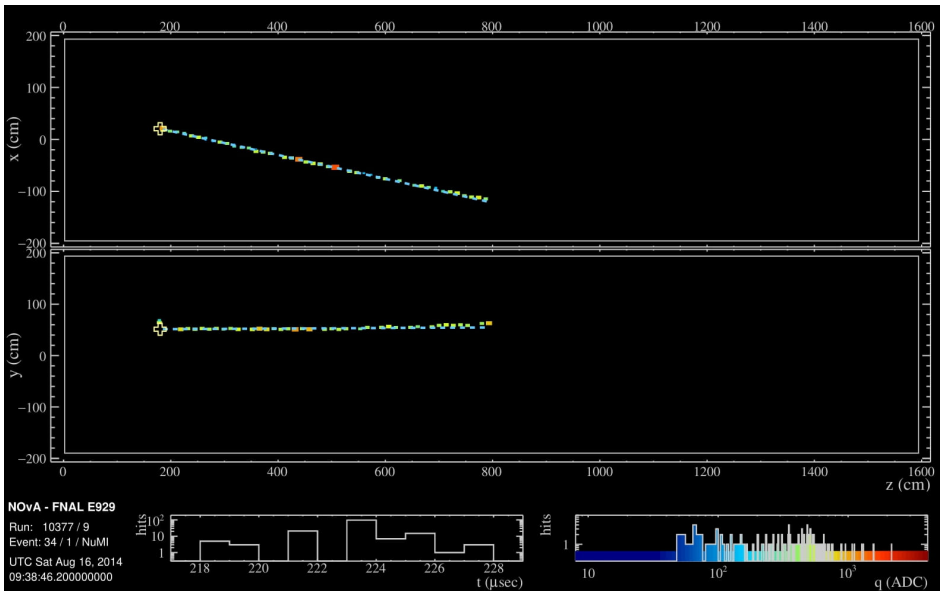

Figure 50: Diagram of a simulated $\nu_\mu CC$ event with low hadronic activity. The multicolored line represents the detector response for the muon, the only charged particle coming out of the interaction with enough kinetic energy to leave a trace in the detector. The blue dashed line represents the true path of the simulated muon. Two views are necessary to reconstruct the 3D path in the detectors. Top: the XZ view, Bottom: the YZ view.

6 Available Energy and Bin Determination

The cross-section of the charged current muon neutrino interaction is dependent on the energy of the incoming neutrino. However, there are limitations on reconstructing the neutrino energy directly. To reduce the model dependence of this analysis, the differential cross-section is measured with regards to variables that are generally well-modeled in neutrino generators. This analysis measures the triple differential cross-section of the charged current muon neutrino interaction. Two of the variables in the differential describe the lepton kinematics. The angle and kinetic energy of the outgoing muon are a standard metric to model neutrino cross-sections [28]. The muon energy is related to the length of muon track in the detector [31].

The third variable describes energy transferred to final state particles. Limitations in measuring energy transfer directly come from model dependence in corrections due to final-state interactions [34]. A closely related observable was defined, "the hadronic energy available to produce activity in the detector called E-Avail" [34].

E-Avail was defined by the MINERvA collaboration [34]. E-Avail in an event is defined as the sum of energies of particles other than the outgoing muon and nucleus. These include [35]:

- The kinetic energies of all final state protons and charged pions produced in the interaction.
- The total energies of all final state neutral pions, photons, electrons and kaons. The energies of the pions, photons and electrons appear as electron showers, while the kaons appear as ionizations from the K^0, $K^{\pm}$ decay
- The total energy minus proton mass for hyperons. These energies appear as ionizations from the hyperon decay.
- The total energy plus proton mass for anti-nucleons. These energies appear as the result of the neutron-antinucleon annihilation.

The muon kinematics and E-Avail can then be mapped to neutrino energy [31].

E-Avail allows for QE and 2p2h events to be separated from resonant pion production events and DIS events [34]. The selection cuts described in a previous section leads to a higher ratio of low E-Avail events, which leads to a higher ratio of QE and MEC events and a lower ratio of resonance and DIS events.

6.1 Modeling Reconstructed Available Energy

Visual Hadronic Energy (Vis-Had E) is defined as the sum of the energy deposited by all hits not associated with the muon track and the energy of the muon track that exceeds minimum ionizing values [31]. E-Avail is a variable related to the deposited hadronic energy. Particles do not all deposit energy into the detector the same (for example: different types of particles have different dE/dx curves). An event's reconstructed Vis-Had E is correlated with its True E-Avail. This relationship can be used to define a reconstructed E-Avail variable.

A 2D histogram of the selected signal events in bins of true E-Avail versus reconstructed Vis-Had E is made. Two sets of points are made; one using the median value of true E-Avail for each reconstructed Vis-Had E bin versus the median point of each reconstructed Vis-Had E bin, the other uses the mean value of true E-Avail instead. For each set of points, five different fitting functions are tested. These functions fit reconstructed Vis-Had E to either the mean or median true E-Avail in increasing polynomial terms (e.g. Mean Pol-3 Fit would mean $E - Avail_{mean} = A * (E^{reco}_{vishad})^3 + B * (E^{reco}_{vishad})^2 + C * (E^{reco}_{vishad})$). Then the best fitting parameters are found in each case. Figure 1 shows the 2D histogram of the selected signal events overlaid with the fits to the mean of true E-Avail. Figure 2 shows the same 2D histogram overlaid with the fits to the median of true E-Avail. Of these ten outcomes, the most appropriate one is chosen based on criteria in the next section.

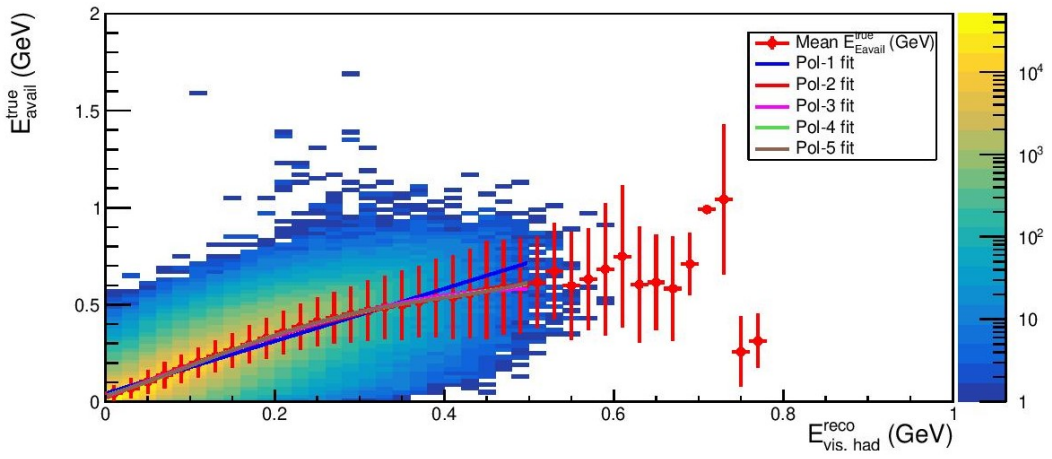

Figure 51: 2D histogram of all Selected Signal events. Their true E-Avail is plotted against their reconstructed Vis-Had E. Polynomials fits up to order 5 are made between the mean of each E-Avail bin and the center of each reconstructed Vis-Had E bin

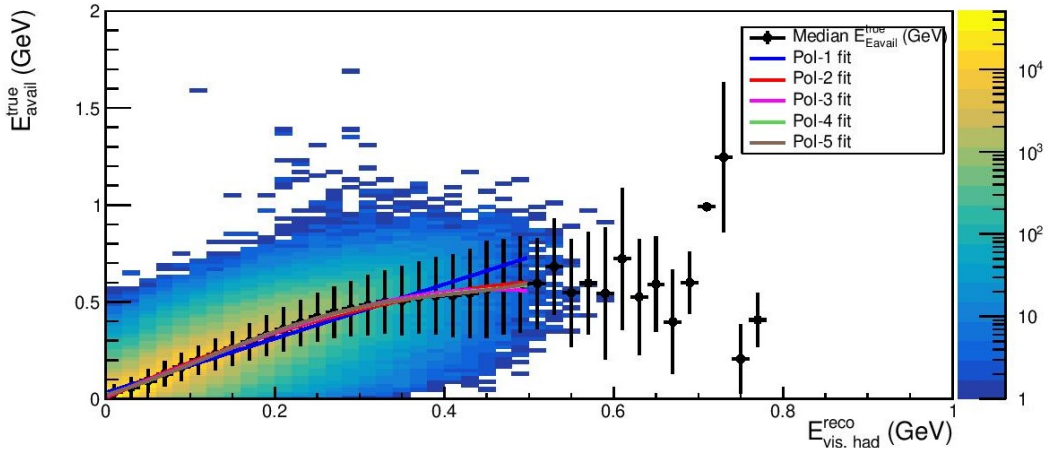

Figure 52: 2D histogram of all Selected Signal events. Their true E-Avail is plotted against their reconstructed Vis-Had E. Polynomials fits up to order 5 are made between the median of each E-Avail bin and the center of each reconstructed Vis-Had E bin

6.2 Resolution

The metric used to choose which polynomial fit to use as the definition of reconstructed E-Avail is the resolution of E-Avail.

To determine the resolution of the different fits, histograms of the difference between true E-Avail and reconstructed E-Avail for each event is made for each definition of reconstructed E-Avail.

The selected signal events are arranged into sets of histograms. They are arranged into a set of fine bins (called E-Avail finer bins) for each definition of reconstructed E-Avail. And they are arranged by the difference between their reconstructed E-Avail and true E-Avail for each definition of reconstructed E-Avail, in a set of bins called E-Avail resolution bins. One histograms is made arranging the selected signal events by their true E-Avail into the finer bins.

- E-Avail finer bins: 240 Bins from 0 to 12 GeV
- E-Avail resolution bins: 4800 Bins from -120 to 120 GeV

The histograms are then arranged into 2D histograms, with one axis always being the true E-Avail of selected signal events, and the other axis is filled by one of the other variables.

For each bin of the true E-Avail axis, a histogram of the difference between reconstructed E-Avail and true E-Avail is made. Figure 53 shows the histogram for one of these bins. The standard deviation of the distribution is used as the Resolution of that bin. The mean of the distribution is used as the bias in that bin. Figure 54 shows the resolution for each bin for each of the ten fits, while Figure 55 shows the bias in each bin. A Gaussian is also fit to the distribution.

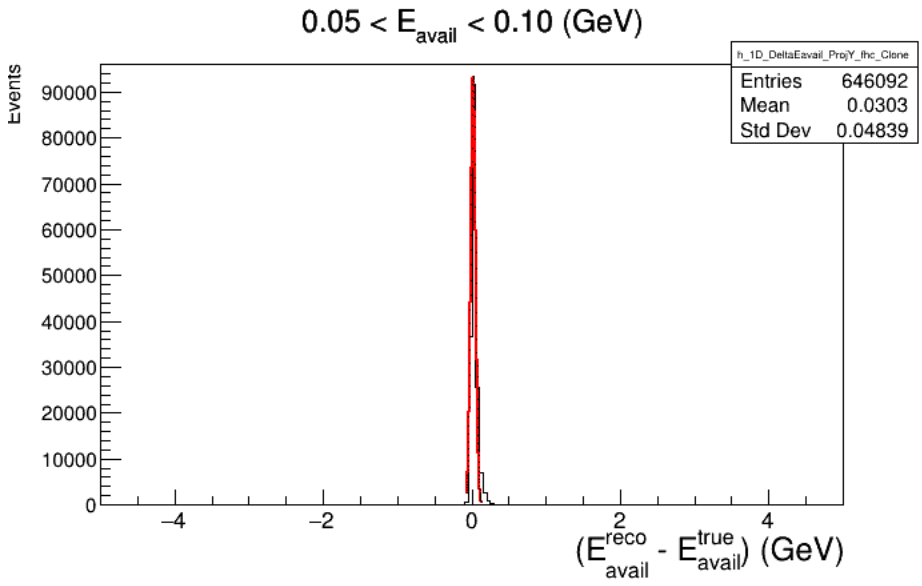

Figure 53: A reconstructed E-Avail - true E-Avail Histogram for all events in the 50 - 100 MeV true E-Avail finer bin

The linear fit to the mean of the true E-Avail was chosen due to its resolution being the lowest at the lower regions of E-Avail. The final formula for reconstructed E-Avail is as follows:

$$E^{Reco}_{Avail} = 0.0421037 + 1.35087(E^{Reco}_{VisHad}) \tag{26}$$

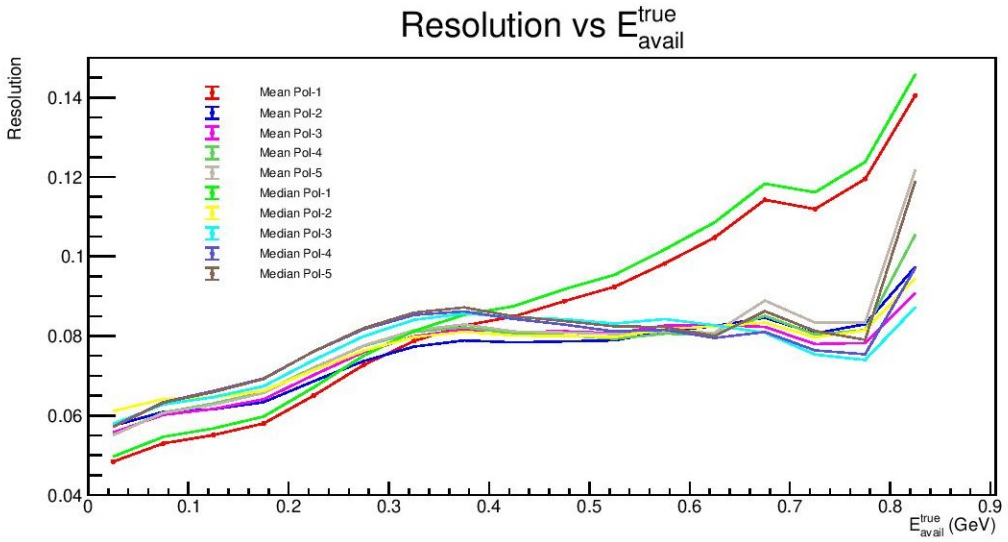

Figure 54: The resolution in each finer bin for each of the ten reconstructed E-Avail fits

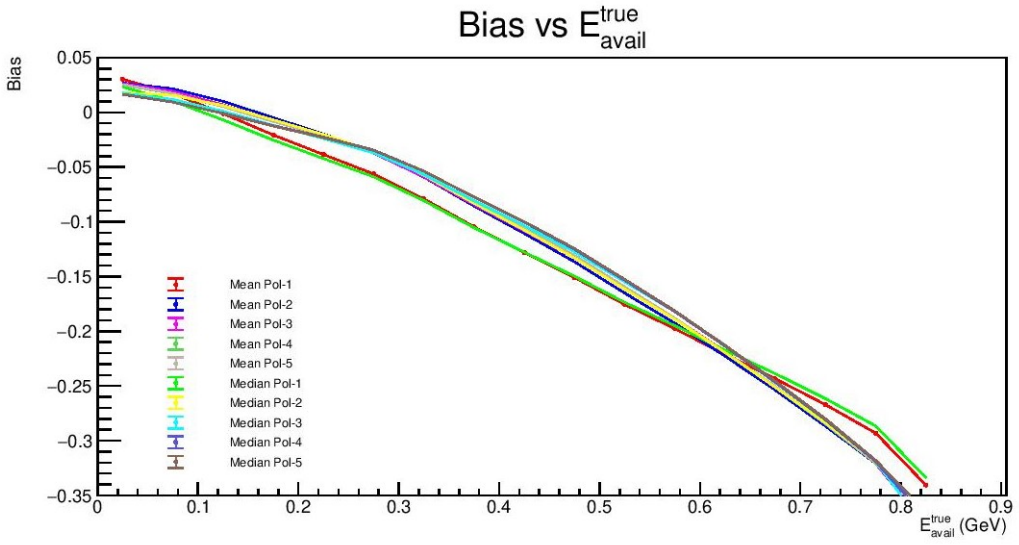

Figure 55: The bias in each finer bin for each of the ten reconstructed E-Avail fits

6.3 Bins

The three variables for the triple differential cross-section measurement are Kinetic Energy of the outgoing Muon (T_μ), Cosine of the Angle of the Outgoing Muon ($\cos\theta_\mu$)), and E-Avail. The binning

for T_μ and $\cos\theta_\mu$) was taken from a $\nu_\mu CC$ inclusive analysis which required that all muon kinematic bins are at least as wide as the resolution estimated from their selected signal events [31]. Table 6 shows the bin edges for the T_μ and $\cos\theta_\mu$) bins.

The choice for E-Avail bins was based on the resolution, bias and statistics. The conditions on choosing bins for the analysis were that the Resolution and the absolute value of the Bias may not exceed sixty percent of the size of the E-Avail bin. Furthermore, their must have at least 1000 selected signal Events. Table 7 shows the resolution and bias for each of the finer bins.

From the size of the resolution and bias, an E-Avail bin size of 100 MeV was chosen for the lowest two E-Avail bin to provide sufficient coverage. After 200 MeV, the size of the resolution is enough to warrant a larger bin. The next bin size chosen was 200 MeV. Less than 3% of selected signal events have a true E-Avail above 0.400 GeV. Therefore the upper-bound for the last analysis bin is 0.400 GeV. Table 8 shows the number of events in each of the E-Avail bins, and what fraction of the total number events lay in each bin.

E-Avail Bins (GeV): {-10, 0.0, 0.100, 0.200, 0.400, 120}

Table 6: The bin edges for the muon kinematic variables [31].

$\cos\theta_\mu$ Bins	T_μ Bins (GeV)
-1.0	-10.0
0.5	0.5
0.68	0.6
0.74	0.7
0.80	0.8
0.85	0.9
0.88	1.0
0.91	1.2
0.94	1.3
0.96	1.4
0.98	1.5
0.99	1.6
1.0	1.7
10	1.8
	1.9
	2.0
	2.1
	2.2
	2.3
	2.4
	2.5
	120

Table 7: The resolution and bias in each of the finer bins from the definition of reconstructed E-Avail chosen

Bin	Resolution	Bias
0.050-0.100	0.0529813	0.0170596
0.100-0.150	0.0550756	-0.00108725
0.150-0.200	0.0579945	-0.0206558
0.200-0.250	0.0650029	-0.03856
0.250-0.300	0.0727235	-0.0562529
0.300-0.350	0.0787157	-0.0790262
0.350-0.400	0.0826325	-0.104594
0.400-0.450	0.0849002	-0.127943
0.450-0.500	0.0887756	-0.150908
0.500-0.550	0.092382	-0.175552
0.550-0.600	0.0982359	-0.197679
0.600-0.650	0.104776	-0.221285
0.650-0.700	0.0845883	-0.243439
0.700-0.750	0.111928	-0.267062
0.750-0.800	0.119501	-0.293028
0.800-0.850	0.140505	-0.340457

Table 8: The number of events, normalized to 14.2238×10^{20} POT, in each E-Avail bin

Bin	Events	Ratio
0-0.100	273830	0.29022781341
0.100-0.200	366547	0.38849700296
0.200.400	278051	0.29470158034
0.400-120	25072.2	0.02657360327

7 Cross-Section Measurement Chain

The probability that a given interaction will occur is dependent on a quantity called the cross-section [2]. The cross-section can be measured based on the number of selected events, the purity, the efficiency, the flux and number of targets.

$$\frac{d^3\sigma}{dT_\mu d\cos\theta_\mu dE_{avail}} = \frac{\Sigma_j U_{ij}(N^{sel}(x_j)P(x_j))}{\epsilon(x_i)\phi(N_{target})(\Delta x_i)} \tag{27}$$

The process for taking sets of Monte-Carlo (MC) simulation to a measured differential cross section is called the Cross-Section Full-Chain. The steps of the Cross-Section Full-Chain are as follows:

- Monte-Carlo Simulation Generation
- Fake Data Generation
- Flux Generation
- Unfolding
- Cross-Section Measurement

7.1 Monte Carlo Simulation Generation

The first step in the Cross-Section Full-Chain is generating Monte-Carlo simulation. The production of the MC is discussed in greater detail in Chapter 4.

Sets of MC simulation are arranged into multiple histograms. These histograms include the selected signal events in both reconstructed and truth variables and the signal efficiency. A matrix is constructed, showing the selected signal events in reconstructed variables on one axis and truth variables on the other axis. This matrix is called the unfolding matrix, otherwise known as a smearing matrix. The binning of these histograms is discussed in Chapter 6. The unfolding matrix can be seen in Figure 56. Each bin on both axes represents a bin in 3D space (those

dimensions being, outgoing muon kinetic energy, cosine of the outgoing muon angle with respect to the beam direction, and E-Avail). This can make visualizing the relationships between the true and reconstructed spaces harder. Histograms of unfolding matrices in one variable each have been included in Figures 57 through 59. However, it is important to state that these have been included for visualization purposes, as these variables are not independent.

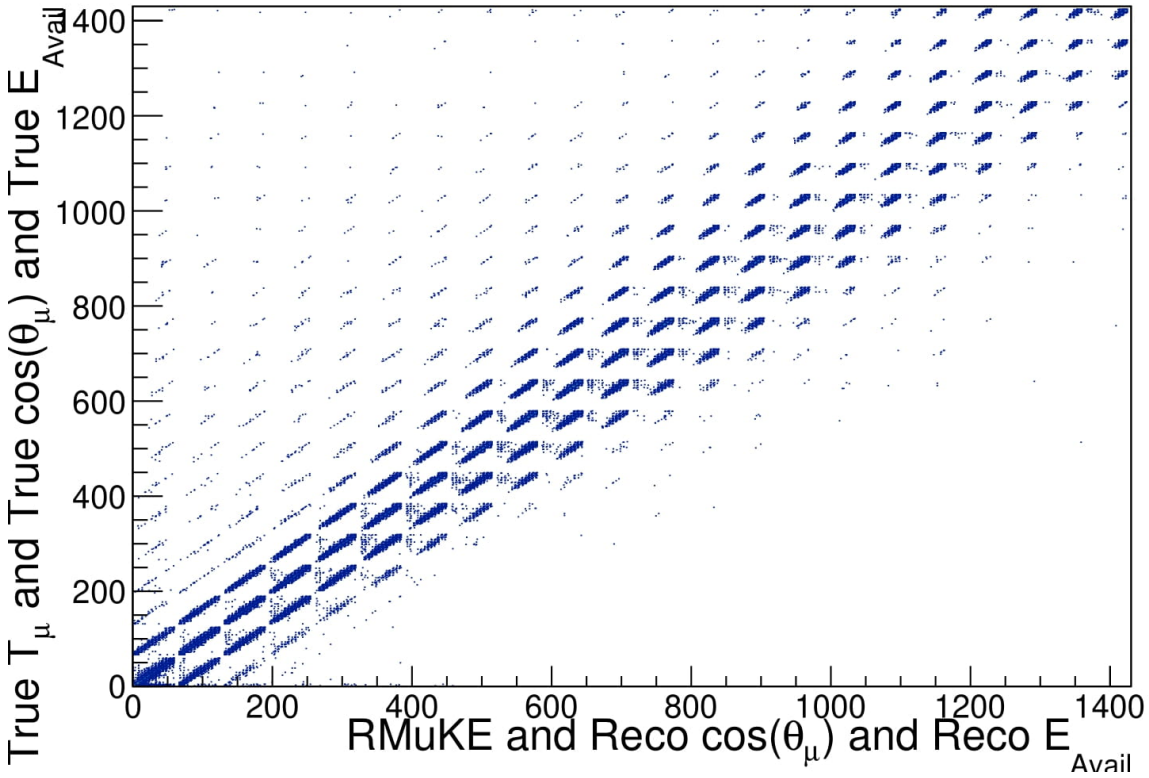

Figure 56: The unfolding matrix for the fake data study, shown as a 2D histogram. Each bin represents a bin in 3D space. The diagonal represents the probability that an event in reconstructed space will remain in the same bin in true space. The off-diagonal bins represent the probabilities that an event will move to another bin during unfolding. Gaps in the diagonal represent bins where there are no events. Due to the 3D nature of the bins, neighboring bins can be far apart in at least one variable.

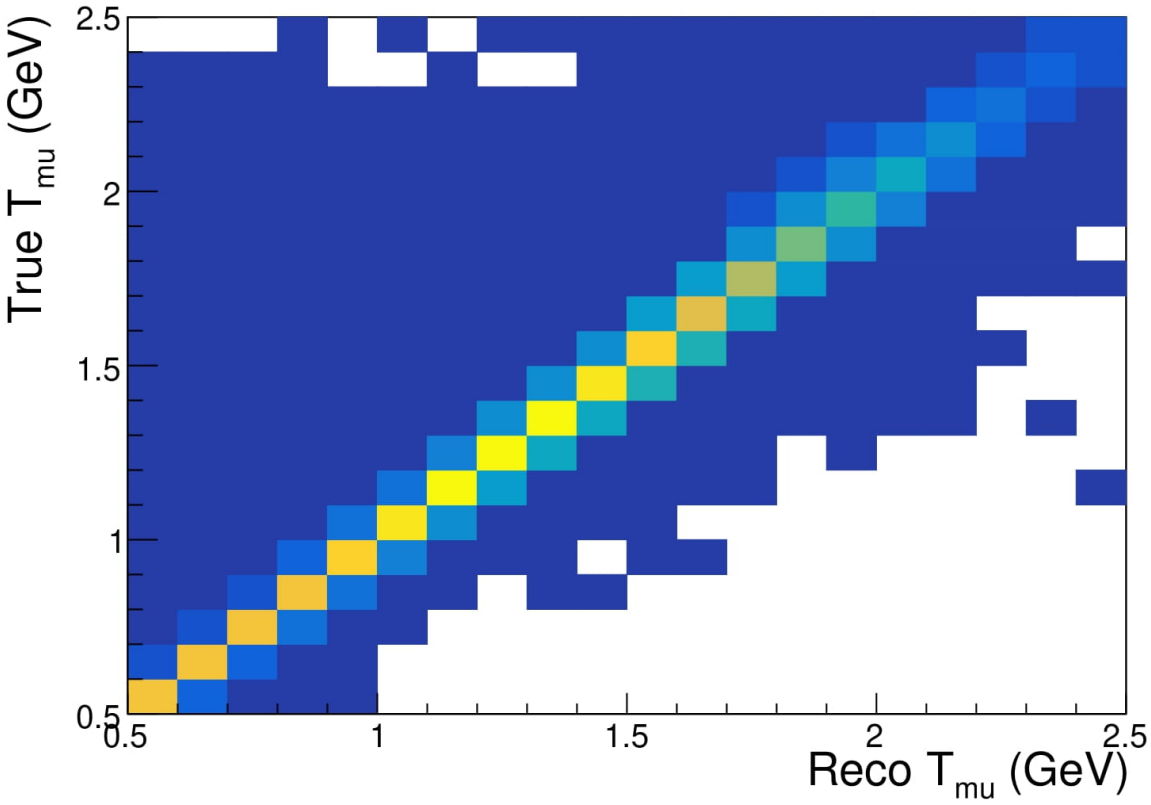

Figure 57: The unfolding matrix for the fake data study, shown as a 2D histogram. Each bin represents a bin in outgoing muon kinetic energy. The diagonal represents the probability that an event in reconstructed space will remain in the same bin in true space. The off-diagonal bins represent the probabilities that an event will move to another bin during unfolding. Outgoing muon kinetic energy is not necessarily independent from the other variables, this histogram is mainly for visualization.

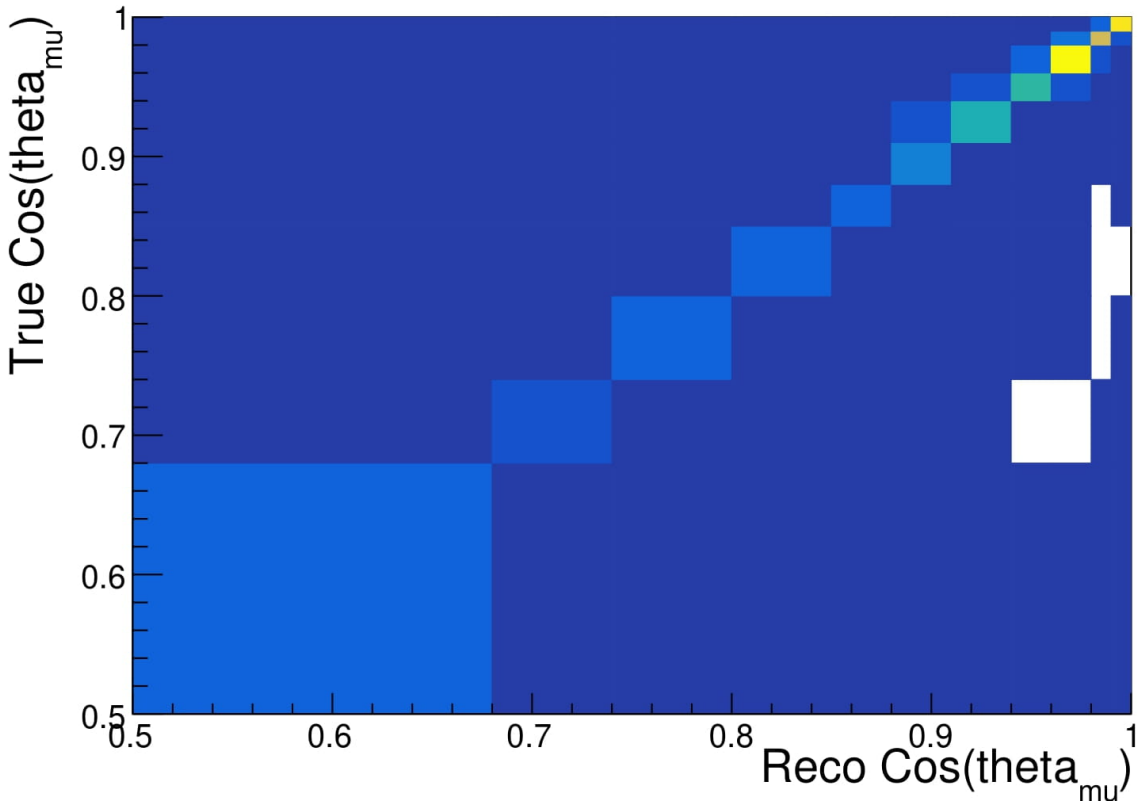

Figure 58: The unfolding matrix for the fake data study, shown as a 2D histogram. Each bin represents a bin in cosine of the angle of the outgoing muon. The diagonal represents the probability that an event in reconstructed space will remain in the same bin in true space. The off-diagonal bins represent the probabilities that an event will move to another bin during unfolding. Cosine of the angle of the outgoing muon is not necessarily independent from the other variables, this histogram is mainly for visualization.

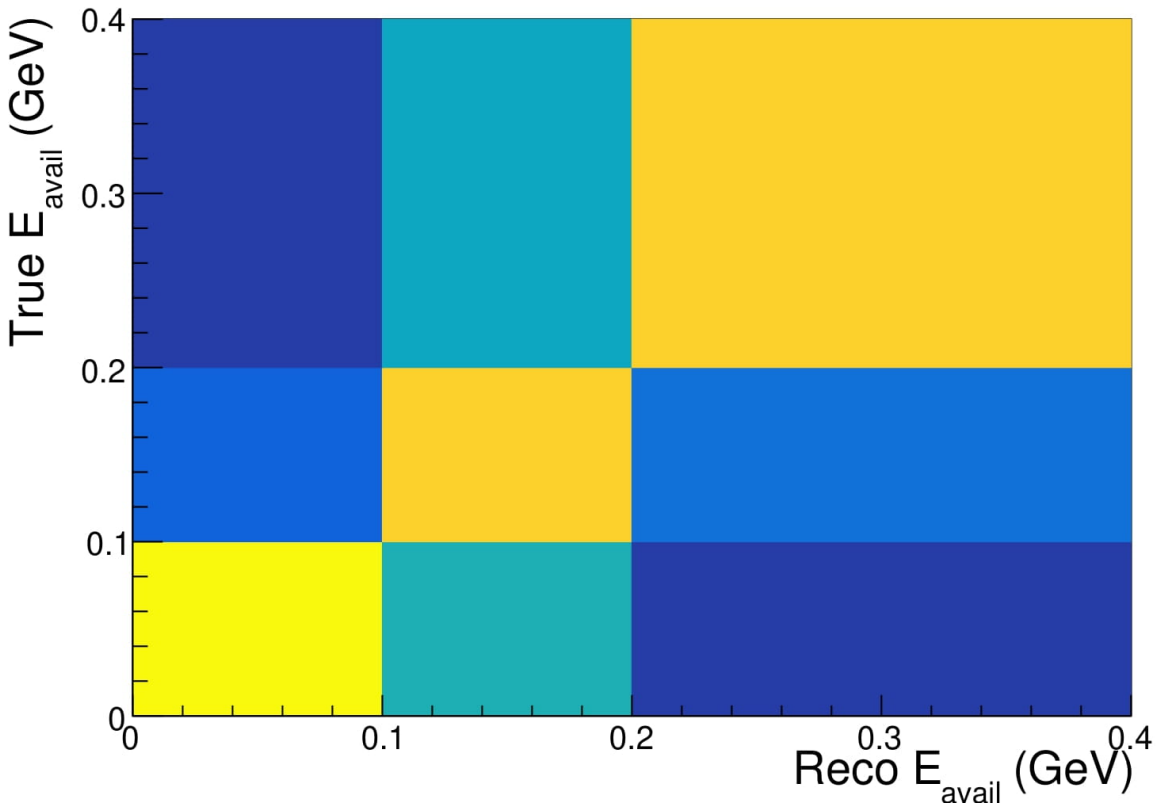

Figure 59: The unfolding matrix for the fake data study, shown as a 2D histogram. Each bin represents a bin in E-Avail. The diagonal represents the probability that an event in reconstructed space will remain in the same bin in true space. The off-diagonal bins represent the probabilities that an event will move to another bin during unfolding. E-Avail is not necessarily independent from the other variables, this histogram is mainly for visualization.

For fake data studies, the total MC simulation set is split into two statistically independent sets. One sample is used as fake data while the other is treated as MC. For the Full-Chain Cross-Section measurement, eighty percent of the total simulation is used for the nominal MC for the central value of the cross-section measurement. When real data is used, one-hundred percent of the total simulation is used for the nominal MC for the cross-section measurement. Eighty percent is used for the nominal MC to minimize statistical uncertainties on the unfolding matrix and signal distributions while leaving enough events for the fake data to have good statistics.

Additional histograms are made for the purity and efficiency as discussed in Chapter 5.

7.2 Fake Data Generation

For fake data studies, twenty percent of the total simulation is used for the fake data for the cross-section measurement. The fake data is stored in histograms of selected events. This step is replaced when working with real data. The fake data selected events can be see in Figure 60.

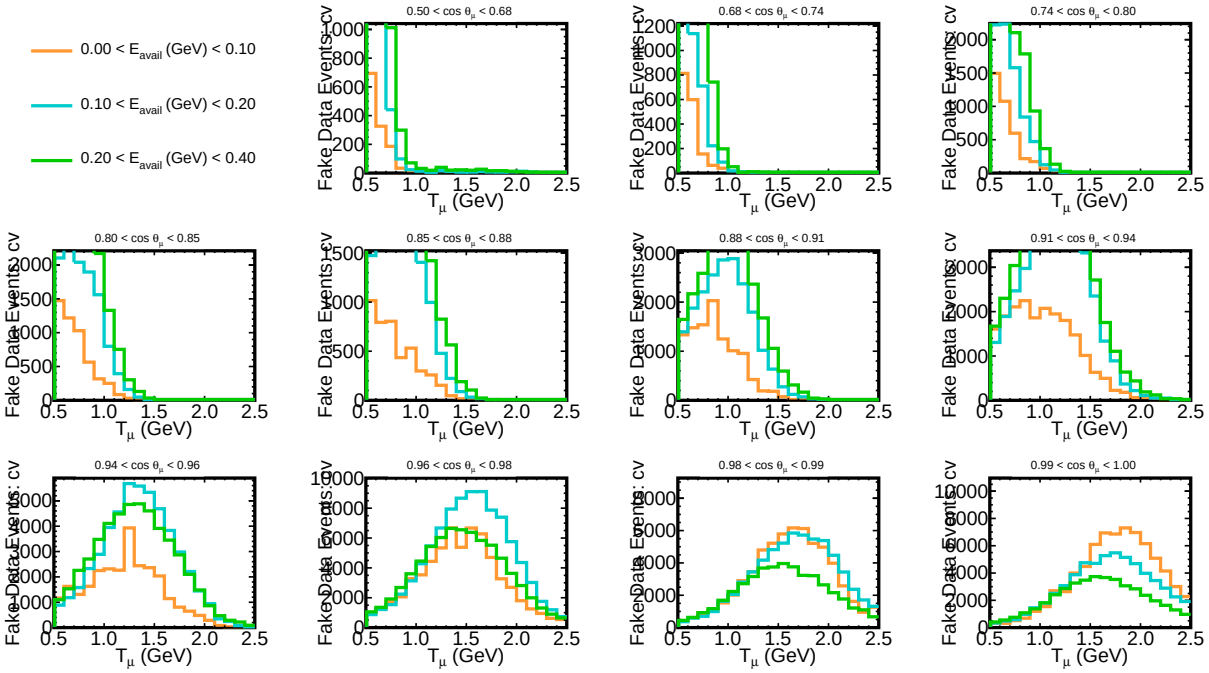

Figure 60: Panel of the selected events of the fake data in reconstructed axes

7.3 Flux Generation

The flux is derived from the number of neutral current (NC) elastic events in the fiducial volume (the number of NC elastic events on hydrogen in a specified area of the ND). The events are simulated using the GENIE simulation package, which includes simulated parameters for the cross-section of the NC elastic interaction. From this cross-section and the number of events in the region, the integrated flux of neutrinos can be derived. The integrated flux derived in this way is $1.6442 \times 10^{13}\text{m}^{-2}$.

7.4 Unfolding

Unfolding is the iterative process of taking a reconstructed distribution and determining the truth distribution it represents.

The selected events in reconstructed variables is multiplied by the purity histogram. The result is an estimation of the distribution of selected signal events in the reconstructed variables. The result can then be fed into the unfolding algorithm. This distribution can be seen in Figure 61.

The unfolding matrix described in a previous section is a map of the MC selected signal events in reconstructed vs truth variables. This map is used to distribute the fake data selected signal events from each bin in the reconstructed axis to bins in the truth axis.

Underflow and overflow bins are necessary for the software to work correctly. Events need to be able to move in and out of bins. For this process to work correctly, underflow and overflow bins are necessary.

After the events are distributed by inverting the unfolding matrix, Bayesian unfolding algorithms[36] are used to ensure that the number of selected signal events remains the same after unfolding. This process is repeated for a second iteration. The data and MC will have different distributions of events in the reconstructed and truth axes. Multiple iterations of the unfolding process are done to get the unfolded events as close to their Truth as possible for an unknown dataset. The optimization process that lead to this analysis doing exactly two iterations of unfolding is given in Chapter 9. The unfolded distribution can be seen in Figure 62.

Tests to show the validity of the unfolding can be seen in Chapter 8.

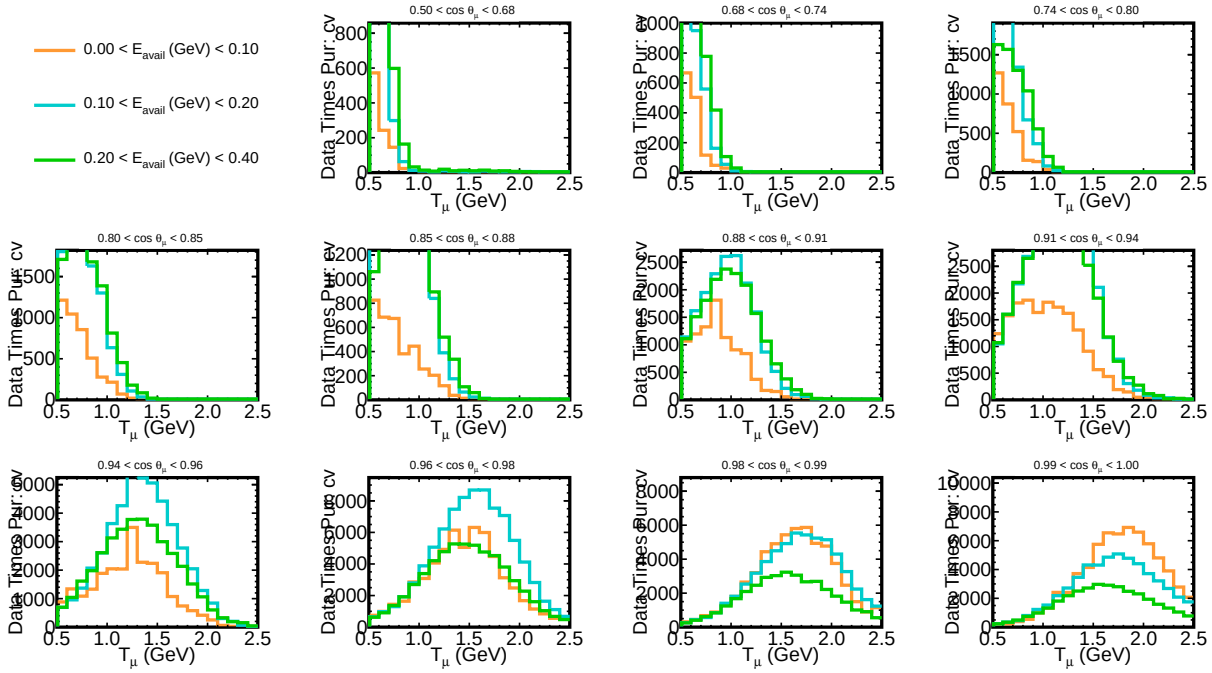

Figure 61: Panel of the selected events of the fake data in reconstructed axes times the purity

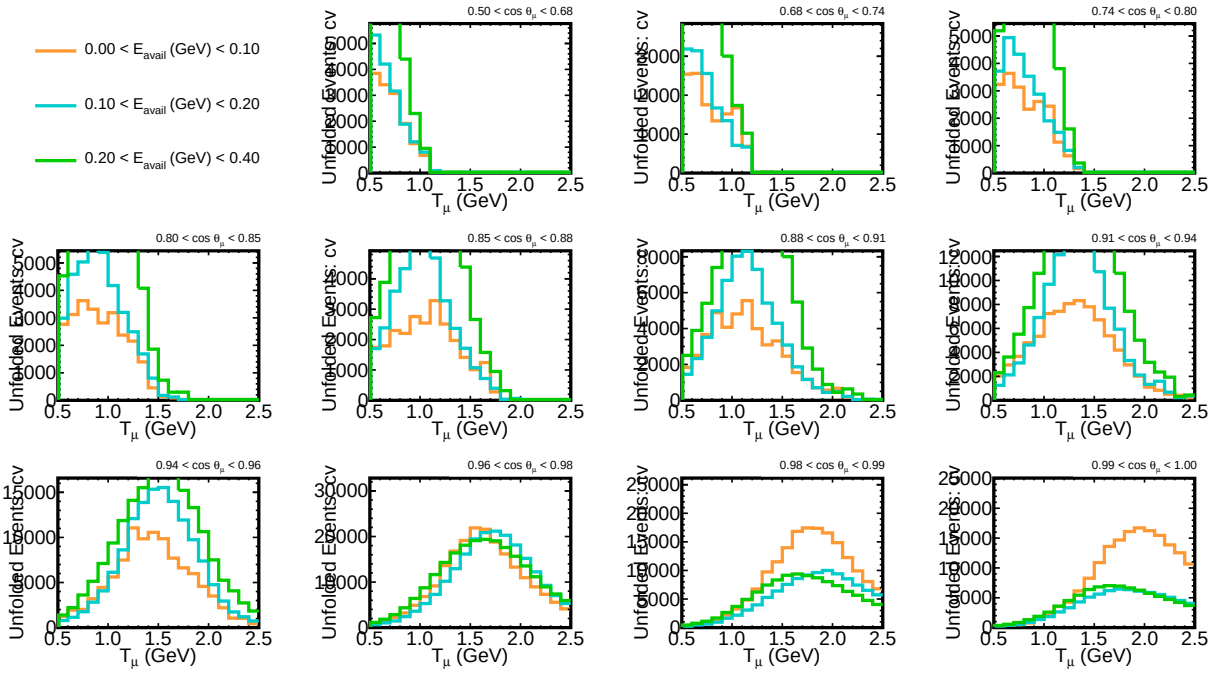

Figure 62: Panel of the unfolded selected signal events in bins of true muon kinetic energy, true cosine of the angle of the muon, and true E-Avail. Two iterations of unfolding are done to get this result.

7.5 Cross-Section Measurement

The cross-section measurement is dependent on the number of selected events, the purity, efficiency, the flux and number of targets.

$$\frac{d^3\sigma}{dT_\mu d\cos\theta_\mu dE_{avail}} = \frac{\Sigma_j U_{ij}(N^{sel}(x_j)P(x_j))}{\epsilon(x_i)\phi(N_{target})(\Delta x_i)} \tag{28}$$

The output of the unfolding step, the estimated number of selected signal events in each of the true variables, is divided by the efficiency, the number of targets and the flux. Each bin is divided by the volume of the bin. The result is the triple differential Cross-Section, as can be seen in Figure 63 for a fake data sample. The same procedure performed on real NOνA data would yield the measured cross-section.

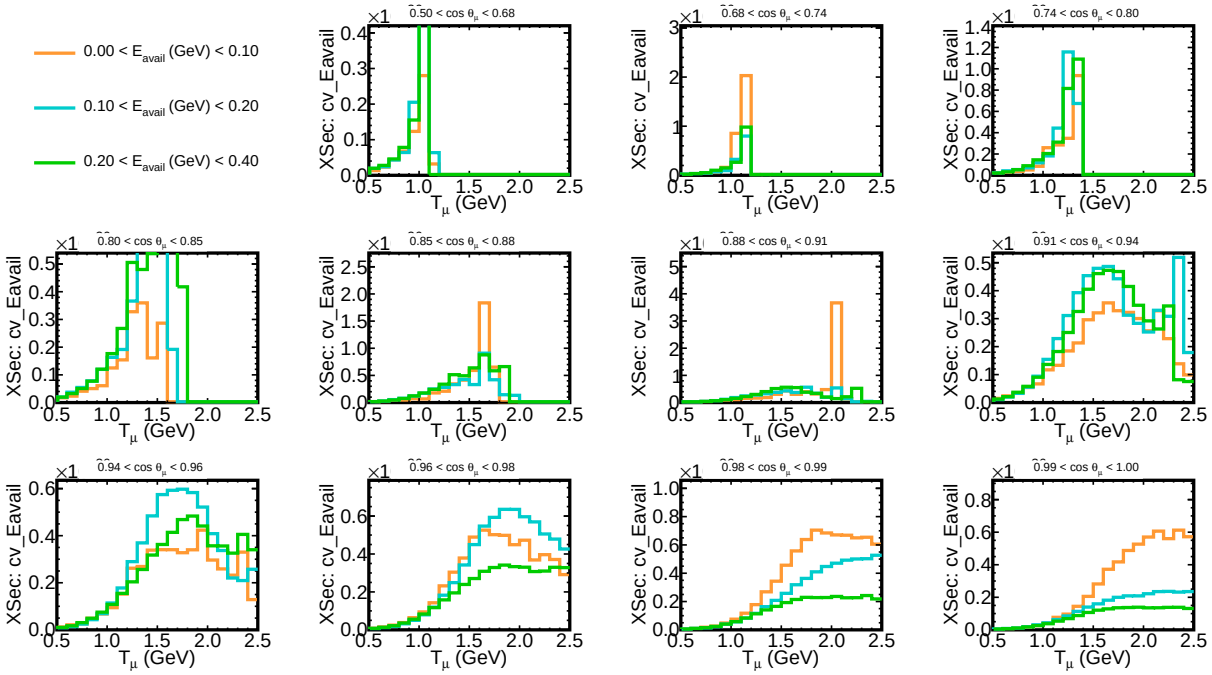

Figure 63: Example of a measured triple differential cross section in bins of true muon kinetic energy, True cosine of the angle of the muon, and true E-Avail using fake data

8 Unfolding Testing

To make sure that the unfolding is done correctly, a test is done to make sure that the unfolded distributions matches the underlying truth. This test is called a closure test. It involves unfolding selected signal events against an unfolding matrix made from Selected Signal events, to ensure that the output matches the input.

8.1 In-Out Test

The trivial case is tested first. The process of unfolding laid out in the chapter 7 is used here with a few alterations. The full MC set is used for both the fake data and MC histograms. One unfolding iteration is done.

After the histogram for the unfolded events events in truth variables is divided by the True selected signal events histogram. The ratio should be exactly one in all bins. Events are allowed to flow in and out of bins just like the during the Full-Chain unfolding, however the migration will be perfect because the migration map used will be the "correct" one.

The results of the test can be seen in figures 64-66. The ratio is one in all bins, meaning the trivial case works as intended.

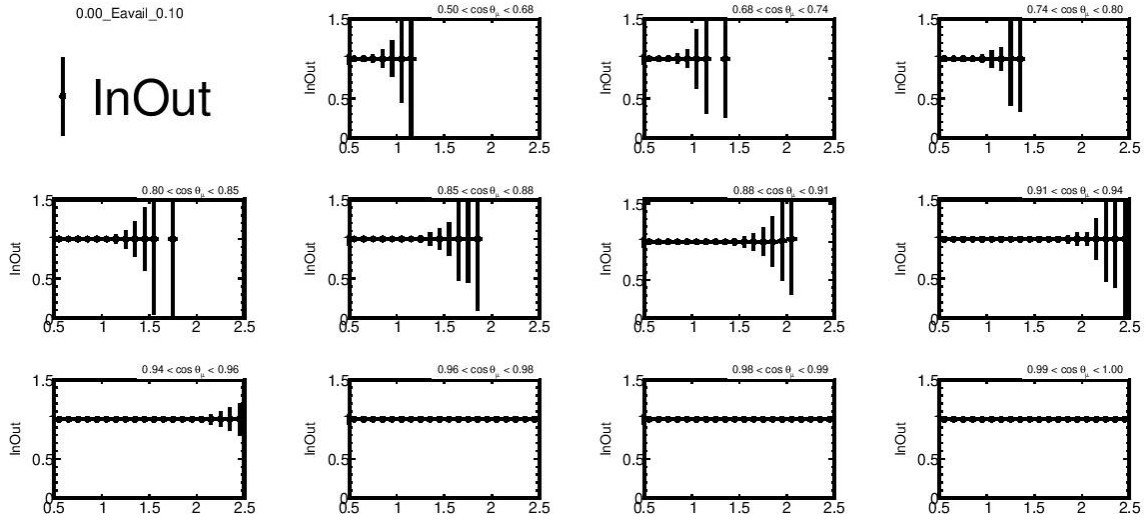

Figure 64: Panel of the trivial case representing the 0 < E-Avail < 100 MeV bin. Ratio of the measured cross-section to the true cross-section. Full MC used for both fake data and MC.

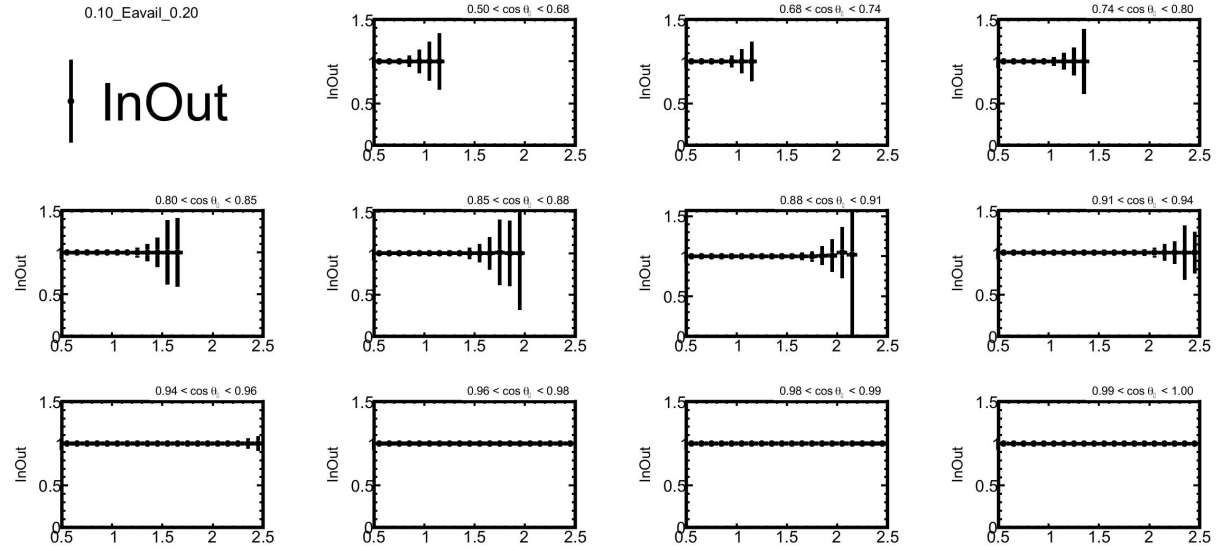

Figure 65: Panel of the trivial case representing the 100 < E-Avail < 200 MeV bin. Ratio of the measured cross-section to the true cross-section. Full MC used for both fake data and MC.

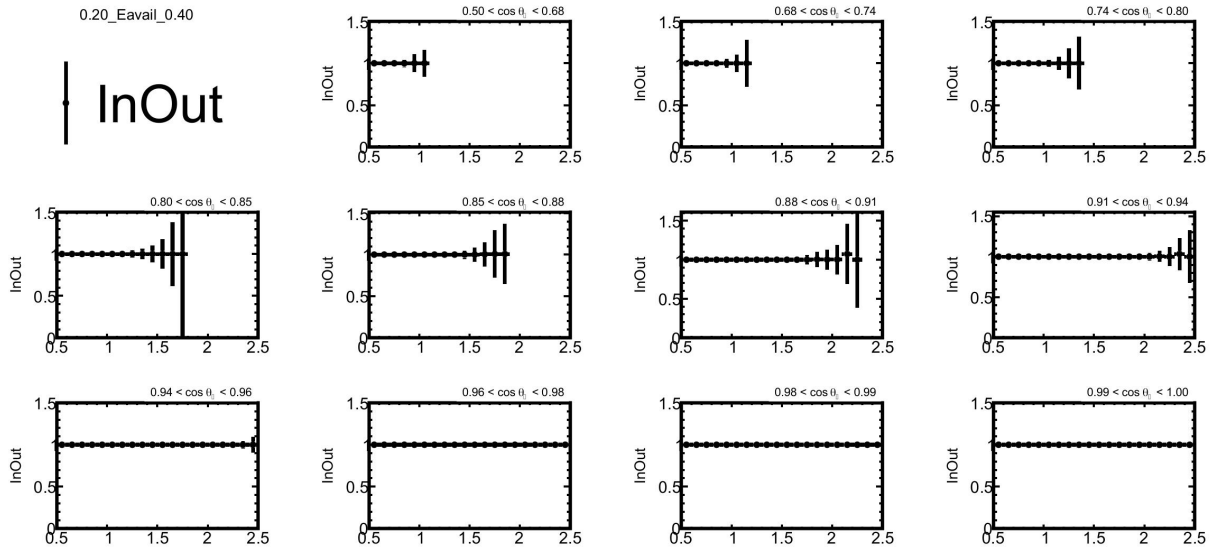

Figure 66: Panel of the trivial case representing the 200 < E-Avail < 400 MeV bin. Ratio of the measured cross-section to the true cross-section. Full MC used for both fake data and MC.

8.2 Closure Test

The closure test takes the full MC set and breaks it into two statistically independent samples of equal size. Sample 1 is used as fake data for the purposes of unfolding. Sample 2 is used as the MC for both unfolding and to compare the unfolded events against. The process for unfolding laid out in the previous chapter is repeated with two changes. Only one unfolding iteration is done, and the selected signal events are used for the fake data histograms.

After the histogram for the unfolded events events in truth variables is divided by the true selected signal events histogram. The two samples are statistically independent samples, and the ratio should be one for all bins within statistical uncertainty. As shown in figures 67 - 69, this did not bear out. A series of tests on this mismatch was carried out, and is described in the next section.

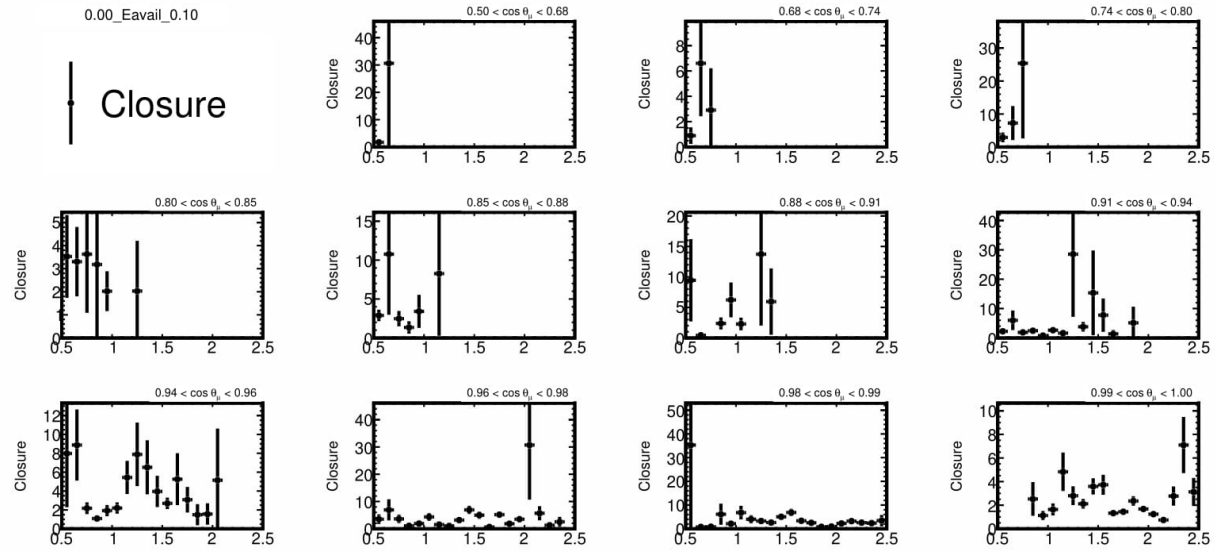

Figure 67: Panel of the closure test representing the 0 < E-Avail < 100 MeV bin. Ratio of the measured cross-section to the true cross-section. Two statistically independent samples of the total MC are used for the fake data and MC.

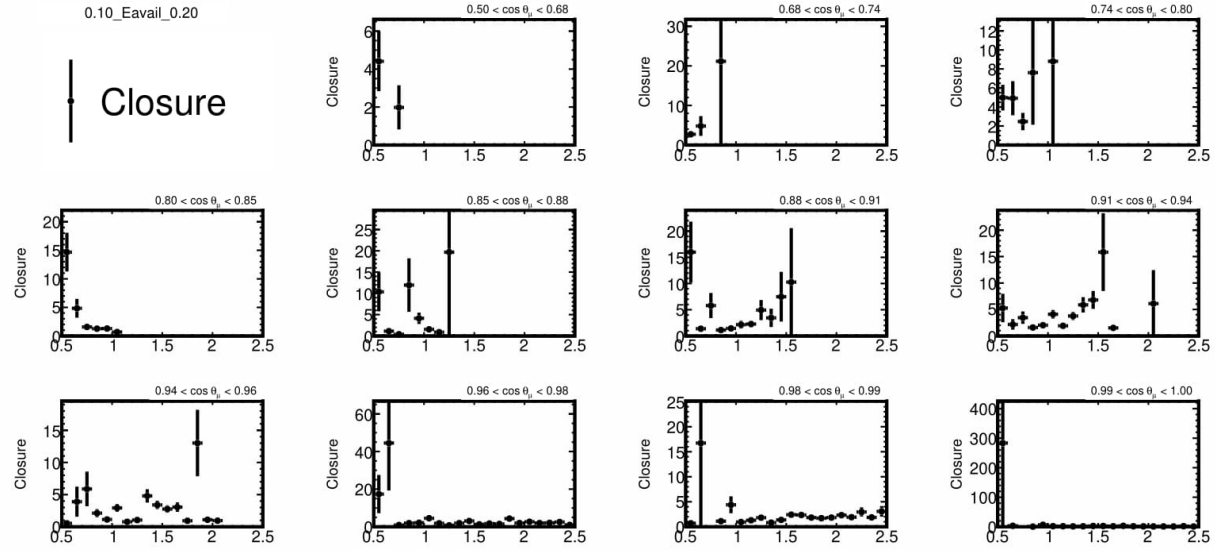

Figure 68: Panel of the closure test representing the 100 < E-Avail < 200 MeV bin. Ratio of the measured cross-section to the true cross-section. Two statistically independent samples of the total MC are used for the fake data and MC.

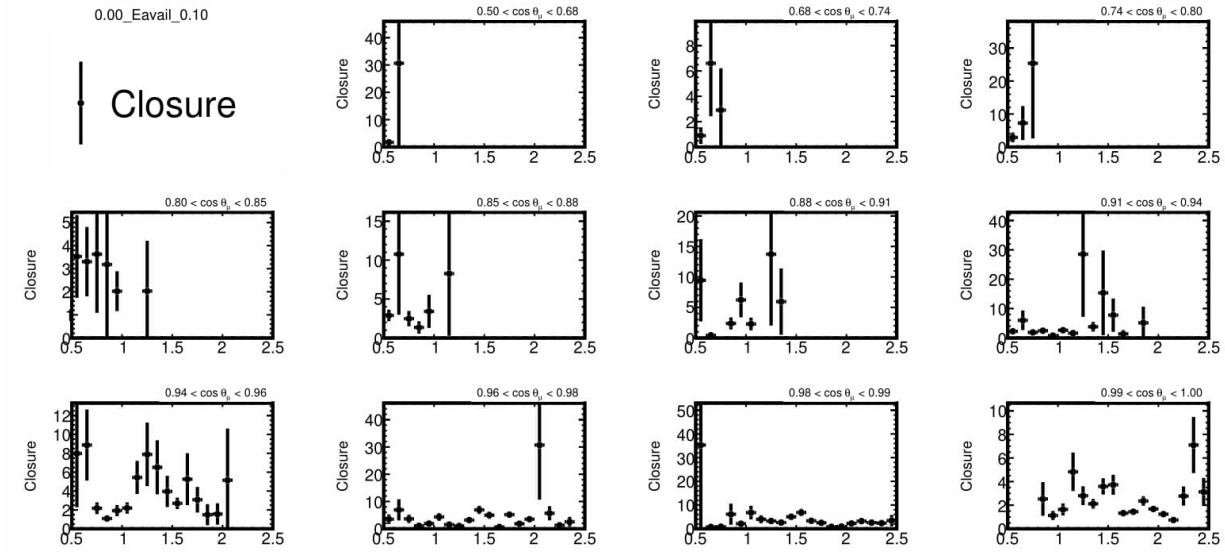

Figure 69: Panel of the closure test representing the 200 < E-Avail < 400 MeV bin. Ratio of the measured cross-section to the true cross-section. Two statistically independent samples of the total MC are used for the fake data and MC.

8.3 Mismatch Testing

As shown in Figures 67, 68, and 69, there is a mismatch between the unfolded fake data and the true selected signal events in the closure test. In order to isolate the source of this mismatch, a series of tests was done. The tests involve turning off individual elements of the analysis and re-running the closure test to see if the mismatch was removed.

The various cuts were turned on and off to see if there was an issue with the choice of cuts. The mismatch did not disappear, which lead to the conclusion that the issue was not with the cuts.

The weights were then turned off to see if there was a problem in the weights. The mismatch disappeared (that is, all ratios were one within statistical uncertainties), leading to the conclusion that there was an issue in the weights. This can be seen in figure 70.

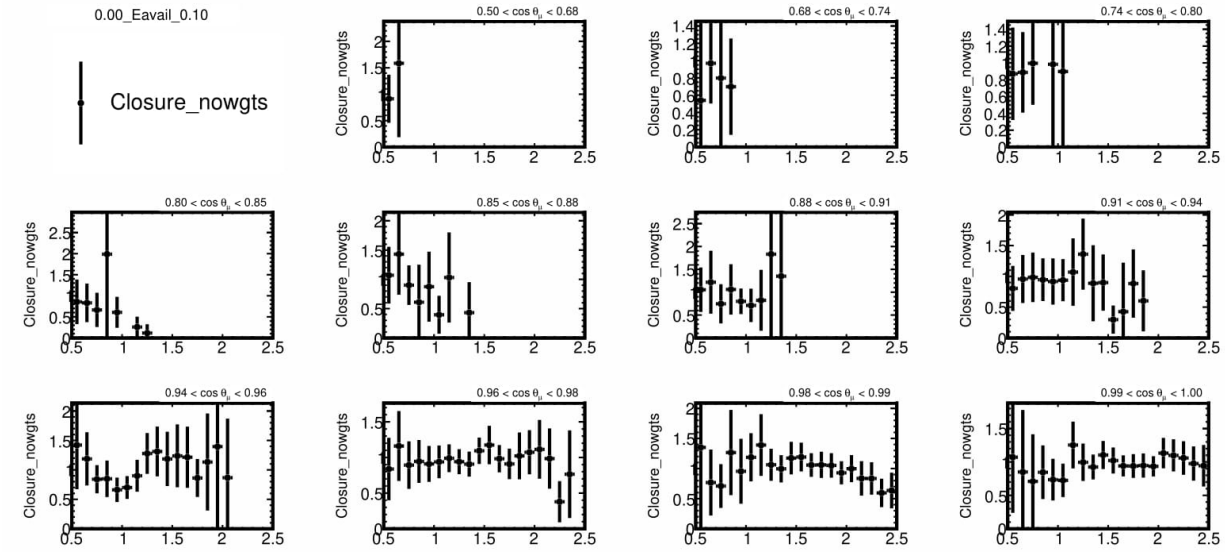

Figure 70: Panel of the closure test with weights turned off representing the 0 < E-Avail < 100 MeV bin. Ratio of the measured cross-section to the true cross-section. Two statistically independent samples of the total MC are used for the fake data and MC.

The selected signal events were separated by interaction mode with the weights kept on. The mismatch disappeared in the quasi-elastic events but remained in the MEC events. The closure test with the MEC events removed can be seen in Figure 71.

The ultimate conclusion was that the MEC weights were causing an issue. Figure 17 in Chapter 4 shows the distribution of weights and the events that were used to determine the weights. This analysis is sensitive to the region where the weights are highest and the the statistics of that sample were low.

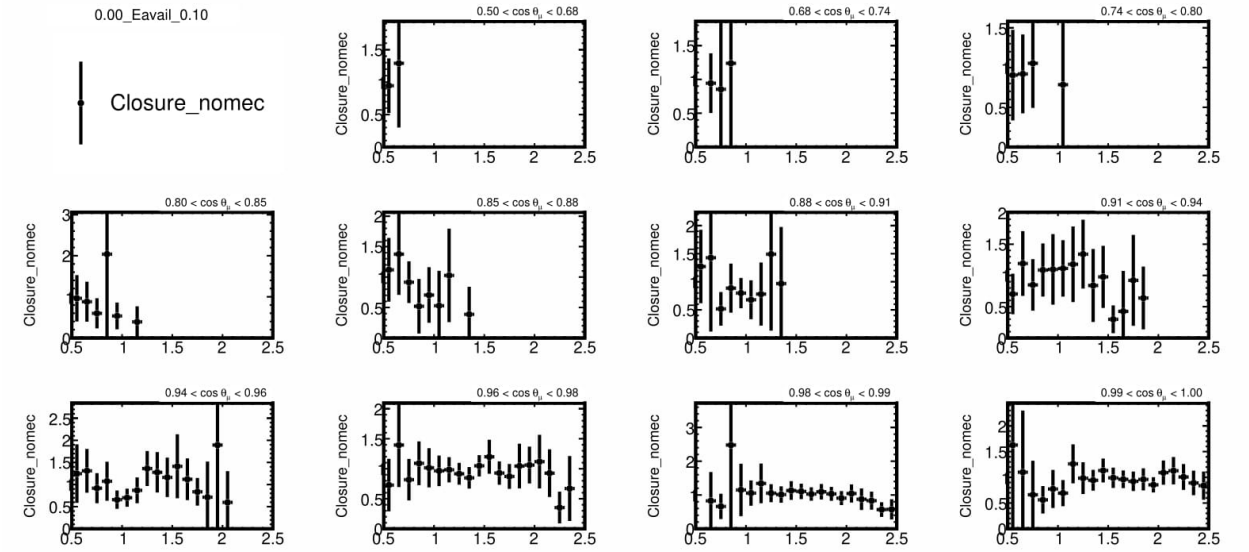

Figure 71: Panel of the closure test with MEC events removed, representing the 0 < E-Avail < 100 MeV bin. Ratio of the measured cross-section to the true cross-section. Two statistically independent samples of the total MC are used for the fake data and MC.

8.4 MEC Weight

Because the source of the mismatch is the MEC weights being very large in som cases, a new weight was created with a condition that capped the MEC Weight at 50.0. The closure test was repeated with these capped MEC weights and the results can be seen in Figures 72 through 74. The ratio was one within one or two standard deviations for all bins.

The compromise made here is that there will be bins that have a weight smaller than needed to provide consistency between NOνA's MEC model and data. The effect of this compromise will be shown in the chapter on systematic uncertainties. Fixing this issue is beyond the time frame available for this thesis result. Therefore, a systematic uncertainty related to this issue will be assigned, described in Chapter 10.

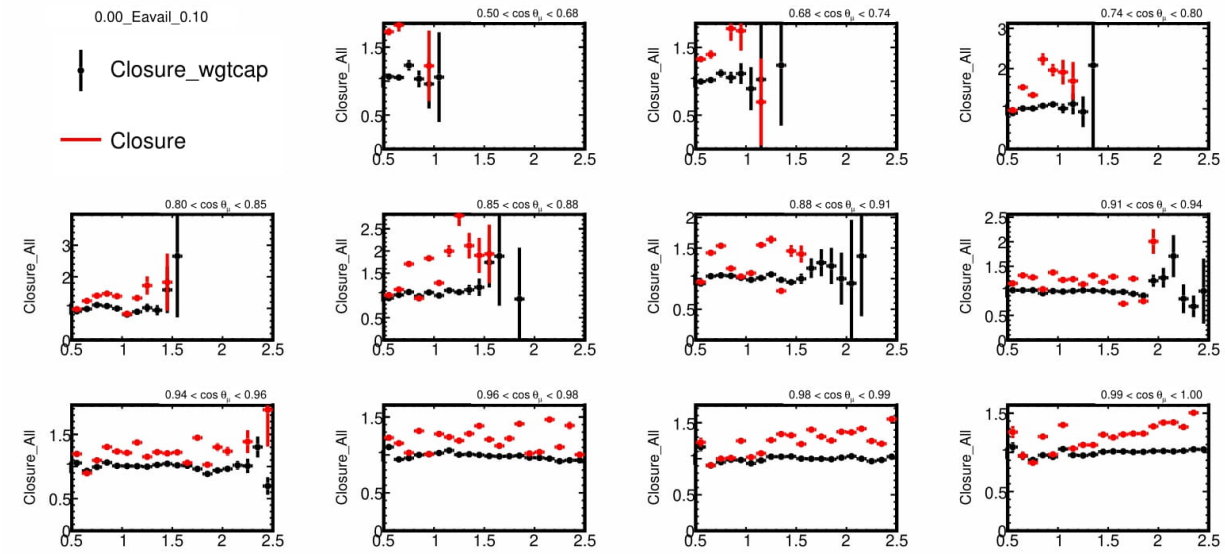

Figure 72: Panel of the closure test with MEC weights capped, compared to the uncapped closure test, representing the 0 < E-Avail < 100 MeV bin. Ratio of the measured cross-section to the true cross-section. Two statistically independent samples of the total MC are used for the fake data and MC.

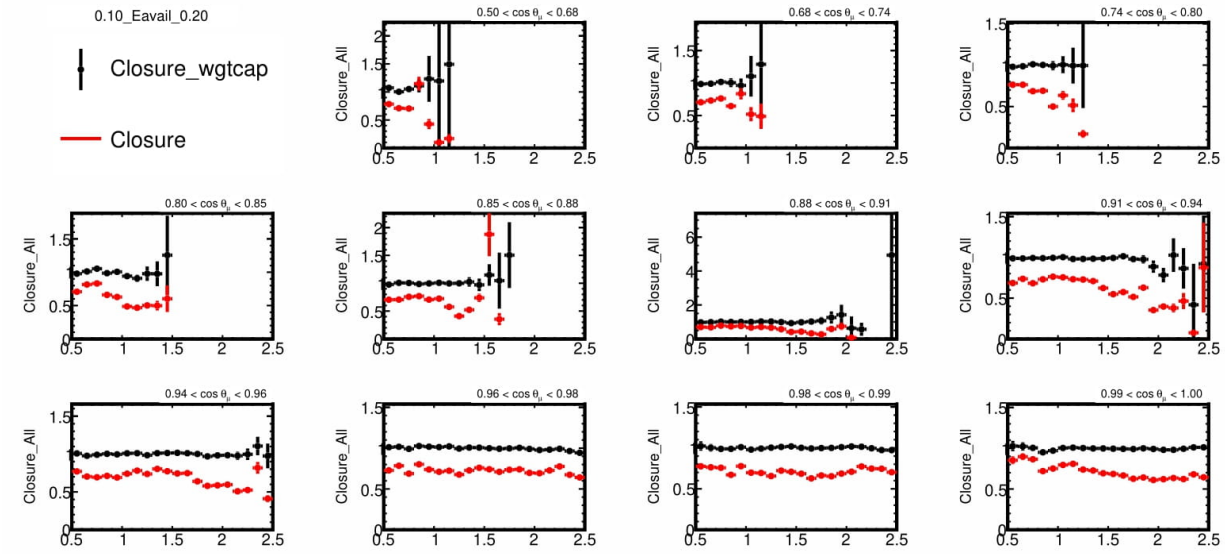

Figure 73: Panel of the closure test with MEC weights capped, compared to the uncapped closure test, representing the 100 < E-Avail < 200 MeV bin. Ratio of the measured cross-section to the true cross-section. Two statistically independent samples of the total MC are used for the fake data and MC.

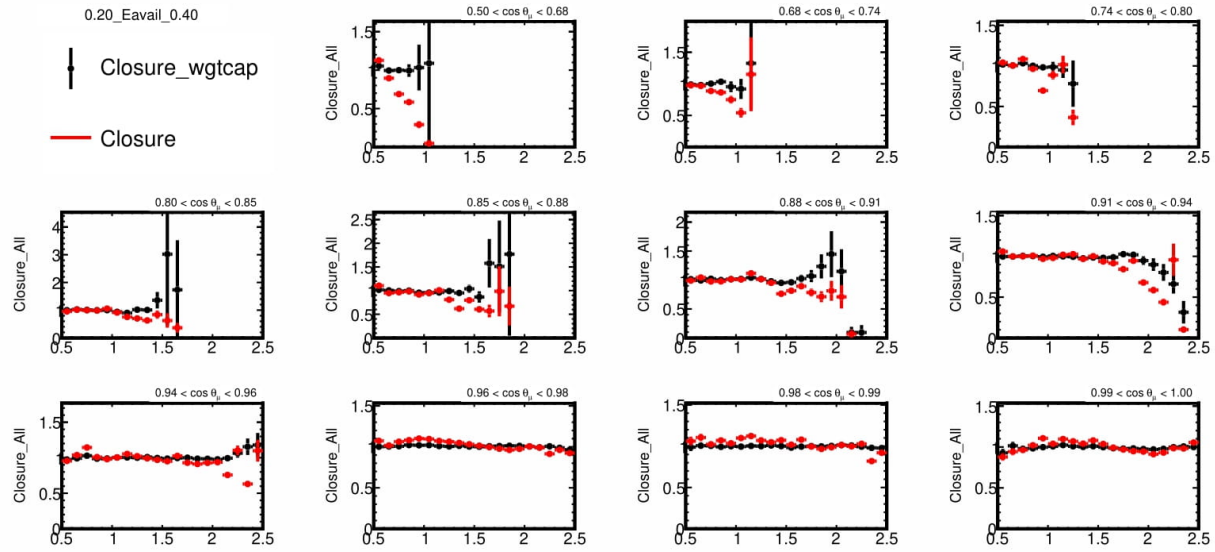

Figure 74: Panel of the closure test with MEC weights capped, compared to the uncapped closure test, representing the 200 < E-Avail < 400 MeV bin. Ratio of the measured cross-section to the true cross-section. Two statistically independent samples of the total MC are used for the fake data and MC.

9 Unfolding Optimization

The goal of unfolding is to match reconstructed distributions to their underlying truth. Unfolding is an iterative process, and the number of iterations has an impact on how well the two distributions match. Therefore, there is a need to determine the optimal number of iterations to use. The steps in this procedure are listed here and described below.

- Generate 500 GENIE universes from pseudo-data
- Unfold 500 pseudo-data distributions using unshifted MC distribution
- Calculate the bias and error for each universe for each number of iterations
- Average combined bias and error over the 500 universes
- Choose number of iterations will the lowest combined error and bias.

The metric chosen for this analysis is the sum of the error and the bias. The number of iterations that minimizes this sum is chosen as the optimal number of iterations. These metrics are chosen because they are what gets changed by unfolding the reconstructed distributions. The average of the sum will be called $\overline{C}$ and is given in the equation that follows.

$$\overline{C} = \frac{1}{M}\sum_{i=1}^{M}\sum_{j=1}^{Bins}\frac{(\sigma_{Unfold_{M,i,j}})^2 + (Unfold_{M,i,j} - True_{M,i,j})^2}{True^2_{M,i,j}} \tag{29}$$

The first term is the statistical error produced by the iterative unfolding algorithm squared. The second term is the bias. Bias is the measure of the difference between the unfolded reconstructed distribution and the true distribution. The closer this term is to zero, the more similar the two distributions are in each bin. It is weighted by the total truth value for each bin, and averaged over the total number of universes generated for this study.

For this study, the nominal MC is split into two evenly distributed statistically independent datasets. Fifty percent is used as pseudo-data, the other fifty percent is used as MC. The Unfolding

process outlined in Chapter 7 is largely followed, however a number of universes must be generated first.

Five hundred universes are generated from the pseudo-data sample. GENIE systematics were used to shift the sample, which will be described in greater detail in Chapter 10. The selected signal events of each universe are saved in both reconstructed and true axes. The events in the reconstructed axes represent the data for that universe, while the events in the truth axes represent the underlying truth of that universe.

The unshifted central MC is used to make the unfolding matrix. The goal of this study is to find the optimal number of iterations to use for an unknown data set (the 500 sets of randomly shifted pseudo-data) with the central MC.

Before any unfolding is done, a measurement of combined error and bias is done for each universe. The error in the pre-unfolded distribution is the statistical uncertainty, equal to the square root of the number of events in each bin of the distribution.

For each universe, the pseudo-data is fed into the unfolding algorithm using the same unshifted central MC as the truth information. It is first unfolded a single iteration. Once it has been unfolded, the error in each bin and the number of events in each bin are recorded. These are then compared with the truth of that universe to find the combined error and bias of that universe for the one unfolding iteration.

The resulting distribution is unfolded again for another iteration and the process repeated until four iterations had been completed. This process is computationally taxing, so a maximum of four iterations was chosen.

For each universe, the combined error and bias measured is summed over all the bins. The result of this for a randomly chosen universe can be in Figure 75.

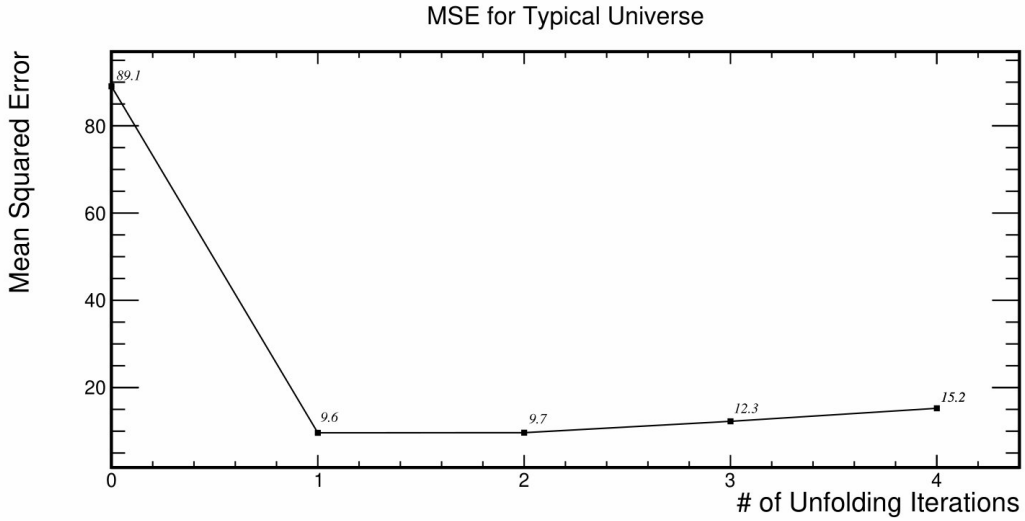

Figure 75: The weighted combined error and bias of a single universe compared to the number of unfolding iterations.

Finally, the combined error and bias for each iteration is averaged over all 500 universes. The result can be seen in Figure 76.

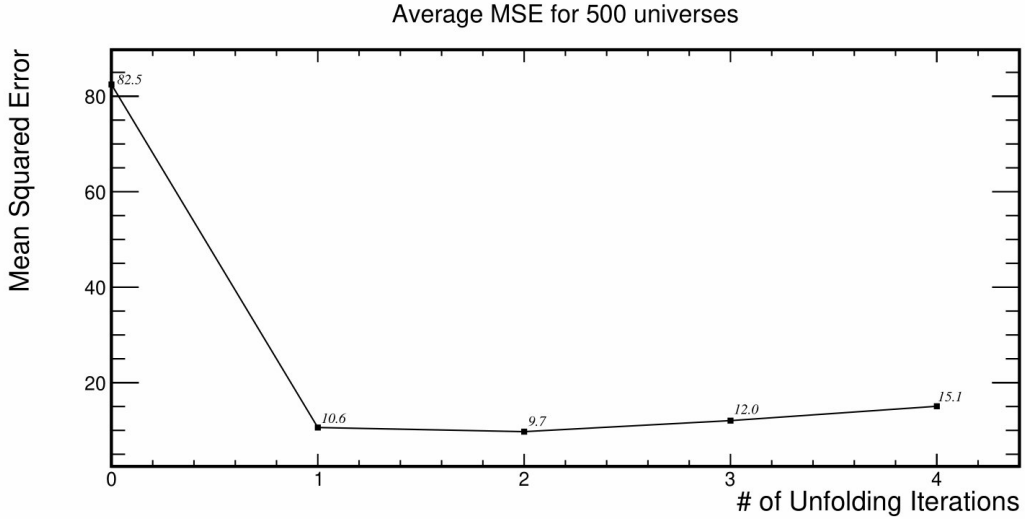

Figure 76: The average combined error and bias of 500 universes versus number of unfolding iterations. The minima is found at two unfolding iterations.

$\overline{C}$ is the lowest when there are two Unfolding iterations. Therefore, the optimal number of unfolding iterations is two iterations.

10 Cross-Section Uncertainty

There are a number of sources of uncertainty in this measurement. The sources of systematic uncertainty that have been modeled are grouped into the following designations:

- Detector Systematics
- Muon Kinematic Systematics
- Beam Systematics
- GENIE Systematics
- PPFX Systematics
- MEC Model Systematic
- MEC Weight
- Neutron

Simulated samples are produced in which models have been shifted or adjusted to account for each systematic uncertainty. The process outlined in Chapter 7 is repeated for each source of systematic uncertainty. The same fake data is compared against shifted truth samples. In this way, the fake data is fit to a truth sample which has a different underlying model, and the effect this has on the measured cross-section can be evaluated. The difference between the measured cross-section with the nominal model and with each shifted model is considered a systematic uncertainty on the measured cross-section. The cross-section uncertainty modeling is done to ensure that the there is sufficient coverage that the real underlying cross-section is covered by the cross-section measured from the data and the uncertainty. After the cross-sections are measured for the shifted samples, bin to bin covariance matrices are calculated for the different systematics.

In addition to the systematic uncertainty, statistical uncertainty is also taken into account.

10.1 Detector Systematics

The detector-related systematic uncertainties are related to modeling the light output due to scintillation and other effects in the detector. The list of systematics that fall under this category are:

- Calibration Up/Down
- Calibration Shape
- Cherenkov Up/Down
- Light Level Up/Down
- Aging

The calibration systematic is made by changing the parameter of the absolute calibration, as discussed in Chapter 4. NOνA uses a five percent uncertainty in the absolute calibration parameter [22]. Two separate shifts are made, one measuring the cross-section with a five percent increase in the energy deposited and the other measuring the cross-section with a five percent decrease in the energy deposited. The covariance matrices are calculated for both cases, and then averaged together. The fractional uncertainty is then the average. A similar process is used for all two-sided systematics (systematics where a parameter is tuned up or down). The calibration systematic can be seen in Figure 77.

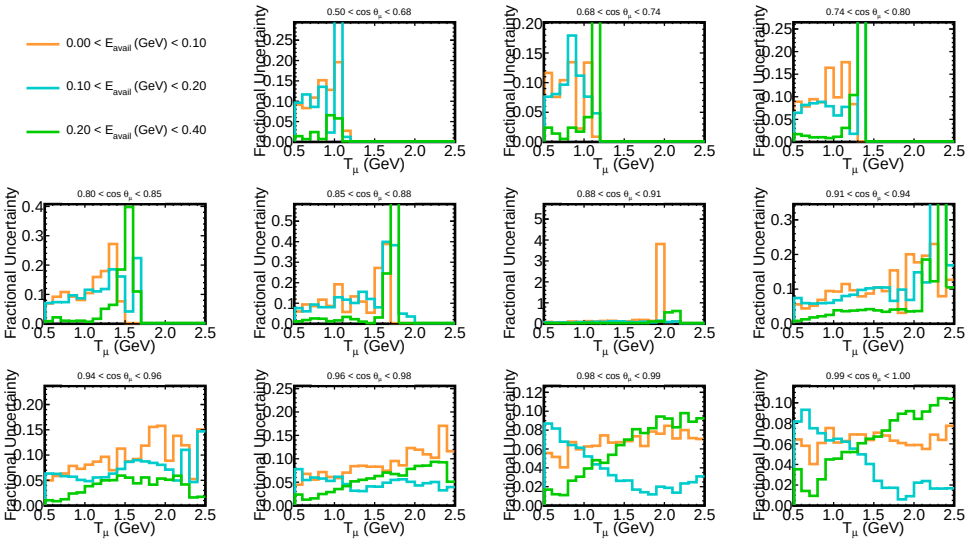

Figure 77: The fractional uncertainty between the central value cross-section and the shifted samples made from adjusting the absolute calibration parameters by ±5%. This uncertainty uses the combined covariance matrix for both the positive and negative shifts.

The calibration shape systematic comes from uncertainty introduced from the relative calibration. Relative calibration, as discussed in Chapter 4, accounts for differences in energy reported based on the location of the hit in the cell. However, the calibration procedure breaks down at the edges of the cells. An uncertainty was introduced based on data/MC differences, parameterized with a linear shape, with different slopes for the edges vs the middle [22]. The calibration shape systematic can be seen in Figure 78.

The light level systematic is a two-sided systematic that increases/decreases the number of photons measured in each view by ±5% [22]. The light level systematic can be seen in Figure 79.

The Cherenkov systematic is a two-sided systematic that increases/decreases the amount of Cherenkov radiation measured by ±6.2% [22]. The Cherenkov systematic can be seen in Figure 80.

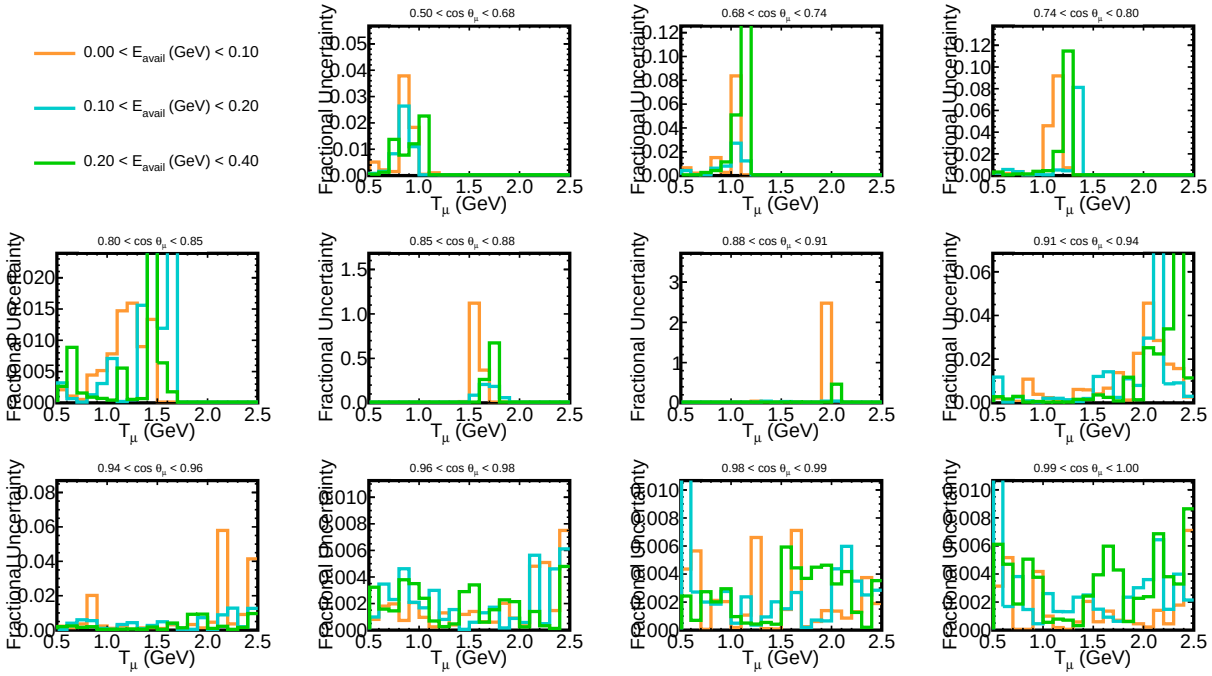

Figure 78: The fractional uncertainty between the central value cross-section and the shifted sample made by taking into account uncertainties introduced from the relative calibration.

The detector aging systematic assumes that there is a linear drift downwards in light level over time due to degradation of the scintillator and/or fibers and adds a corresponding upward drift overall calibration scale to compensate [22]. This is meant to counteract the increasing number of hits that will fall below threshold over time [22]. The detector aging systematic can be seen in Figure 81.

Systematic shifts are applied to the full MC dataset. The twenty percent definition is used for the fake data definition. The total uncertainty that comes from uncertainties from the detector can be seen in 82. Each source plotted together can be seen in Figures 83, 84 and 85.

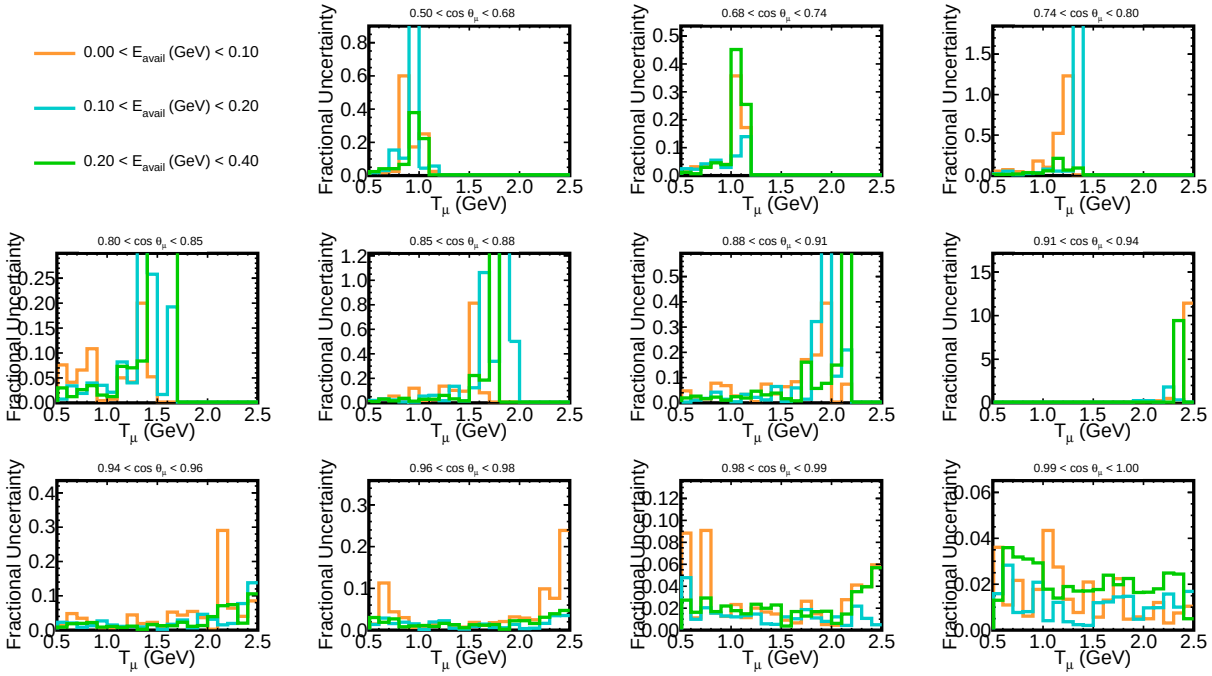

Figure 79: The fractional uncertainty between the central value cross-section and the shifted samples made from adjusting the number of photons measured in each view ±5%. This uncertainty takes uses the combined covariance matrix for both the positive and negative shifts.

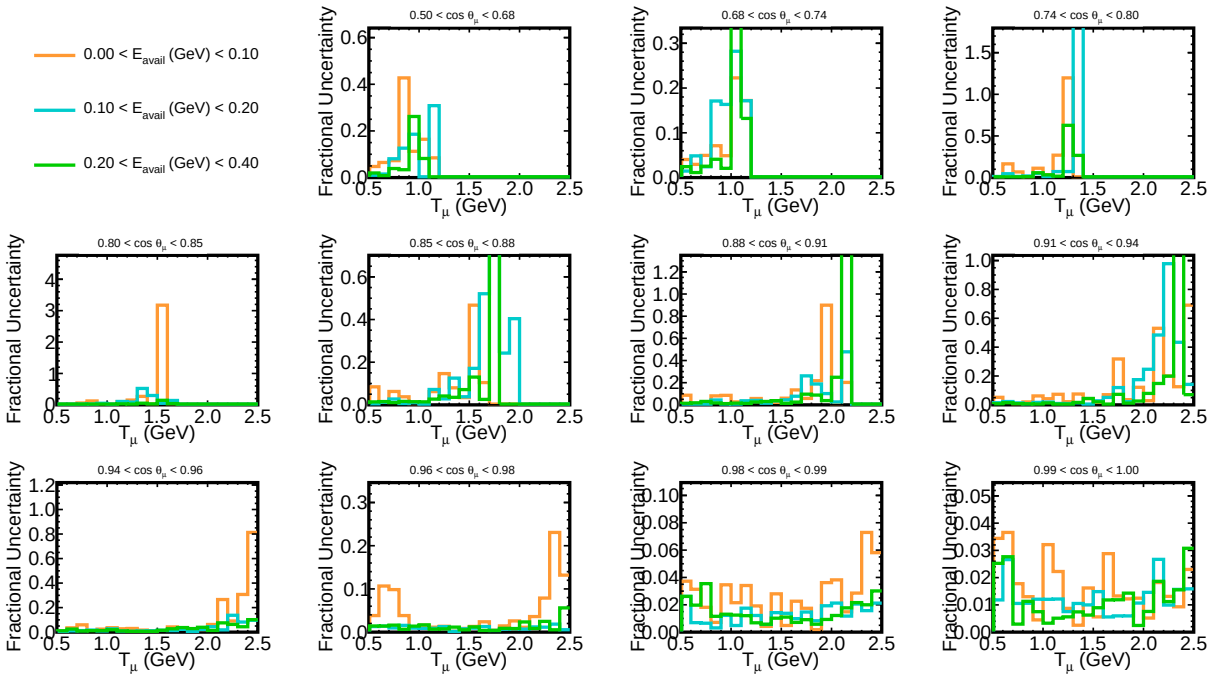

Figure 80: The fractional uncertainty between the central value cross-section and the shifted samples made from adjusting the amount of Cherenkov radiation measured by ±6.2%. This uncertainty uses the combined covariance matrix for both the positive and negative shifts.

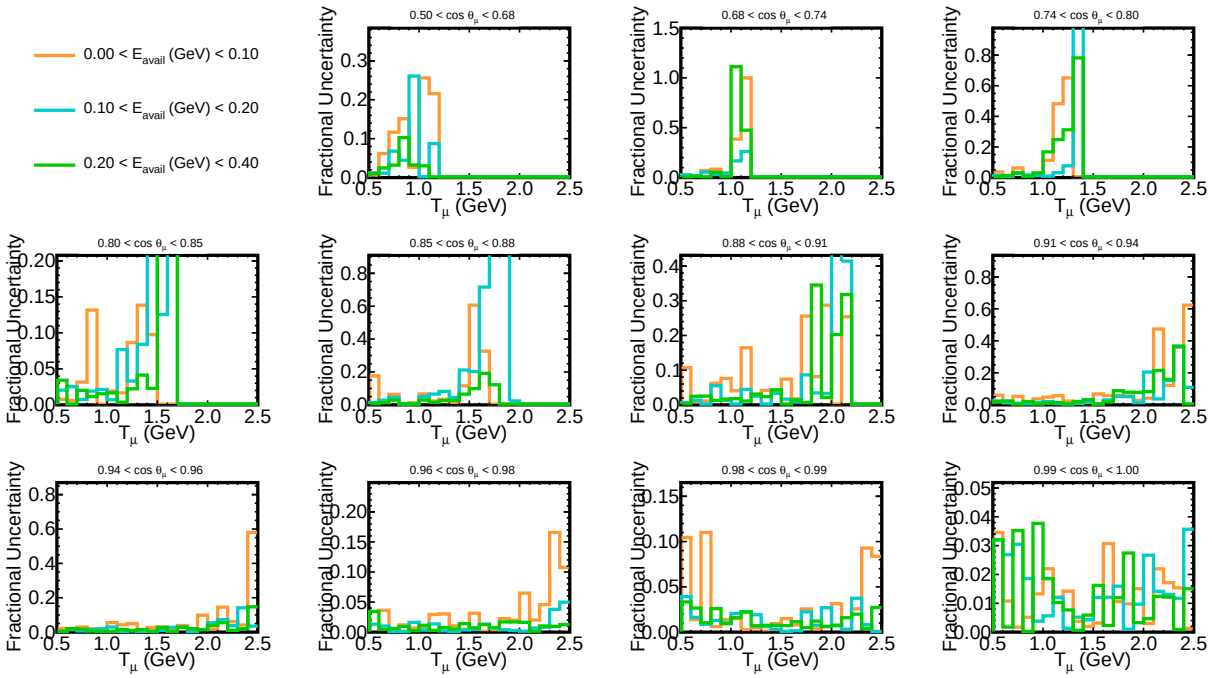

Figure 81: The fractional uncertainty between the central value cross-section and the shifted sample made to compensate for the linear drift downwards in light level over time.

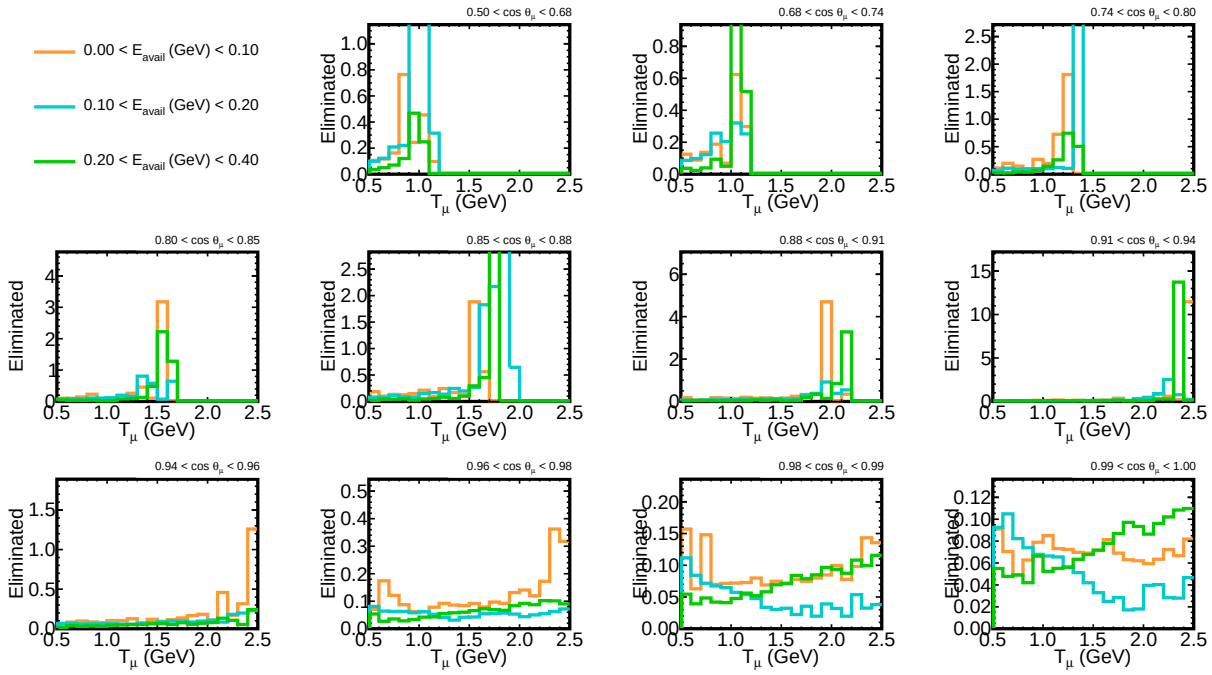

Figure 82: The fractional uncertainty introduced from the combined detector systematics.

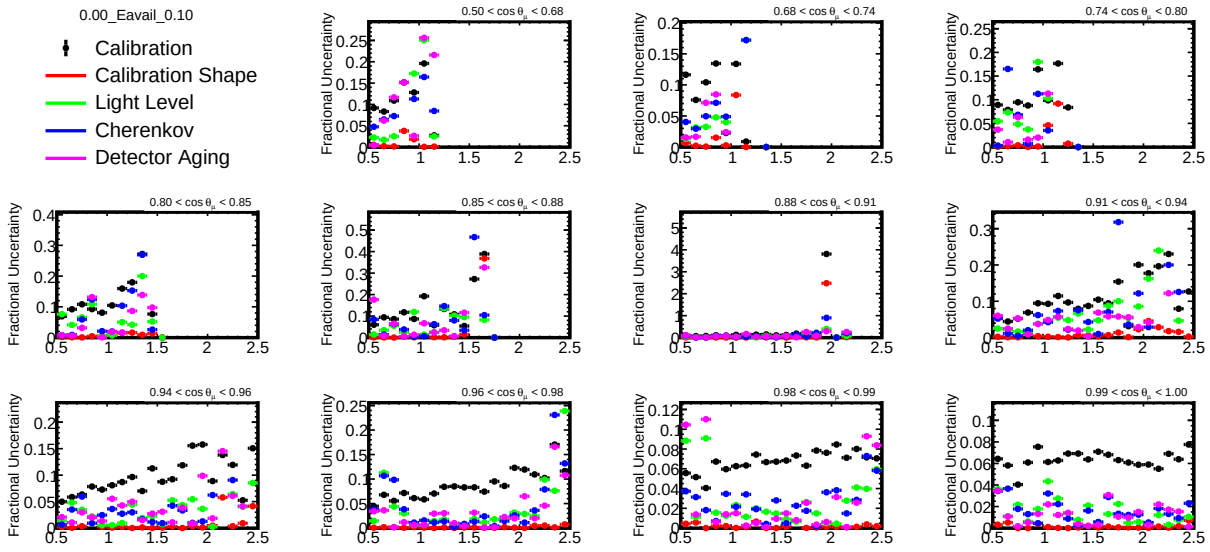

Figure 83: The fractional uncertainty on the central value cross-section due to all sources of detector uncertainty. The first E-Avail bin is shown here.

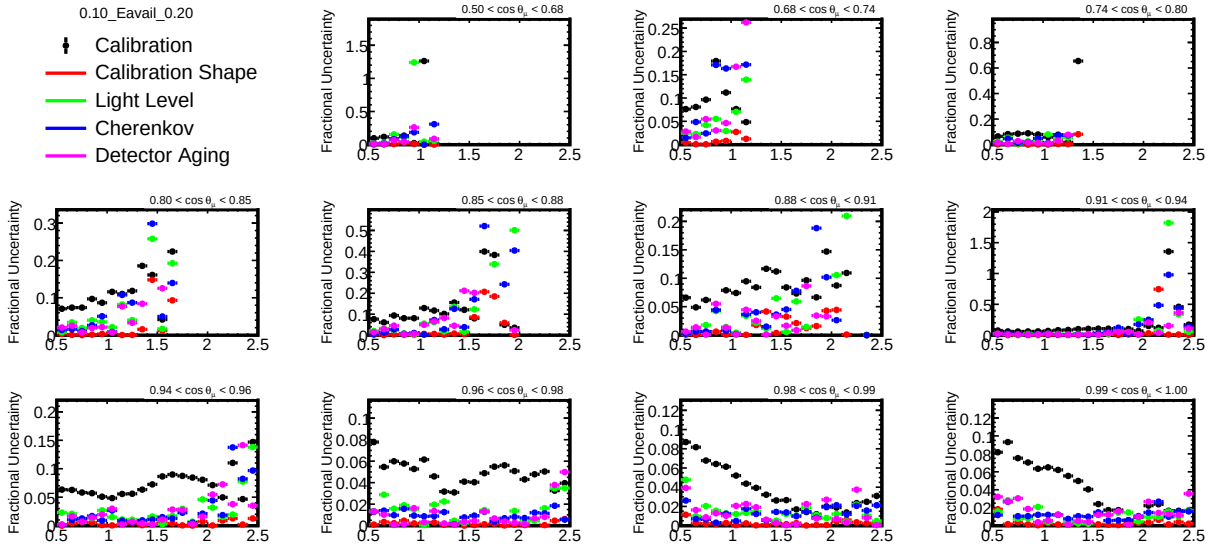

Figure 84: The fractional uncertainty on the central value cross-section due to all sources of detector uncertainty. The second E-Avail bin is shown here.

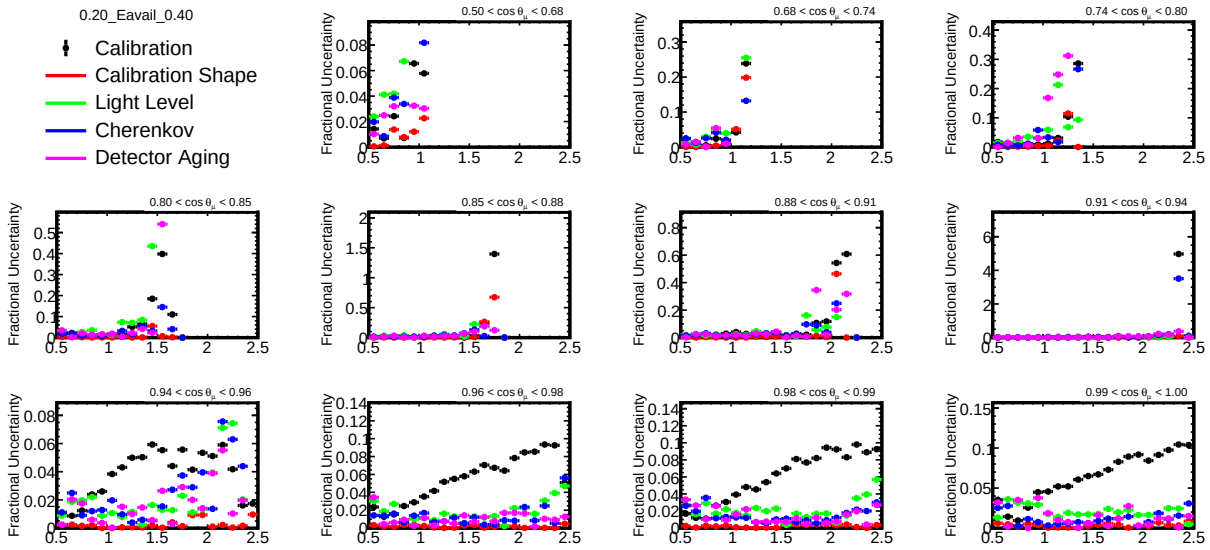

Figure 85: The fractional uncertainty on the central value cross-section due to all sources of detector uncertainty. The third E-Avail bin is shown here.

10.2 Muon Kinematic Systematics

Systematic changes to the outgoing muon kinetic energy and exit angle are modeled. These affect the reconstruction of the muon. This is to account for mis-reconstructing the data events so that the selected data distribution has sufficient coverage.

For the muon angle, the angle of the outgoing muon with respect to the beam is shifted by 10 mrad. The muon angle is shifted in both the XZ and YZ directions, both forwards and backwards. The systematics that result from these shifts can be seen in Figures 86 and 87.

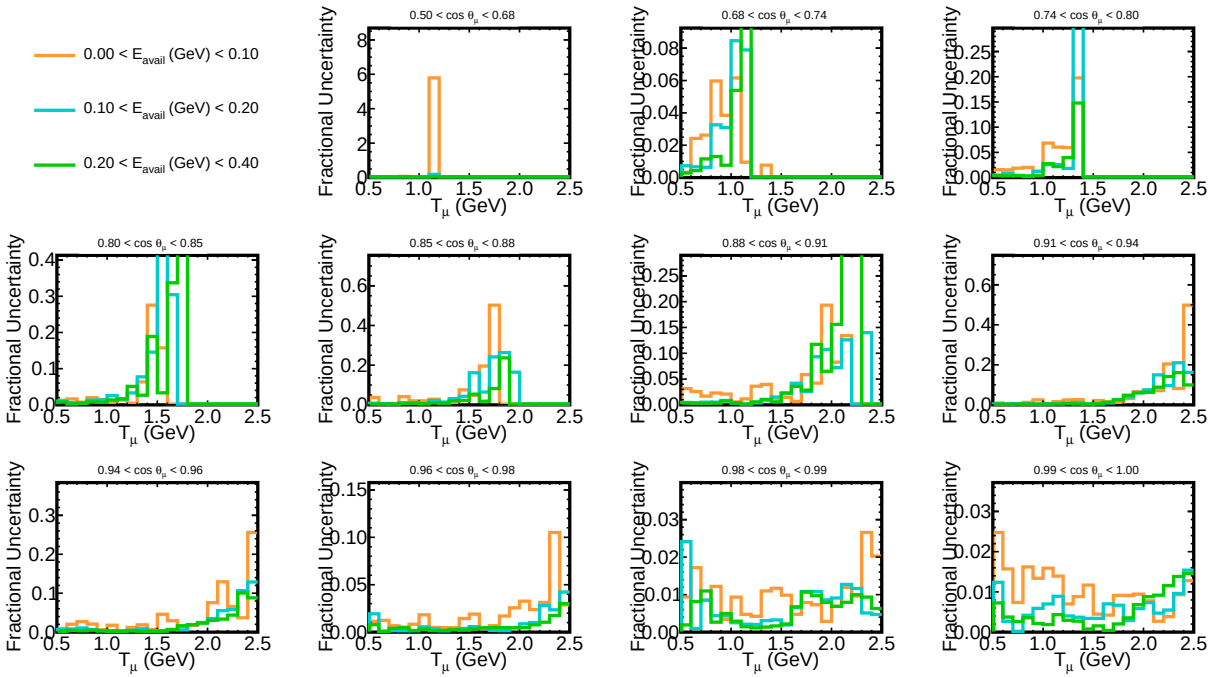

Figure 86: The fractional uncertainty between the central value cross-section and the shifted samples made from adjusting the angles of outgoing muons by ±5 mrad in the XZ direction. This uncertainty takes uses the combined covariance matrix for both the positive and negative shifts.

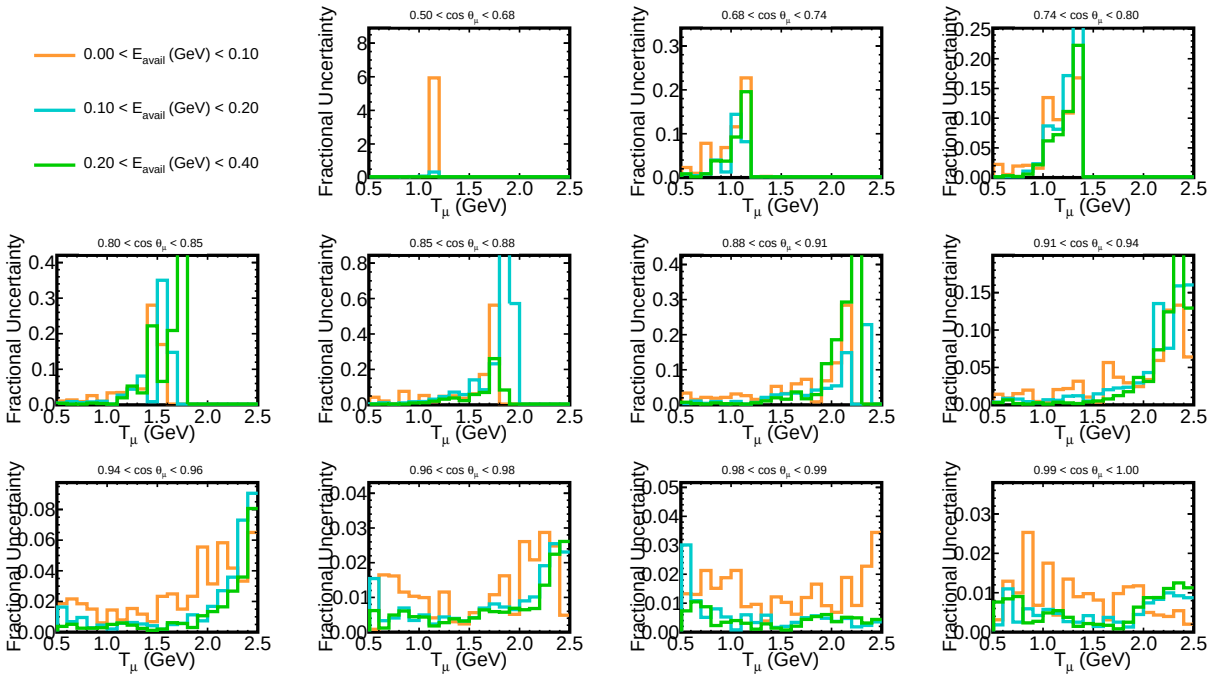

Figure 87: The fractional uncertainty between the central value cross-section and the shifted samples made from adjusting the angles of outgoing muons by ±5 mrad in the YZ direction. This uncertainty takes uses the combined covariance matrix for both the positive and negative shifts.

For the muon kinetic energy, the energy of the muon is shifted. For the muon kinetic energy up systematic, the energy of the muon in the active region is increased by a factor of 1.0079 and a by a factor of 1.0120 in the muon catcher. For the muon kinetic energy down systematic, the energy of the muon in the active region is decreased by a factor of 0.9921 and a by a factor of 0.9880 in the muon catcher. The muon kinetic energy systematic can be seen in Figure 88.

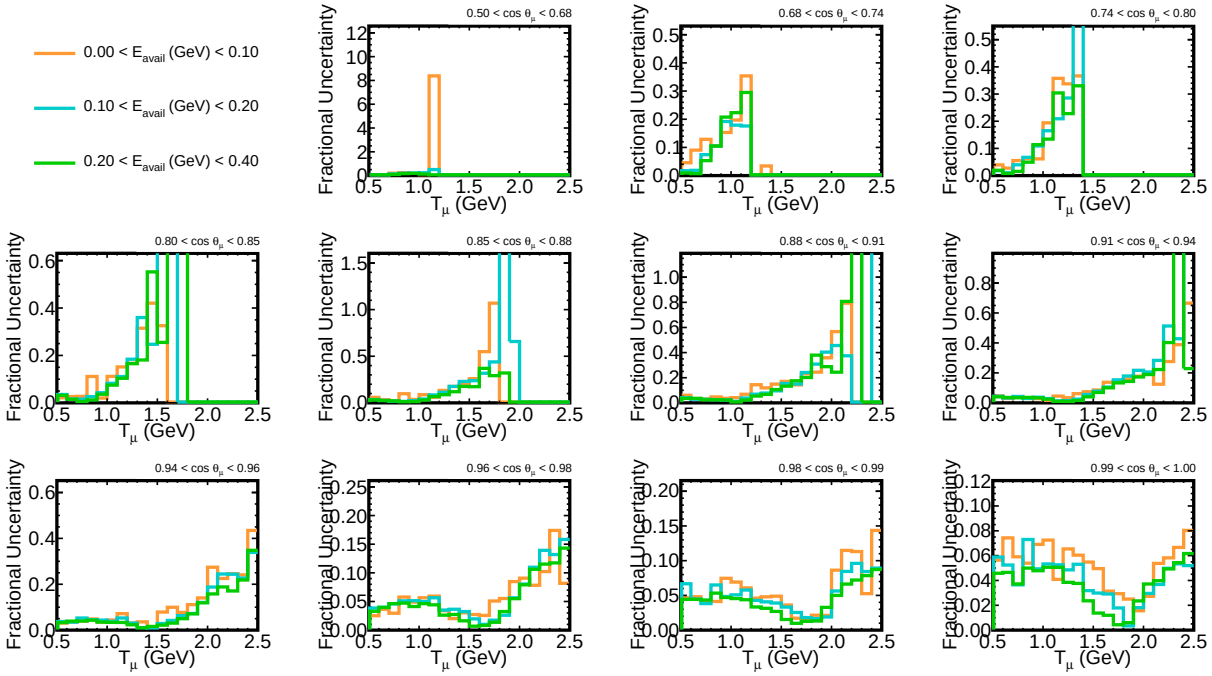

Figure 88: The fractional uncertainty between the central value cross-section and the shifted samples made from adjusting the kinetic energy of outgoing muons. This uncertainty takes uses the combined covariance matrix for both the positive and negative shifts.

10.3 Beam Systematics

These sources of systematic uncertainty are related to measurement uncertainties in certain parameters of the NuMI beamline. The list of systematics that fall under this category are:

- Horn Current
- Beam Spot Size
- Beam Position on Target
- Horn 1
- Horn 2
- Target
- Magnetic Field in Decay Pipe

- New Target
- Horn Water

The systematics in this list are treated as two-sided systematics, where the sample has a parameter shifted up or down by a specified amount, covariance matrices are calculated separately and then averaged together.

Horn Current is nominally $200kA$ and is shifted $\pm 2kA$ [37].

Beam Spot Size is nominally $1.3mm$ and is shifted $\pm 0.2mm$ in both the X and Y directions [37].

The Beam Position on Target is shifted by $\pm 1mm$ in both the X and Y direction [37].

The positions of both Magnetic Horns are separately shifted in both the X and Y directions by $\pm$3mm [37].

Target Z position is nominally located at -143.3cm and is shifted $\pm 7mm$ in the Z direction [37].

Uncertainties introduced from the addition of Magnetic Fields in the NuMI Decay Pipe are also modeled. The steel pipe can either increase the field (if magnetized during construction) or decrease the field (if shielding from the Earth's magnetic field) and the uncertainty covers the addition and subtraction of a magnetic field [37].

There was a change in the beam target to handle higher beam powers [38]. To account for this change, there was an additional systematic generated to account for replacing the target.

There is a 1mm layer of water cooling horn 1, and there is a shift of $\pm$1mm on the water level [37].

The total contribution of the beam systematics can be seen in Figure 89.

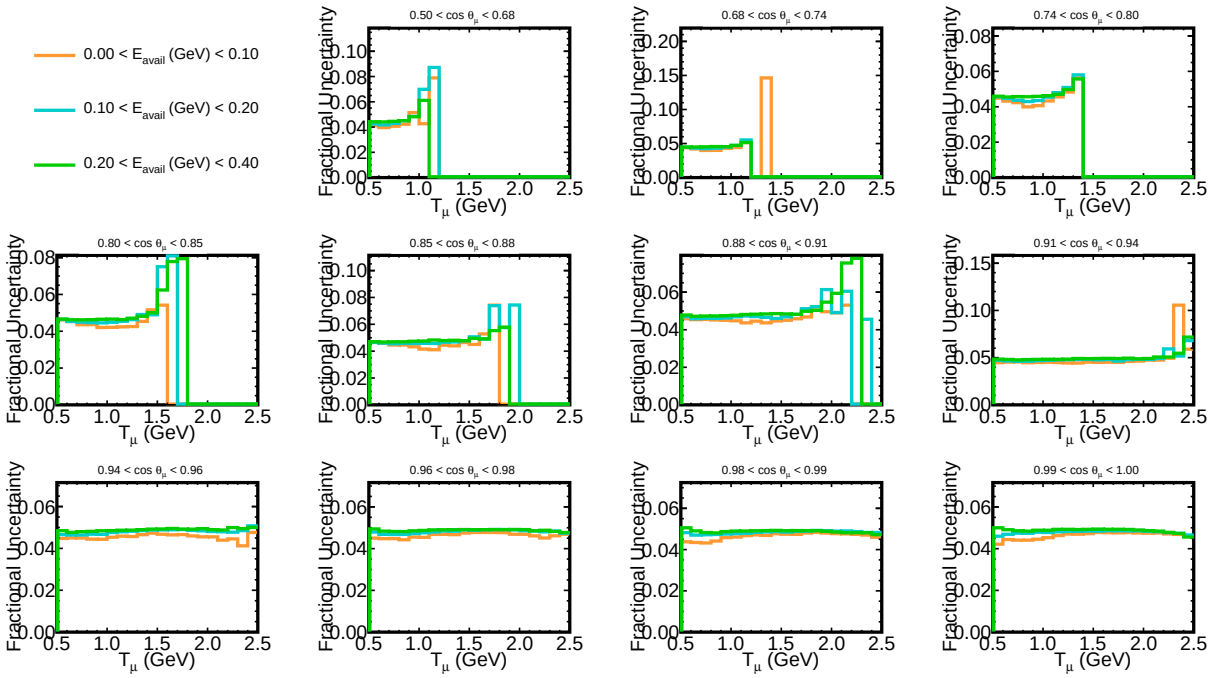

Figure 89: The fractional uncertainty introduced from the combined beam systematics

These systematics are applied as systematic shifts to the eighty percent sample of the total MC. The other twenty percent is used for the fake data sample.

10.4 Cross-Section Model Systematics

A multiverse approach is taken for the neutrino interaction systematics. A universe is taken to be a collection of physics parameters, in this case the collection of parameters GENIE uses to govern neutrino interactions [39]. These parameters govern simulations of interaction models as discussed in Chapter 4.

Each of the parameters that go into the neutrino interaction simulation is fluctuated a random amount for each universe. A random number is chosen from a normal distribution centered at 0, from -1 to 1, and each parameter is shifted by that many sigmas [39]. They are then applied as shifts to the eighty percent sample of the total MC for each universe.

There are many parameters that get shifted; they have been broken up into lists based on category. The first category is the neutrino interaction cross-section parameters. GENIE has options

for some of these parameters that affect both shape and normalization of observable distributions, and those that just affect the shape of the observable distributions (maintaining normalization) [40]. NOνA uses the options that affect both shape and normalization.

The list of these parameters is below. A form factor contains the information on the spatial distribution of the nucleus being studied [2]. In weak interactions, these form factors have a vector component and an axial vector component [2]. These components are dependent on a mass parameter called either the vector mass or the axial mass respectively [40]. The BY model is the Bodek-Yang model for DIS [21]. PDF is short for Parton Distribution Function, which are how the quarks in protons and neutrons are parameterized [21]. The BY model uses the GRV98 PDF [41]. The BY model has a scaling variable ξ_w to account for higher twist and target mass effects, which is dependent on parameters A (which accounts for higher order QCD terms) and B (which accounts for initial state quark transverse momentum and final state effective ΔM_f^2) [41]. The GRV98 PDF also contains two photoproduction limit multiplicative factors for valence quarks [41].

- Axial mass for NC Elastic
- Strange axial form factor η for NC elastic
- Z-expansion normalization factor for CCQE
- Axial mass for CC resonance neutrino production
- Vector mass for CC resonance neutrino production
- Axial mass for NC resonance neutrino production
- Vector mass for NC resonance neutrino production
- A_{HT} higher-twist parameter in BY model scaling variable ξ_w
- B_{HT} higher-twist parameter in BY model scaling variable ξ_w
- C_{V1u} u valence GRV98 PDF correction parameter in BY model

- C_{V2u} u valence GRV98 PDF correction parameter in BY model

Next is the list of neutrino induced hadronization and resonance decay parameters:

- Pion transverse momentum (p_T) for $N\pi$ states in AGKY (hadronization model developed to improve MC simulations for the MINOS experiment [40]
- Pion Feynman x (x_F) for $N\pi$ states in AGKY
- Branching ratio for radiative resonance decays
- Branching ratio for single-η resonance decays
- Pion angular distribution in $\Delta \rightarrow \pi N$ (isotropic $\leftrightarrow$ RS)

In addition to the GENIE Knobs, NOνA has their own set of custom knobs.

There are six parameters for the NOνA custom knobs for QE interactions. These include two parameters for RPA (Random Phase Approximation, see Chapter 2) CC-QE enhancement and suppression and four parameters for the Z-Expansion coefficients [20]. The Z-Expansion normalization has already been listed among the parameters that come from GENIE.

There are five parameters for the NOνA custom knobs for RES interactions. This includes one parameter for Low-Q^2 (four-momentum transfer squared) Suppression, two parameters for RES Δ and higher-order normalization scaling, and two parameters for relative RES cross-section scaling of $\frac{\sigma(\nu_p)}{\sigma(\nu_n)}$ (one for neutrinos, one for anti-neutrinos) [42].

There are six parameters for the NOνA custom knobs for MEC interactions, three pairs of parameters that include one parameter for the neutrino interaction and one parameter for the anti-neutrino interaction. These include one pair for the MEC Shape uncertainty, one pair for the neutrino energy cross-section dependence, and one pair for the initial state of the struck nucleon pair (the fraction of nn(pp) or np pairs) [20].

There are thirty-five parameters for the NOνA custom knobs for DIS interactions. This includes one parameter for the DIS formation zone (a distance constant that determines how far partons

may travel before they coalesce into hadrons) [20]. This also includes two parameters for relative scaling of DIS interactions with two final state hadrons (one for neutrinos, one for anti-neutrinos) and thirty-two parameters for transition-DIS events implementing a fifty percent normalization uncertainty with options for neutrinos vs anti-neutrinos, CC vs NC, whether interacting on a neutron or a proton and number of pions (0, 1, 2, >2) [43].

There are four parameters for the NOνA custom knobs for FSI hN model. These include one for the mean free path scale, and three for the fate fraction scale parameters (i.e. absorption, charge exchange and QE scattering) [20].

There are three additional parameters that were taken from the T2K experiment to account for effects that affect ν_e and $\overline{\nu_e}$ cross-sections but not ν_μ and $\overline{\nu_\mu}$ cross-sections [44]. These include two parameters of uncorrelated two percent uncertainties on the ν_e/ν_μ and $\overline{\nu_e}/\overline{\nu_\mu}$ ratios to account for radiative corrections [44]. And one parameter for a two percent uncertainty that is anti-correlated between ν_e and $\overline{\nu_e}$ to allow for second class currents [44].

Two additional parameters were made for coherent pion scattering to replace parameters from GENIE that were broken. These describe the axial mass for CC and NC coherent pion production and the nuclear size parameter controlling π absorption in RS model.

The result of the GENIE Systematic can be seen in Figure 90.

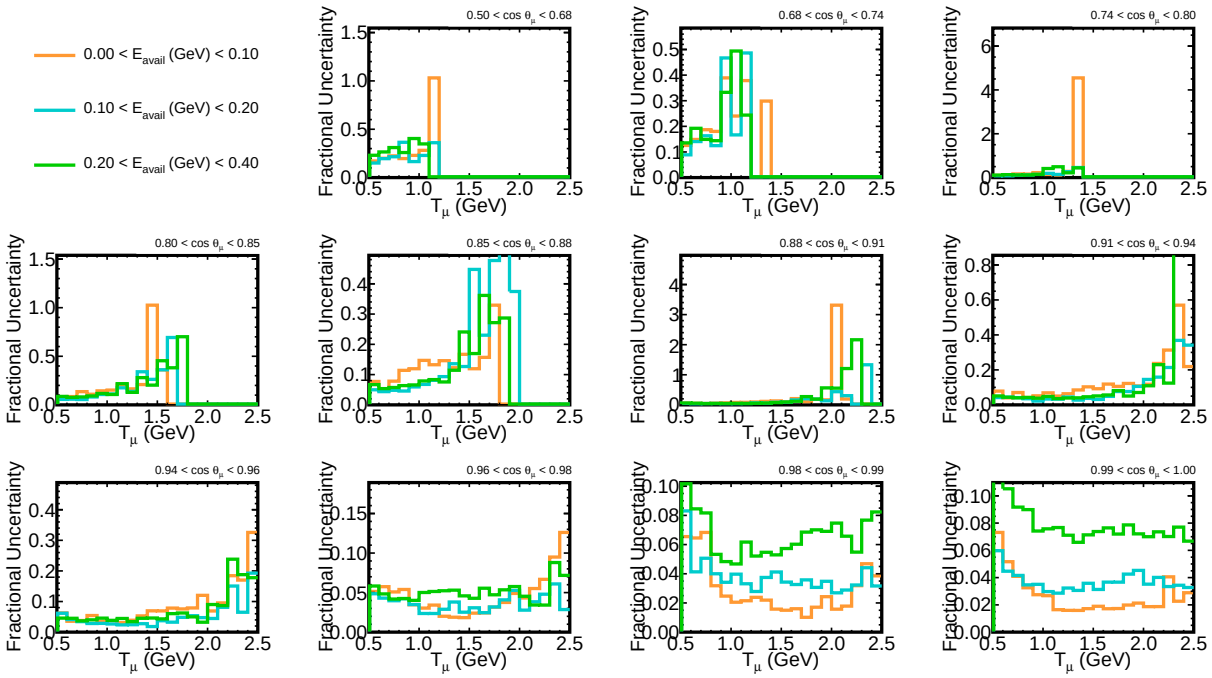

Figure 90: The fractional uncertainty between the central value cross-section and the shifted samples made from randomly fluctuating each of the parameters GENIE uses to govern neutrino interactions. This Uncertainty takes uses the normalized covariance matrix over 1000 universes.

10.5 PPFX Systematics

A multiverse approach is taken for the flux modeling systematics. These are uncertainties related to modeling proton interactions in the beam target that produce hadrons which decay into neutrinos. PPFX is the simulation package for the neutrino flux. All the uncertain parameters in the PPFX package are fluctuated by a random amount in $\pm 1\sigma$, particularly the hadron production cross-sections [45]. Figure 91 shows the uncertainties of each type of hadron interaction. Most of the uncertainties are determined by comparisons with data. These types include the following [45]:

- Pion produced from proton - carbon interactions ($pC \to \pi X$)
- Kaon produced from proton - carbon interactions ($pC \to KX$)
- Nucleon produced from proton - carbon interactions ($pC \to NX$)
- Pion produced from neutron - carbon interactions ($nC \to \pi X$)

- Nucleon incident (nucleon-A): nucleon interactions not covered by the above categories. The main contributors are:
  - Nucleons scattering on targets other than carbon (mostly helium, iron and aluminum). A material scaling is applied for these.
  - QE interactions where there is an assumed forty percent uncertainty.
  - Pion and kaons from nucleon interactions outside the direct data coverage
- Meson Incident - interaction with incident pion or kaon. PPFX does not use data for this type of interaction, a 40 percent uncertainty is applied split by incident particle and produced particle
- Other - forty percent uncertainty for interactions not covered by any of the previous categories.

In addition to the hadron production uncertainties, there are uncertainties due to particle attenuation as well. These include target attenuation (accounting for interaction probability correction for primary and secondary protons on the target) and absorption (where a dataset survey of all inelastic and absorption cross-sections was used to make assign an uncertainty to cover most of the data) [45]. Both of these uncertainties are shown in Figure 91 as well.

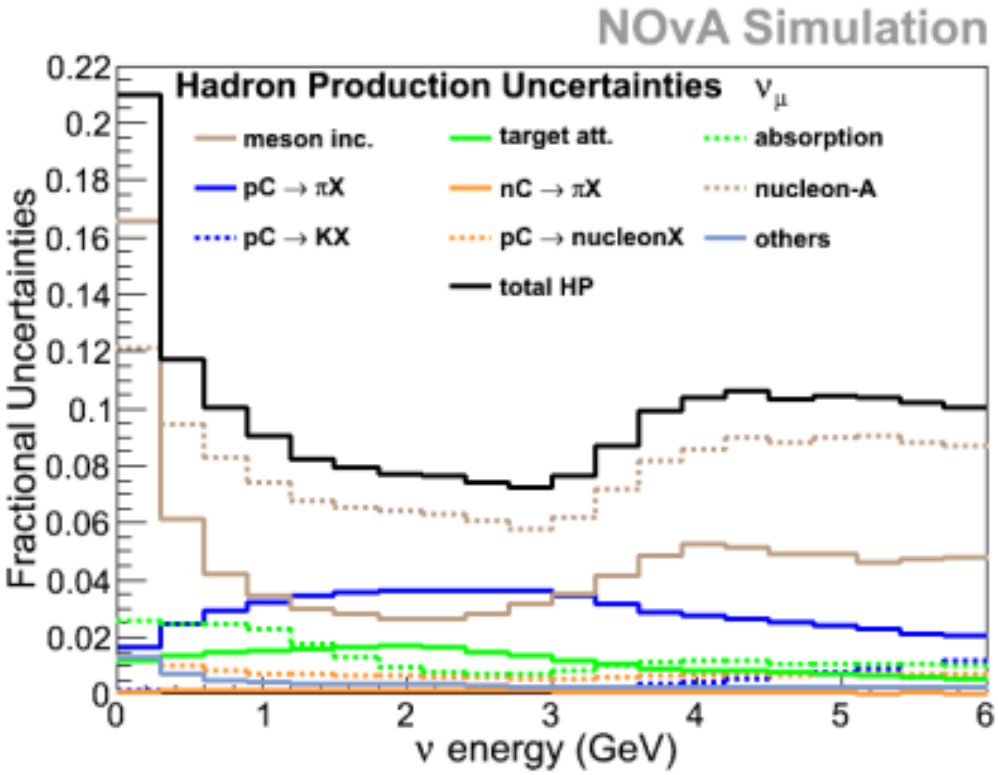

Figure 91: Sources of uncertainties that contribute to the PPFX systematic, these include hadron production uncertainties and uncertainties due to particle attenuation. [45]

One hundred universes are generated. The PPFX Systematic can be seen in Figure 92.

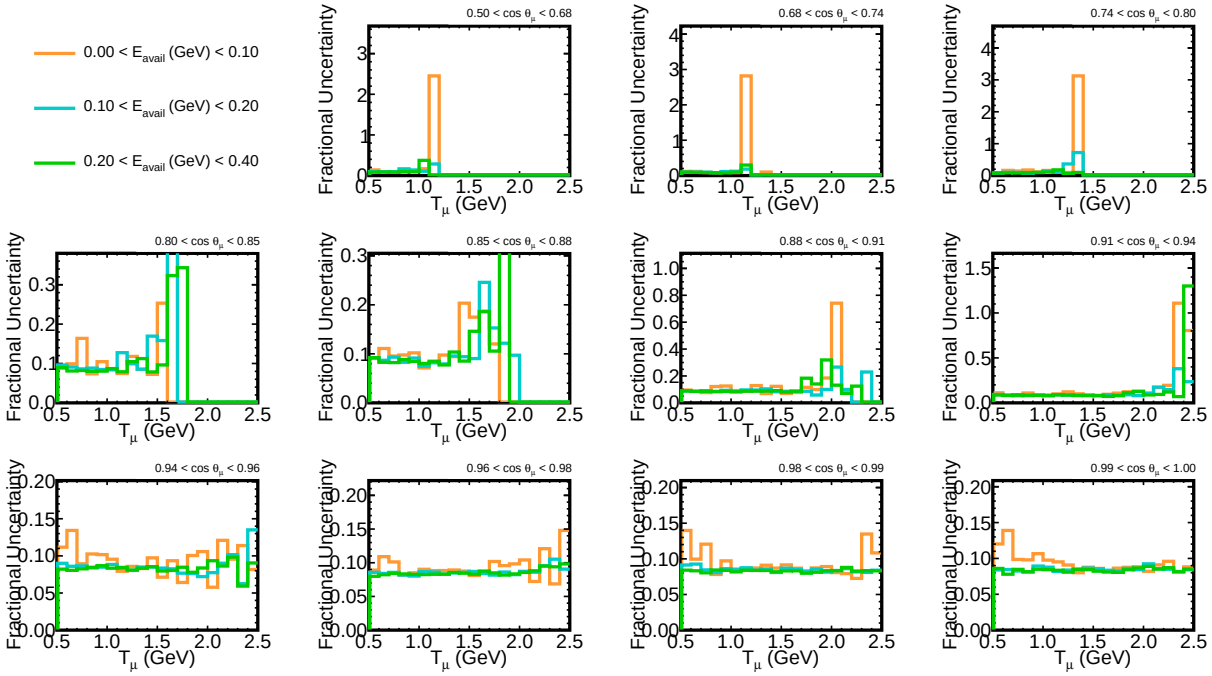

Figure 92: The fractional uncertainty between the central value cross-section and the shifted samples made from randomly fluctuating each of the parameters the PPFX package uses to govern the neutrino flux (particularly hadron production cross-sections). This uncertainty takes uses the normalized covariance matrix over 100 universes.

10.6 Neutron

Like neutrinos, neutrons are particles with neutral charge whose trace in the detector is left by daughter particles instead of the neutrons themselves. In NOνA, neutrons primarily interact via inelastic scattering. There was an additional systematic added to cover for uncertainties introduced by neutrons. The MENATE package for modeling neutron propagation was found to have better agreement with NOνA data over the GEANT4 predictions used in making the central value MC [46]. To estimate the uncertainty introduced from neutrons, a cross-section was measured by replacing the GEANT4 neutron interaction model with the MENATE model and performing the cross-section measurement as described in Chapter 7, and comparing with the central value cross-section. The neutron systematic can be seen in Figure 93.

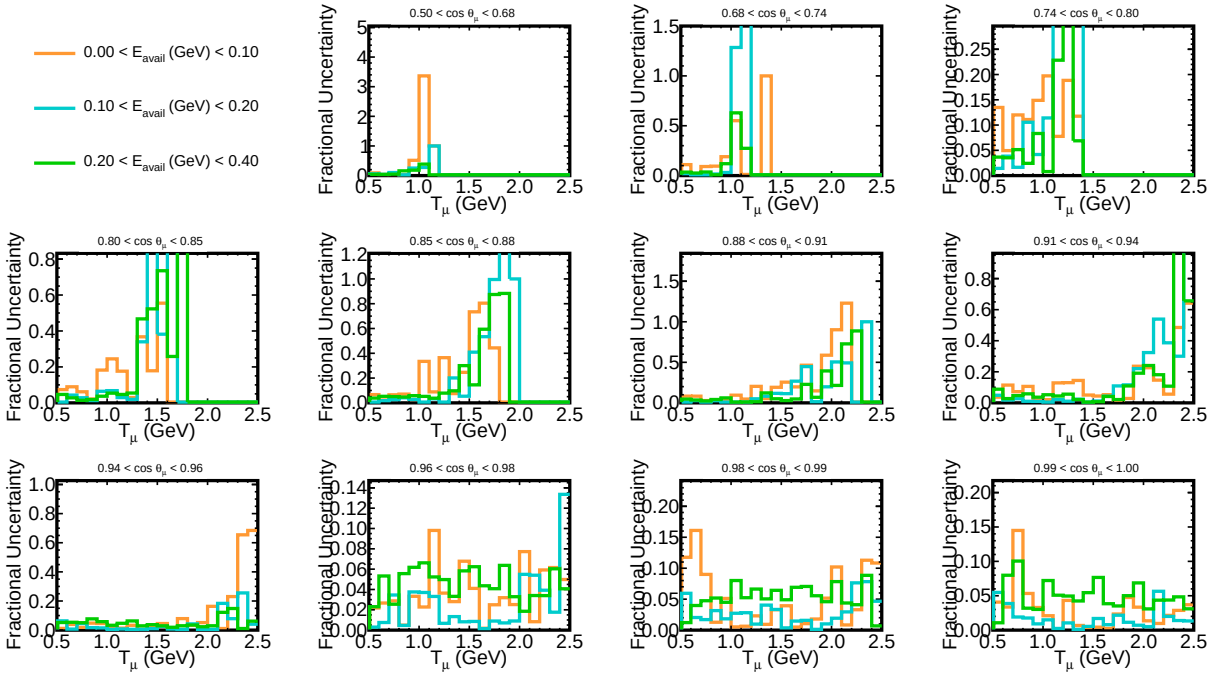

Figure 93: The fractional uncertainty between the central value cross-section and the shifted samples made from replacing the GEANT4 neutron interaction model with the MENATE model.

10.7 MEC Weight

As described in Chapter 8, it was found that there a mismatch in the closure test results caused by an issue with the MEC weights. Fixing the closure test required there to be a cap placed on the MEC weights. To test how much an impact this had on the results, the covariance matrix was measured and the fractional uncertainty was determined from it. The systematic introduced from this can be seen in Figure 94.

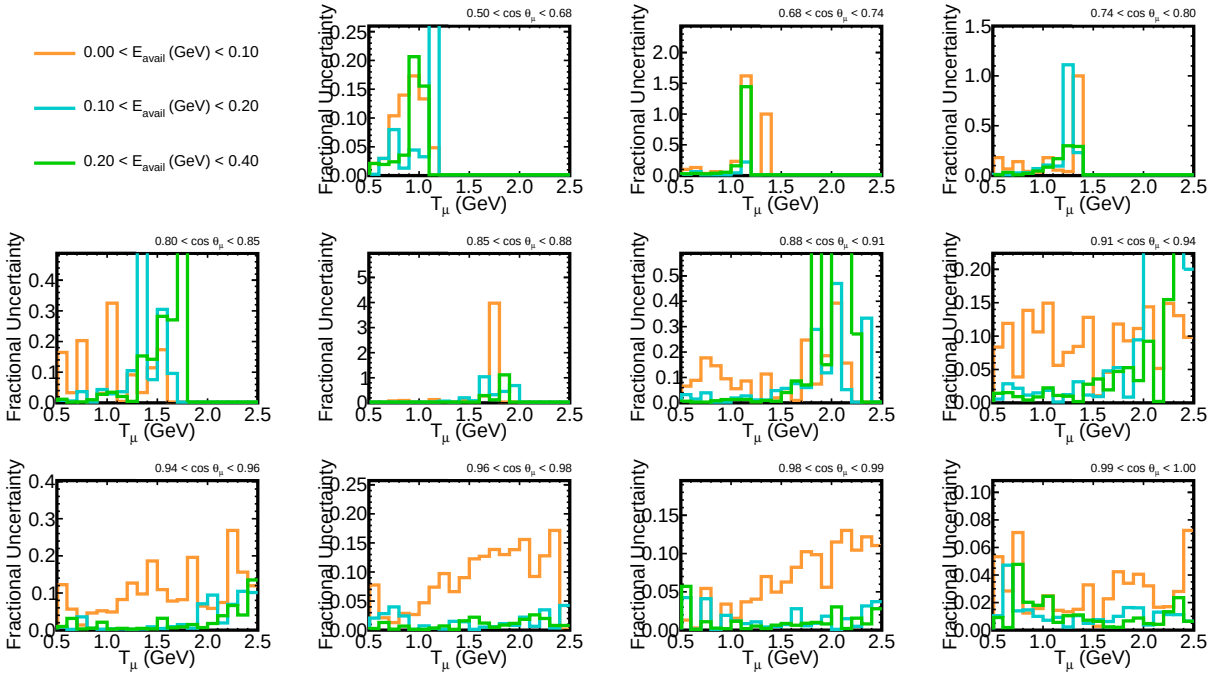

Figure 94: The fractional uncertainty between the central value cross-section and the shifted samples made capping the value of the MEC weight at fifty.

10.8 MEC Model Spread

To model the effect of the choice in MEC model on the cross-section, a multiversal approach was taken [47]. Three models were used to create distributions of neutrinos: the Dytman [48], SuSA [49] and Valencia [50] models. Three random scaling factors are generated and applied to each distribution. Then these distributions are combined to create a unique composite model. This distribution is divided by the default Valencia distribution to obtain the final MEC weights (the data-driven corrections to the GENIE predictions in MC for MEC) for this unique combination. This process is repeated 1000 times to generate 1000 unique models. The uncertainty resulting from this can be seen in Figure 95.

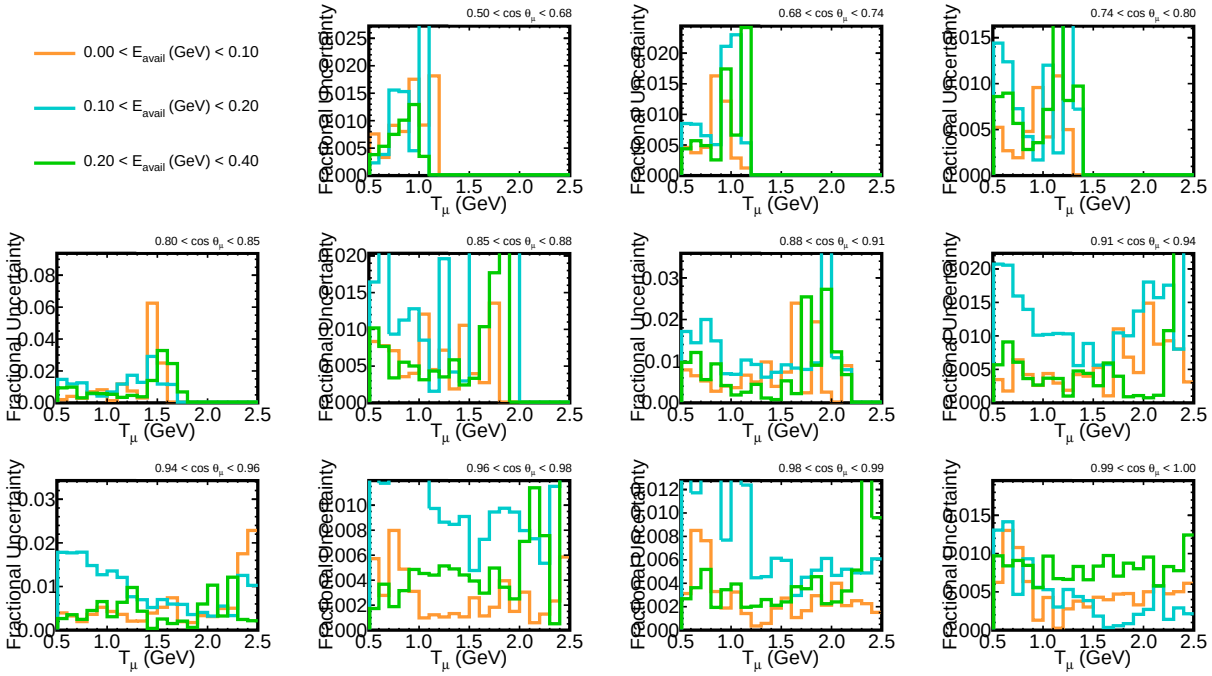

Figure 95: The fractional uncertainty between the central value cross-section and the shifted samples made generating 1000 universes with a random combination of Valencia, SuSA and Dytman MEC models.

10.9 Statistical

To estimate the statistical uncertainty, 3000 universes are made from fluctuating the twenty percent fake data distribution. The fake data selected signal distribution is fluctuated randomly using a Poisson distribution. The cross-section is measured for each universe, and a covariance matrix is made comparing each universe to the central value cross-section. The covariance matrices are added together and then normalized over the 3000 universes. The statistical uncertainty can be seen in Figure 96.

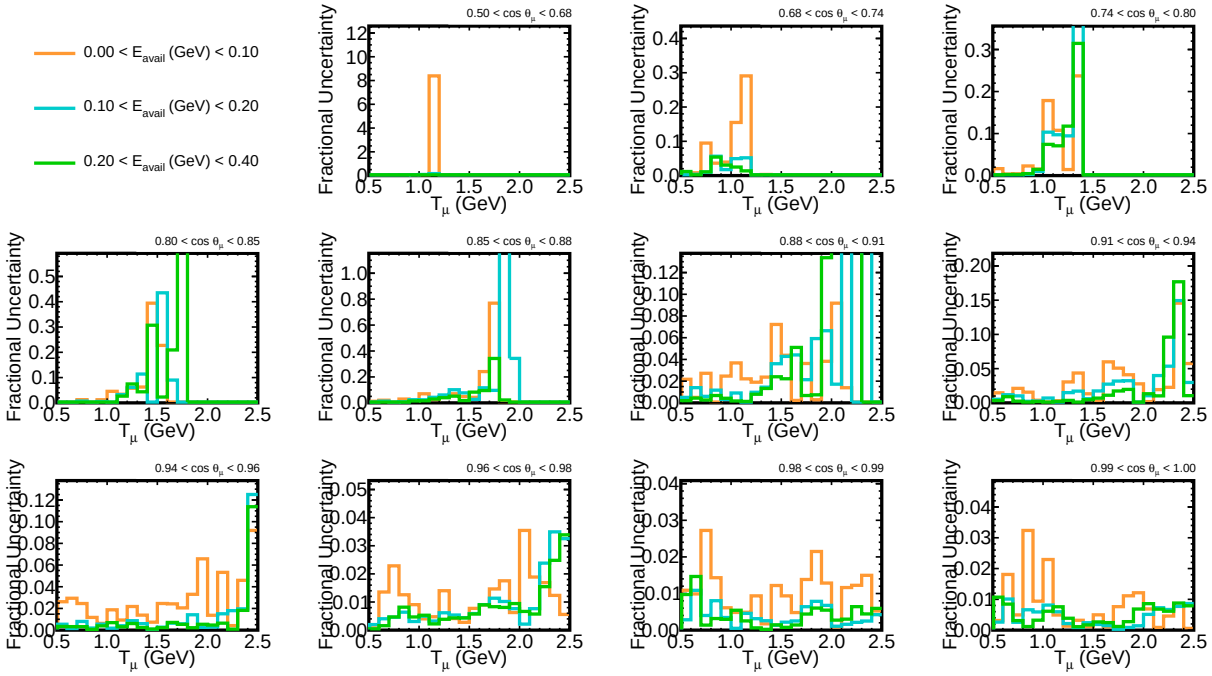

Figure 96: The fractional uncertainty between the central value cross-section and the shifted samples made from randomly fluctuating the fake data 3000 times using a Poisson distribution.

10.10 Total Uncertainty

A summary of all the different sources of uncertainty can be seen in Figures 97, 98, and 99, which show the contributions of each category of uncertainty to the total. A summary table of the average fractional uncertainty can be seen in table 9.

Each source of uncertainty is added in quadrature to the total. The total uncertainty on the cross-section measurement can be seen in Figure 100.

The measured central value cross-section with the total fractional uncertainty applied can be seen in Figures 101, 102, 103.

Table 9: Average fractional uncertainty from each source of uncertainty on the cross-section from the fake data central value.

Source	Contribution
Detector	0.56
Muon Kinematics	0.11
Beam	0.050
GENIE	0.24
PPFX	0.05
Neutron	0.12
MEC Weight	0.042
MEC Model	0.0030
Statistical	0.028
Total	0.56

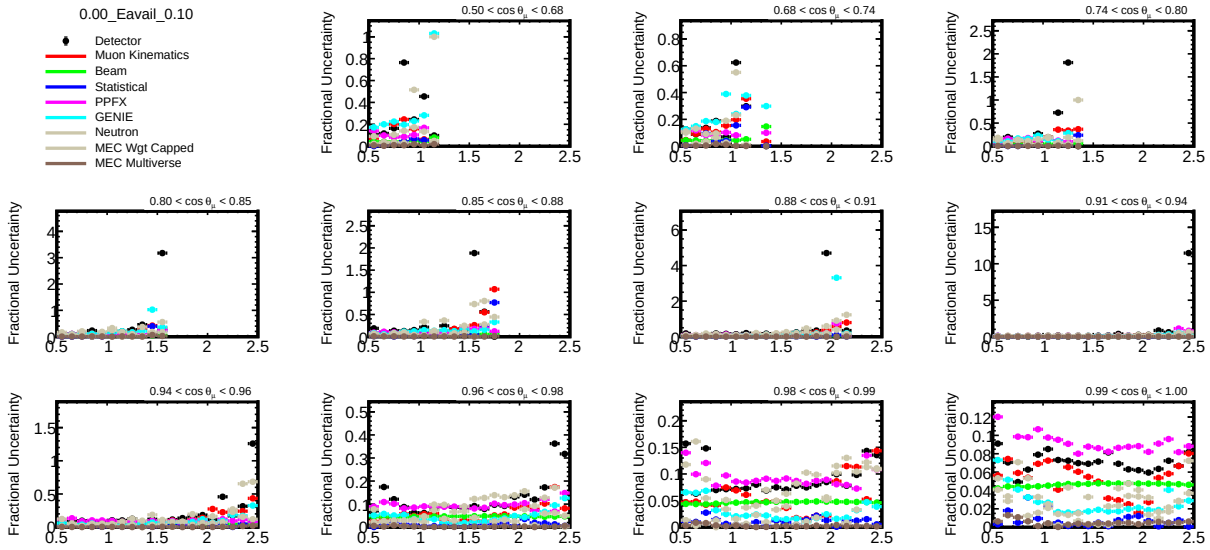

Figure 97: The fractional uncertainty on the central value cross-section due to all sources of uncertainty. The first E-Avail bin is shown here, with the systematics separated by category.

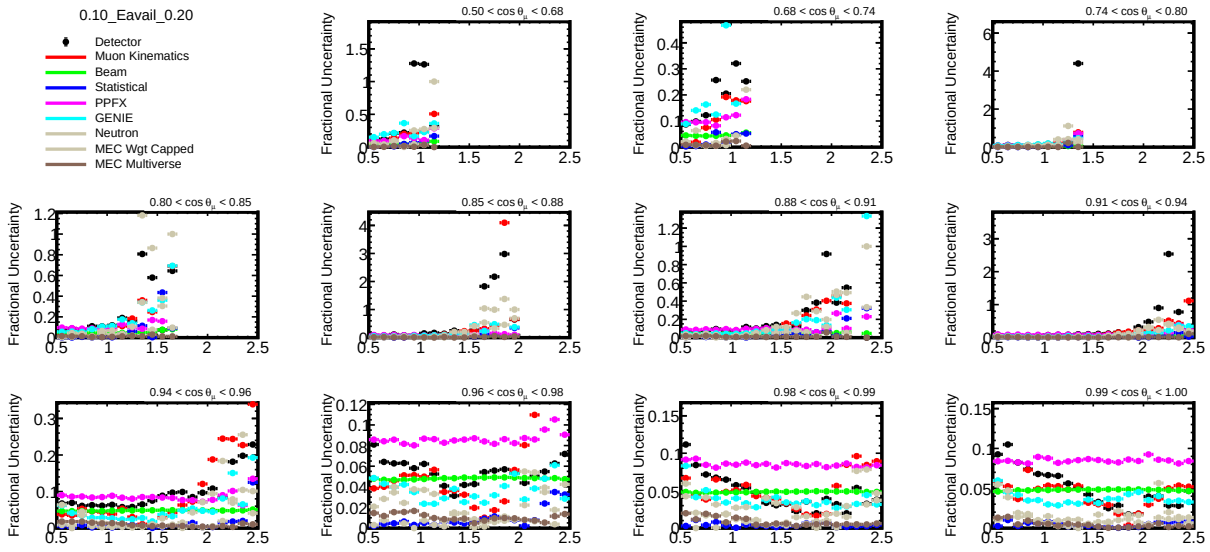

Figure 98: The fractional uncertainty on the central value cross-section due to all sources of uncertainty. The second E-Avail bin is shown here, with the systematics separated by category.

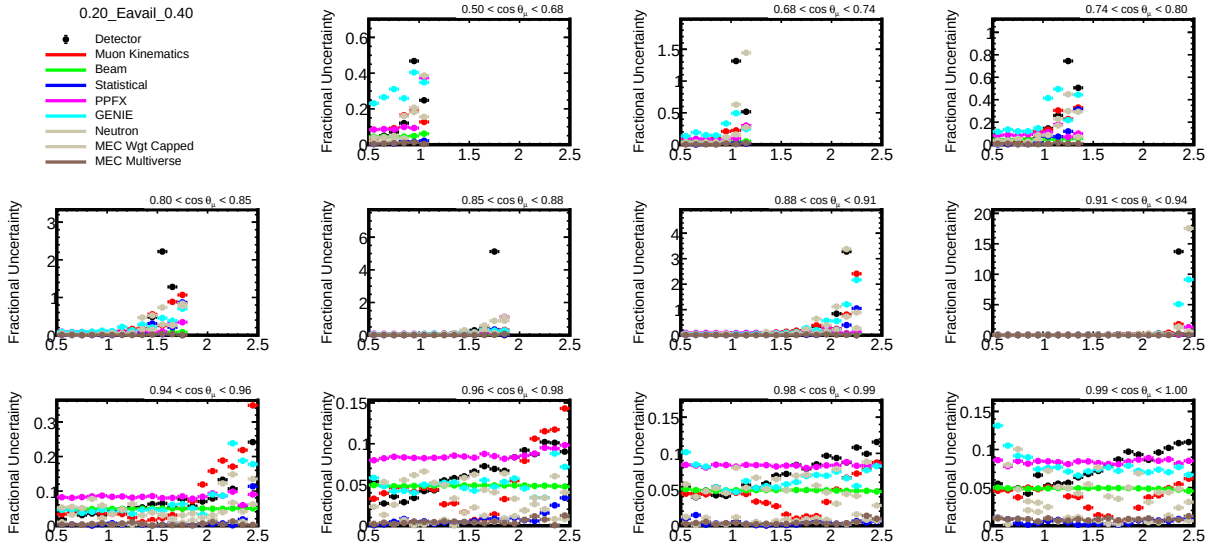

Figure 99: The fractional uncertainty on the central value cross-section due to all sources of uncertainty. The third E-Avail bin is shown here, with the systematics separated by category.

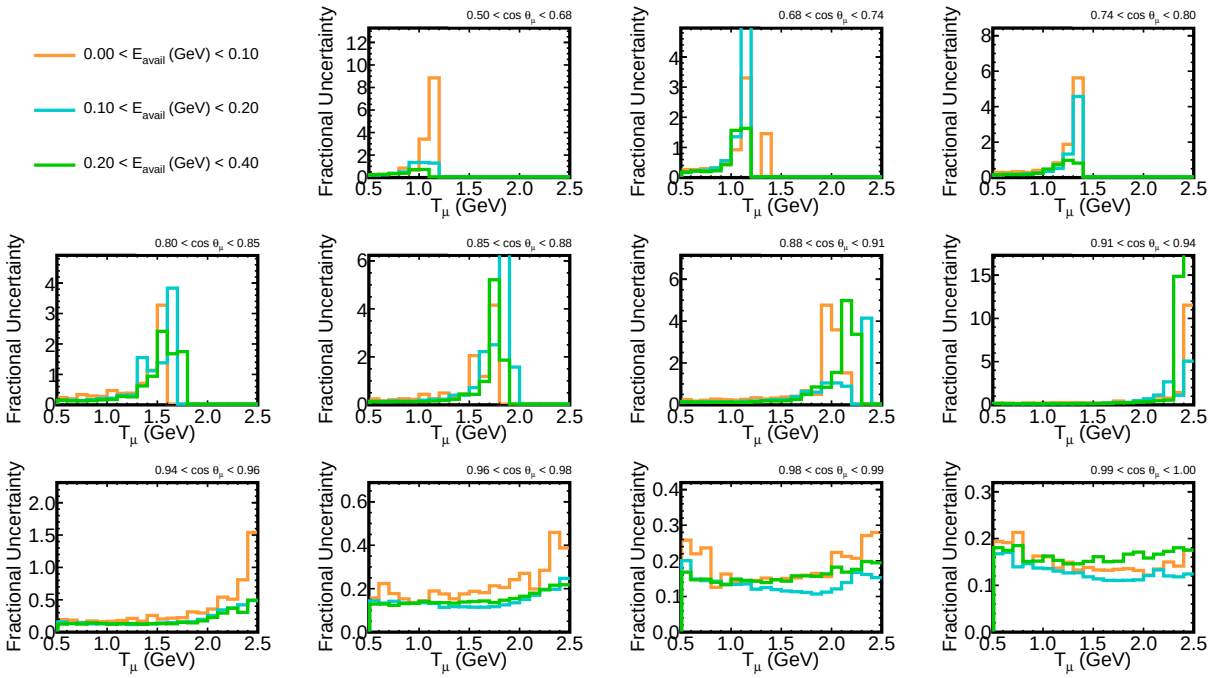

Figure 100: The total fractional uncertainty on the central value cross-section due to all sources of uncertainty.

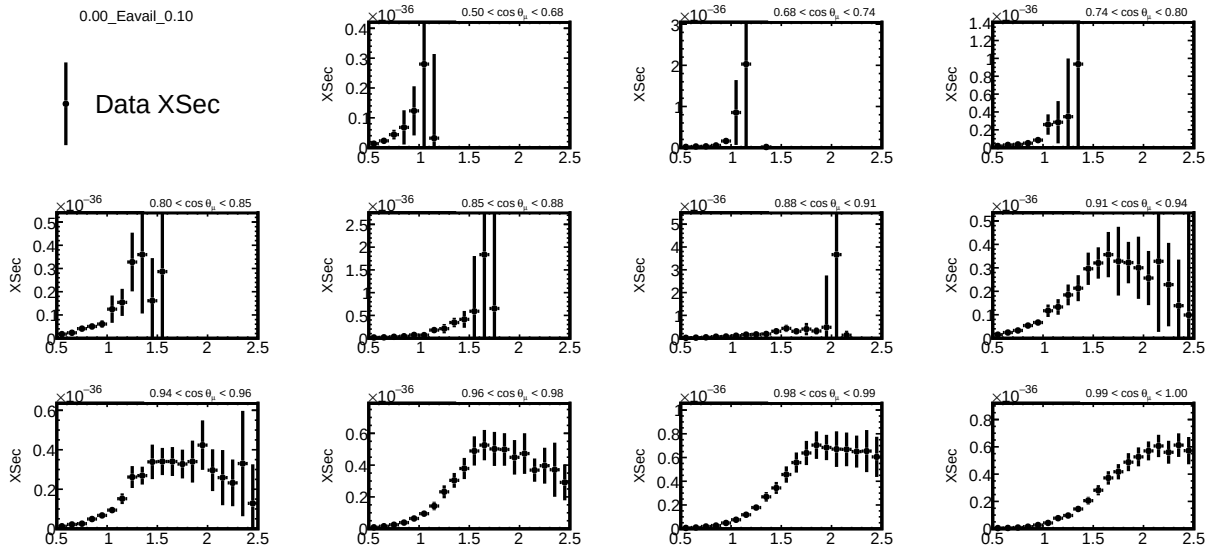

Figure 101: The measured central value cross-section with the total uncertainty applied. Shown is the first E-Avail bin

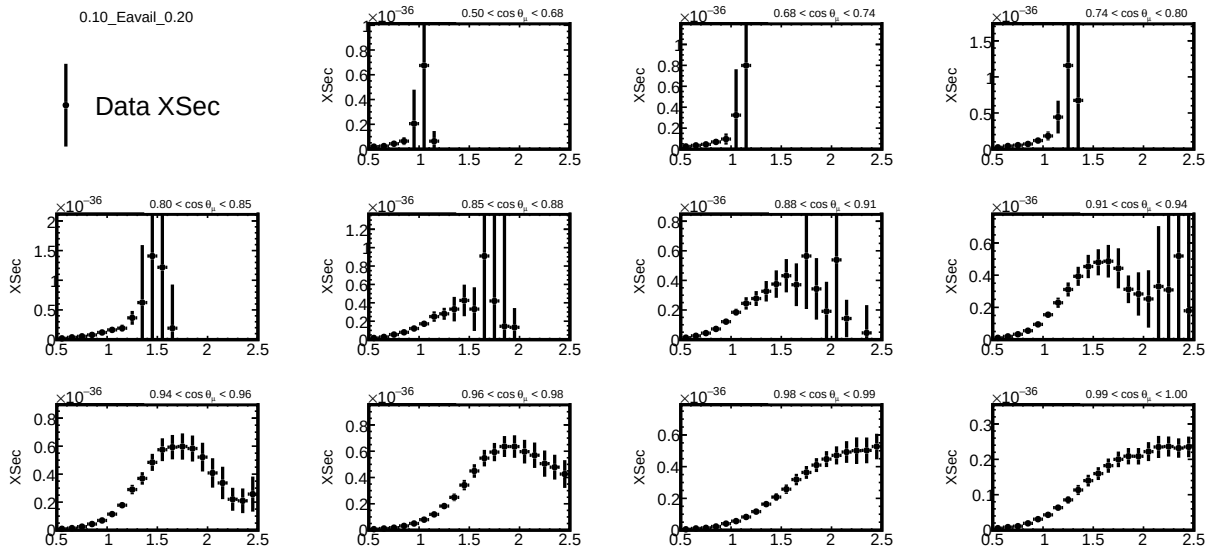

Figure 102: The measured central value cross-section with the total uncertainty applied. Shown is the second E-Avail bin

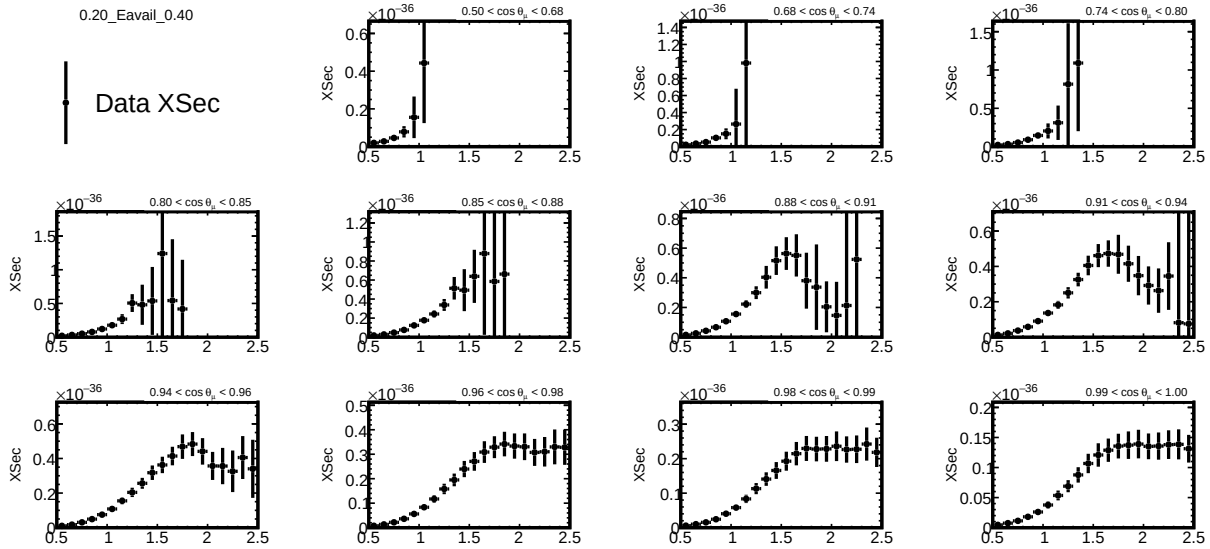

Figure 103: The measured central value cross-section with the total uncertainty applied. Shown is the third E-Avail bin

11 Data Comparisons

The process for the Full-Chain outlined in Chapter 7 is repeated, but this time with real data used in place of the fake data. One-hundred percent of the Monte Carlo simulation events were used to construct the unfolding matrix for all unfolding done with the real data, as well as the purity and the efficiency.

The selected events of the data can be seen in Figure 104. The peak of the data events is in the $0.96 < \cos\theta_\mu < 0.98$ bin, in the region of 1.3-1.7 GeV for T_μ, in the 0.10-0.20 and 0.20-0.40 GeV E-Avail bins. The peak shifts towards the most forward going bin in the 0-0.10 GeV E-Avail bin in the region of 1.6-2.0 GeV T_μ. In general the outgoing muons have less energy the further from the forward direction they are, and there are fewer of them overall.

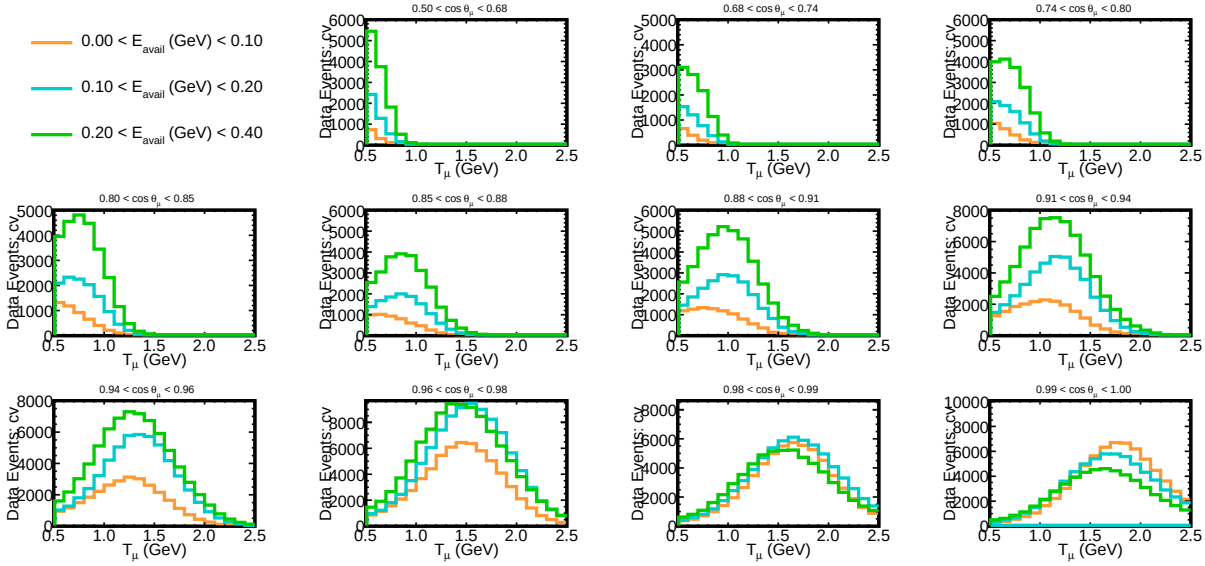

Figure 104: Panel of the selected events of the data in reconstructed variables

The unfolded real data events can be seen in Figure 105. The peak has shifted to the $0.91 < \cos\theta_\mu < 0.94$ bin in the 1.1-1.6 GeV T_μ range, with the 0.2-0.4 GeV E-Avail bin dominating in that bin. The 0-0.1 GeV E-Avail bin dominates more in the forward going bins. The other trends from the pre-unfolded data are retained.

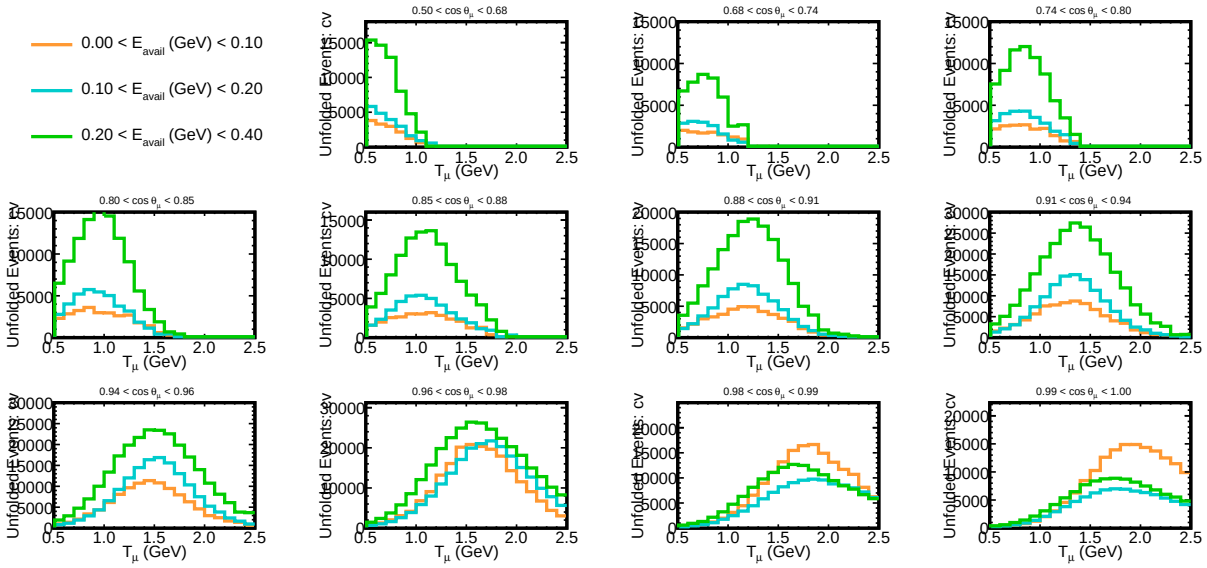

Figure 105: Panel of the unfolded selected signal events in bins of true muon kinetic energy, true cosine of the angle of the muon, and true E-Avail. Two iterations of unfolding are done to get this result.

The measured cross-section can be seen in Figure 106. The peaks shift towards higher values of T_μ due to the lower values of efficiency at higher T_μ values. The peaks of the 0.1-0.2 and 0.2-0.4 GeV E-Avail bins shift into the $0.88 < \cos\theta_\mu < 0.91$ bin, and the peak of the 0-0.1 E-Avail bin shifts into the $0.98 < \cos\theta_\mu < 0.99$ bin. Low statistics bins with low efficiencies cause some bins to have unusually high cross-sections, which feed into high uncertainties.

The selected data events were unfolded using all of the shifted systematic samples described in Chapter 10. The data was Poisson fluctuated as described in Chapter10, to measure the statistical uncertainty. Three thousand universes were generated and unfolded using the non-shifted 100 percent MC sample.

The total fractional uncertainty contribution from the detector response can be seen in Figure 107. The average fractional uncertainty was evaluated to be 0.47, however this is notably pulled up due to low statistics bins significantly raising the average. The uncertainty is on the scale of ten percent in bins where there are good statistics.

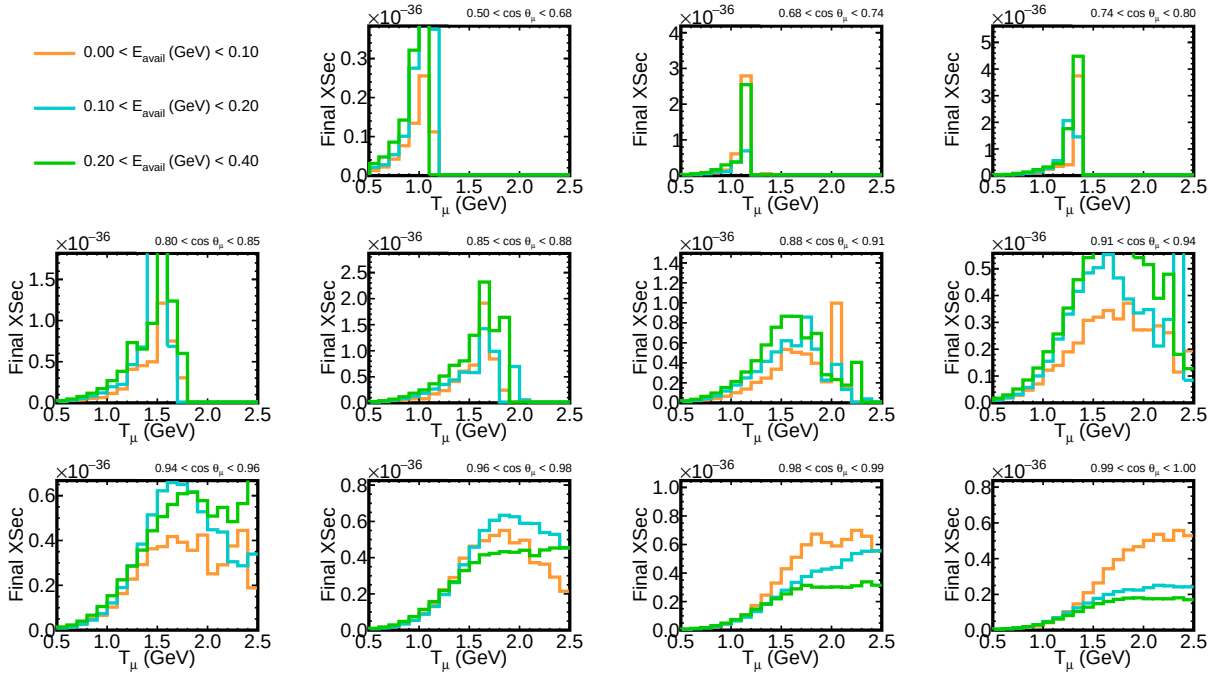

Figure 106: The measured triple differential cross-section in bins of true muon kinetic energy, true cosine of the angle of the muon, and true E-Avail using real data

The total fractional uncertainty contribution from the muon kinematic uncertainty can be seen in Figure 108. The average fractional uncertainty was evaluated to be 0.12. The effect of low-statistics bins is seen here too, but the effect is not as dramatic as on the detector systematics. In general the bins with good statistics have uncertainties between three and eight percent.

The total fractional uncertainty contribution from the beam systematics can be seen in Figure 109. The average fractional uncertainty for the beam systematics was evaluated to be 0.064. The effect of low statistics bins is not as dramatic as the detector systematics, and the uncertainty is around a flat four to five percent uncertainty in most bins.

The total fractional uncertainty contribution from the GENIE systematics can be seen in Figure 110. The average fractional uncertainty was evaluated to be 0.39. The effect of low statistics bins is substantial on the GENIE systematic, the average for most bins is around five percent; there are a few bins that dramatically raise the average.

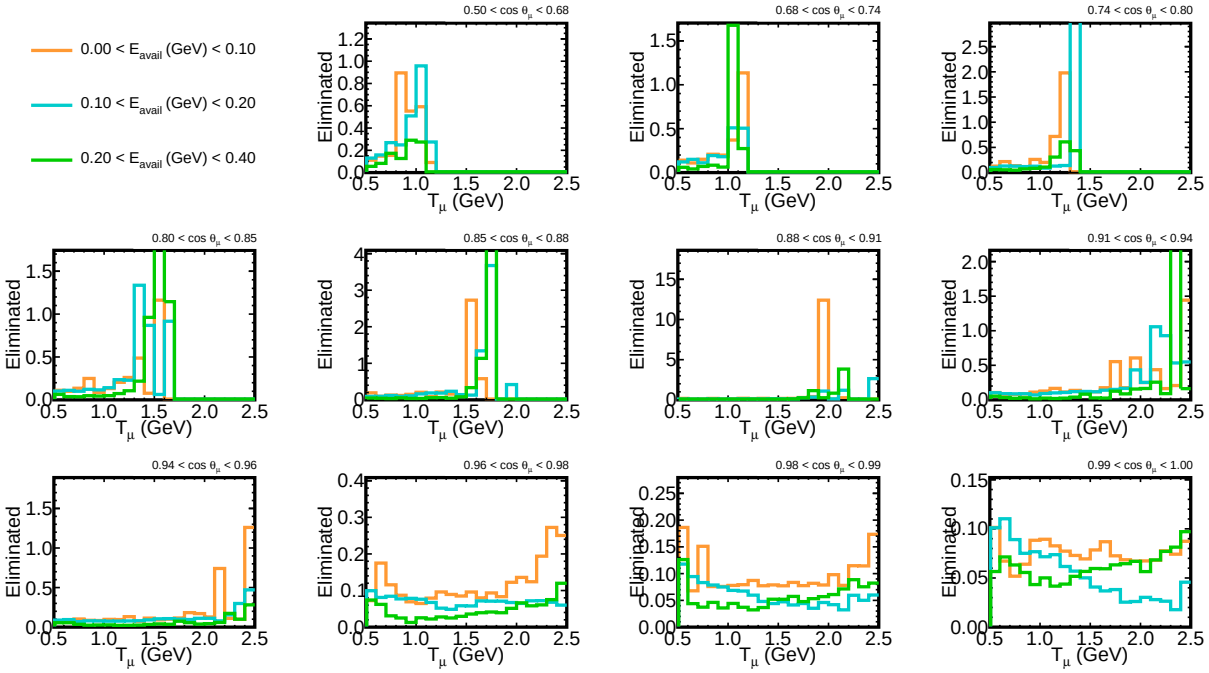

Figure 107: The fractional uncertainty introduced from the combined detector systematics.

The total fractional uncertainty contribution from the PPFX systematics can be seen in Figure 111. The average fractional uncertainty was evaluated to be 0.055. Here the average is lower than most good statistics bins, which have an uncertainty around ten percent.

The total fractional uncertainty contribution from the neutron systematic can be seen in Figure 112. The average fractional uncertainty was evaluated to be 0.14; low statistics bins raise the average from around five percent in good statistics bins.

The total fractional uncertainty contribution from the MEC Weight systematic can be seen in Figure 113. The average fractional uncertainty was evaluated to be 0.030. The effect of low statistics bins is net very low as most good statistics bins have uncertainties between two and five percent.

The total fractional uncertainty contribution from the MEC model spread systematic can be seen in Figure 114. The average fractional uncertainty was evaluated to be 0.0043. Most good statistics bins have an uncertainty between 0.002 and 0.015.

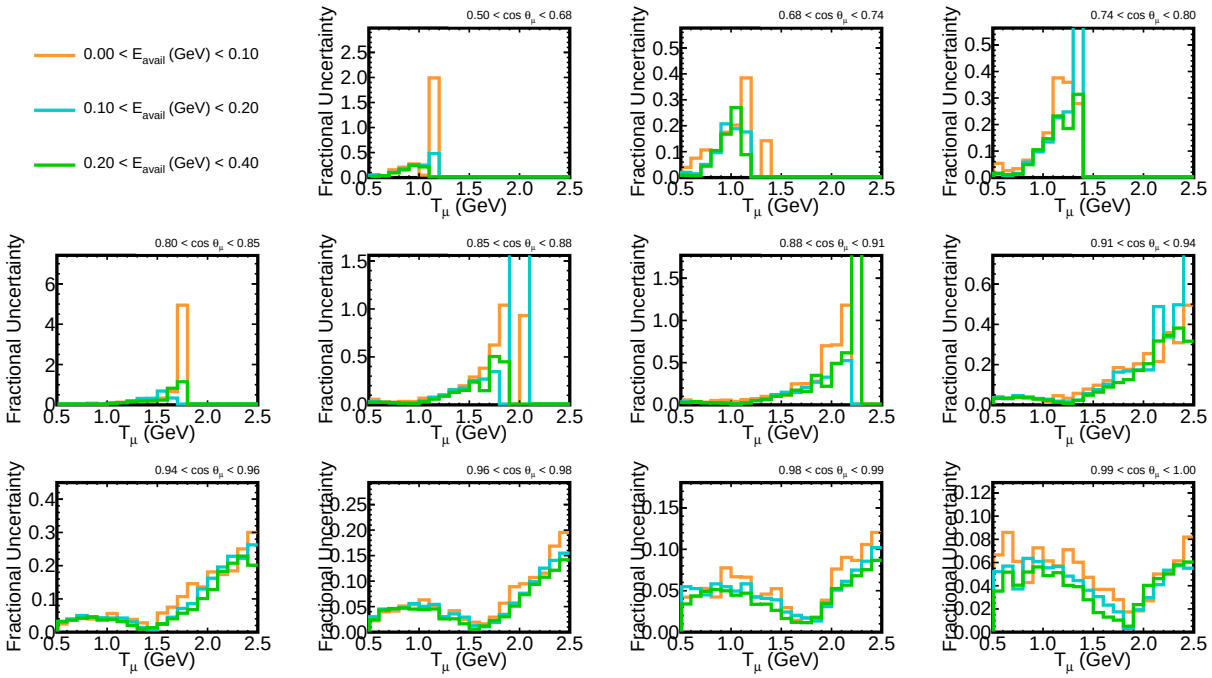

Figure 108: The fractional uncertainty between the central value cross-section and the shifted samples made from adjusting the muon kinematics.

The total fractional uncertainty can be seen in Figure 116. The average uncertainty for the total fractional uncertainty was evaluated to be 0.62. Overall the average is raised due to low statistics bins, in general most good statistics bins have an average around twenty percent.

Once the total fractional uncertainty was measured, the cross-section measured from the data with the uncertainty was plotted against the MC CV cross-section. A summary table of the average fractional uncertainty can be seen in table 9.

The final comparison is between the cross-section measured from the data plotted with the cross-section extracted from NOνA's MC. This can be seen in Figures 117, 118, and 119. It was found that the NOνA MC under-predicted the data in the 0.2-0.4 GeV bin. The 0-0.1 and 0.1-0.2 GeV E-Avail bins had general agreement between Data and NOνA predictions with one σ.

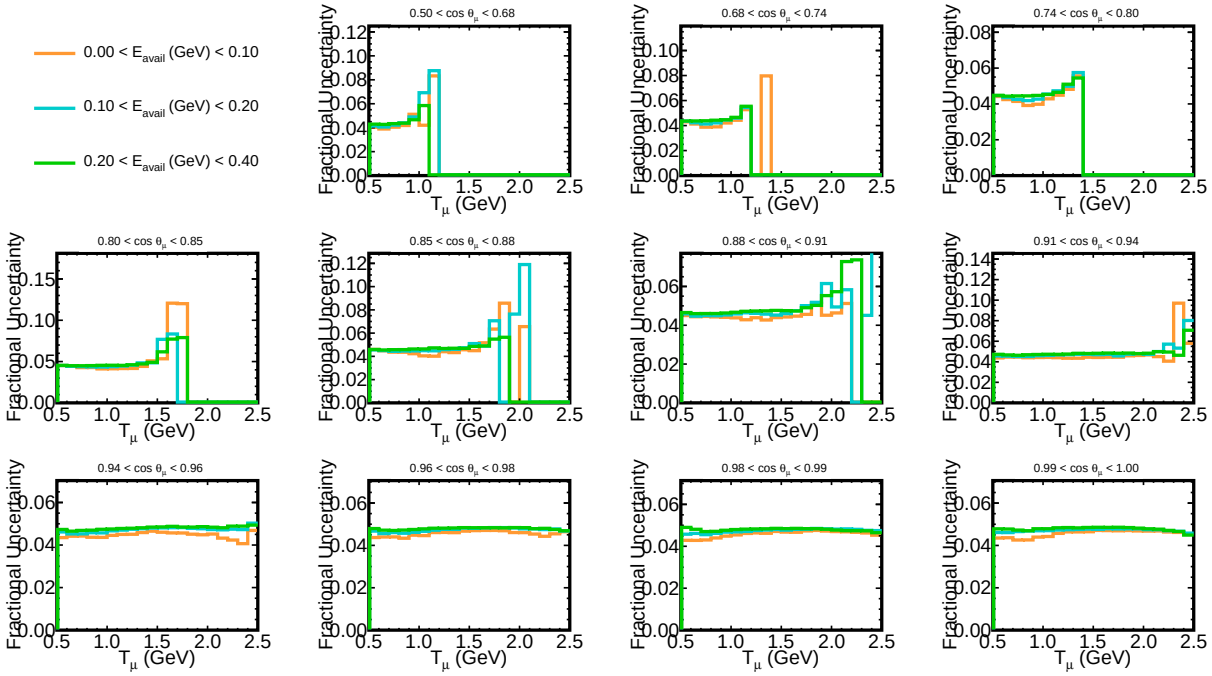

Figure 109: The fractional uncertainty introduced from the combined beam systematics

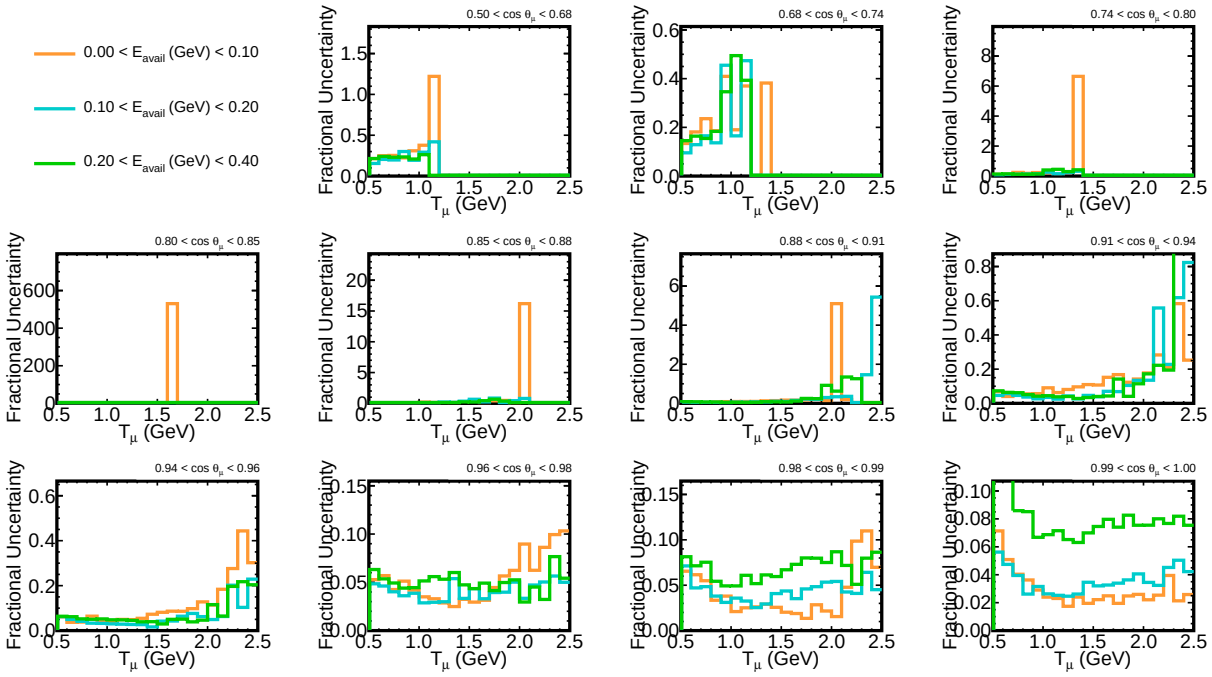

Figure 110: The fractional uncertainty between the central value cross-section and the shifted samples made from randomly fluctuating each of the parameters GENIE uses to govern neutrino interactions. This uncertainty takes uses the normalized covariance matrix over 1000 universes.

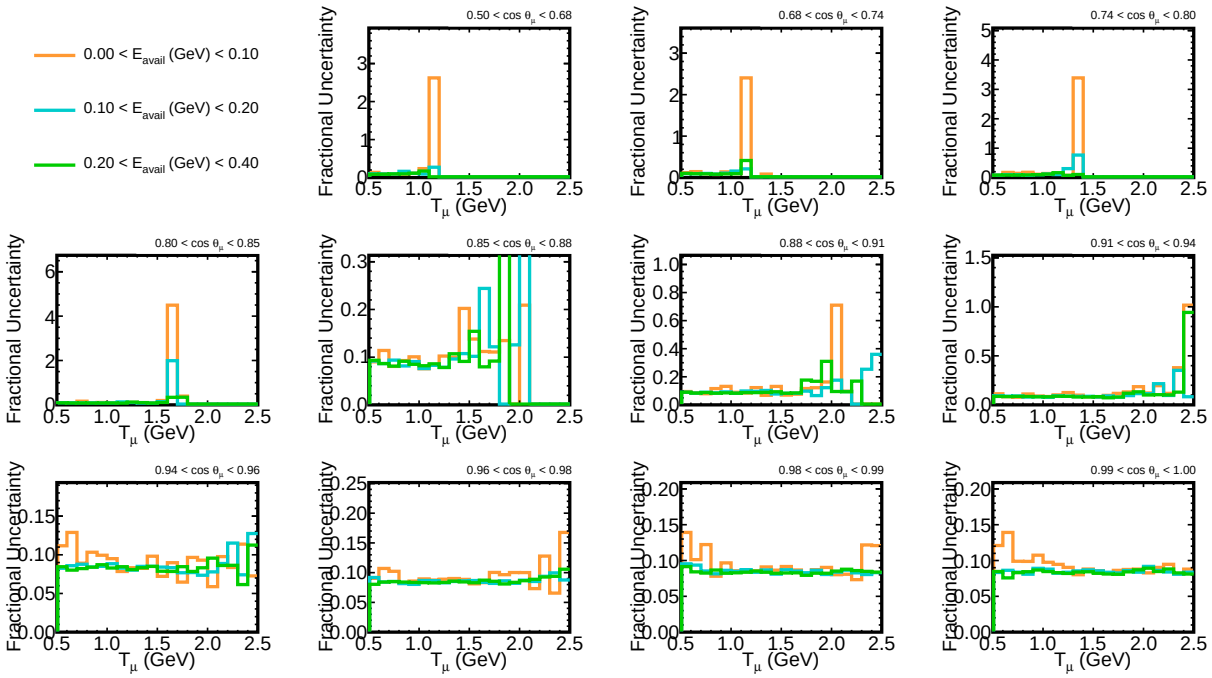

Figure 111: The fractional uncertainty between the central value cross-section and the shifted samples made from randomly fluctuating each of the parameters the PPFX package uses to govern the neutrino flux (particularly hadron production cross-sections). This uncertainty takes uses the normalized covariance matrix over 100 universes.

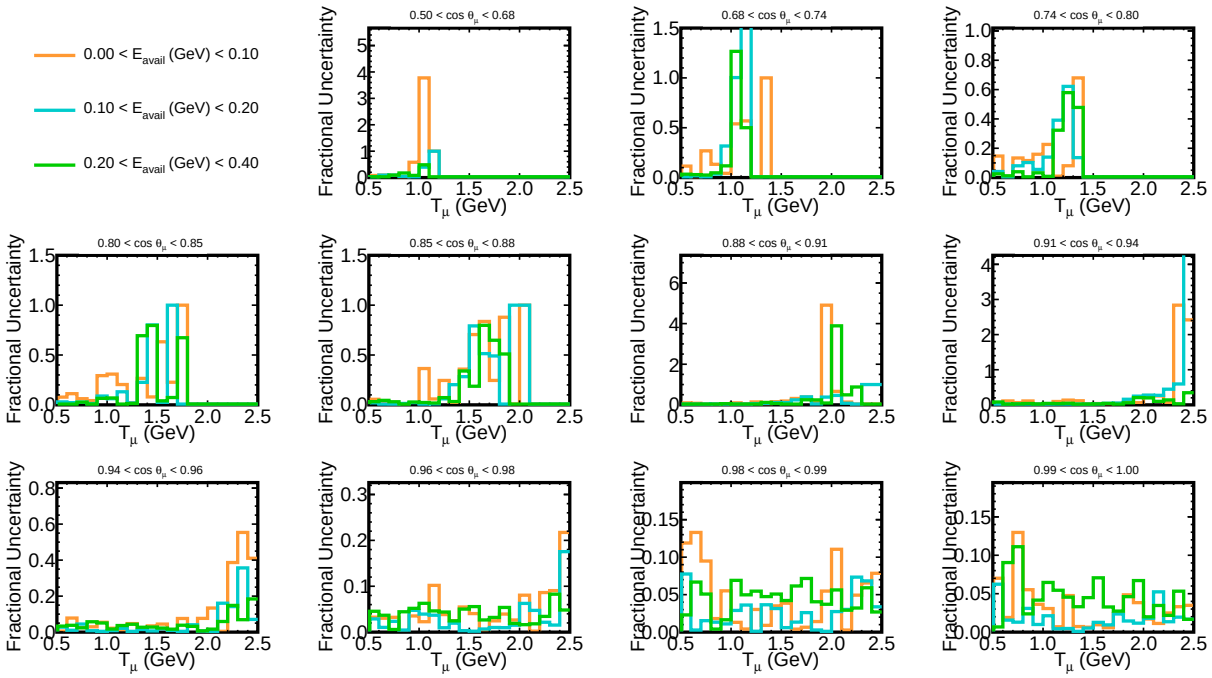

Figure 112: The fractional uncertainty between the central value cross-section and the shifted samples made from replacing the GEANT4 neutron interaction model with the MENATE model.

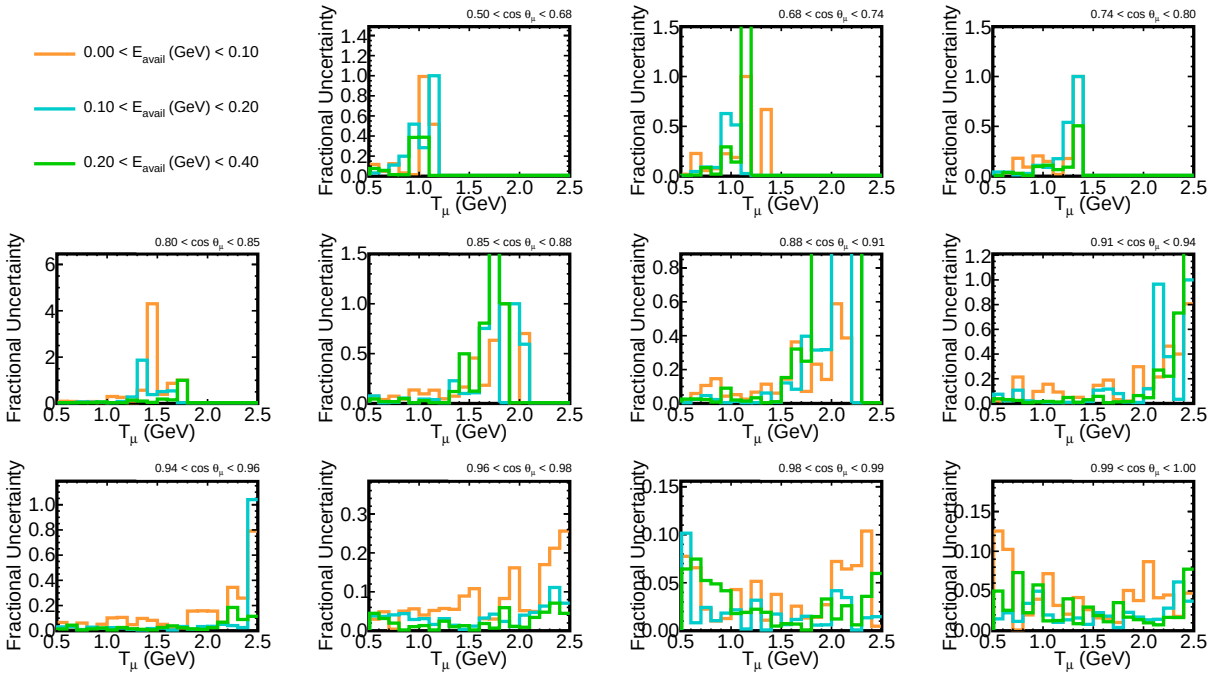

Figure 113: The fractional uncertainty between the central value cross-section and the shifted samples made capping the value of the MEC Weight at fifty.

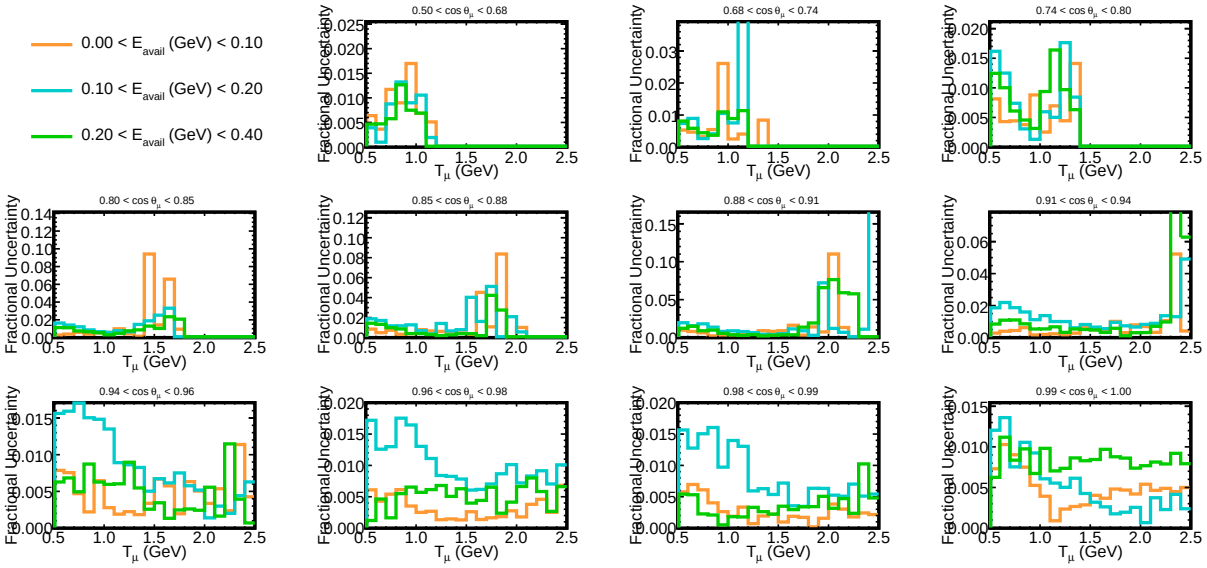

Figure 114: The fractional uncertainty between the central value cross-section and the shifted samples made generating 1000 universes with a random combination of Valencia, SuSA and Dytman MEC models.

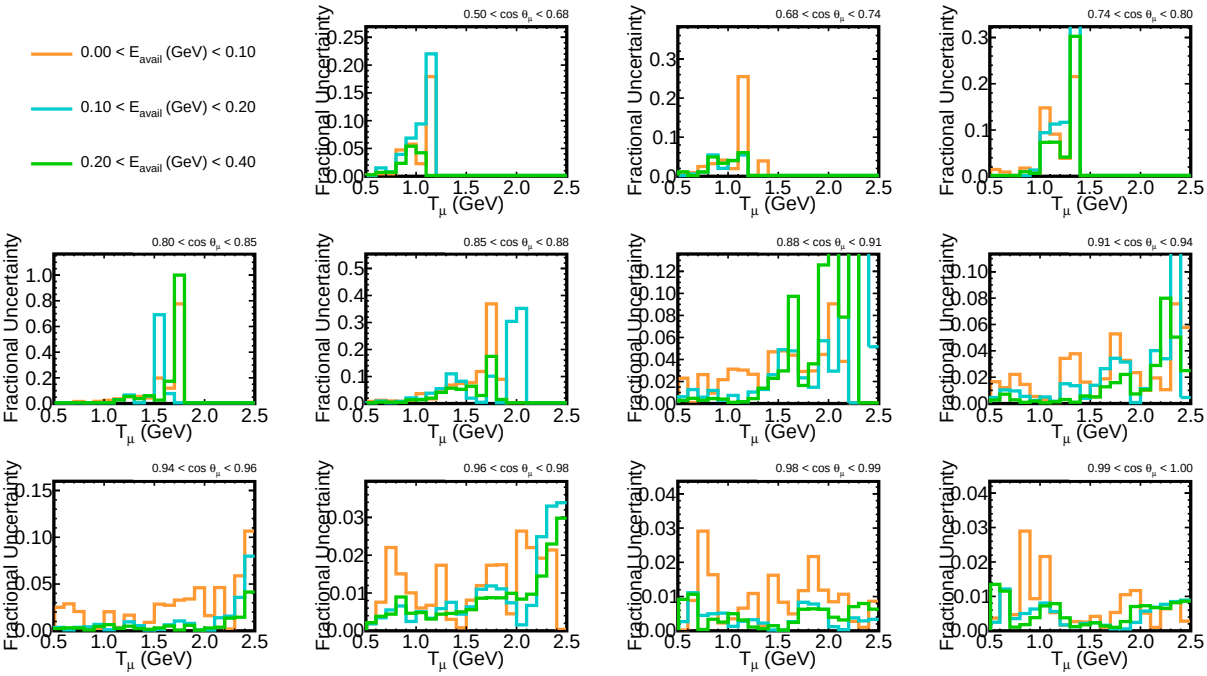

Figure 115: The fractional uncertainty between the central value cross-section and the shifted samples made from randomly fluctuating the fake data 3000 times using a Poisson distribution.

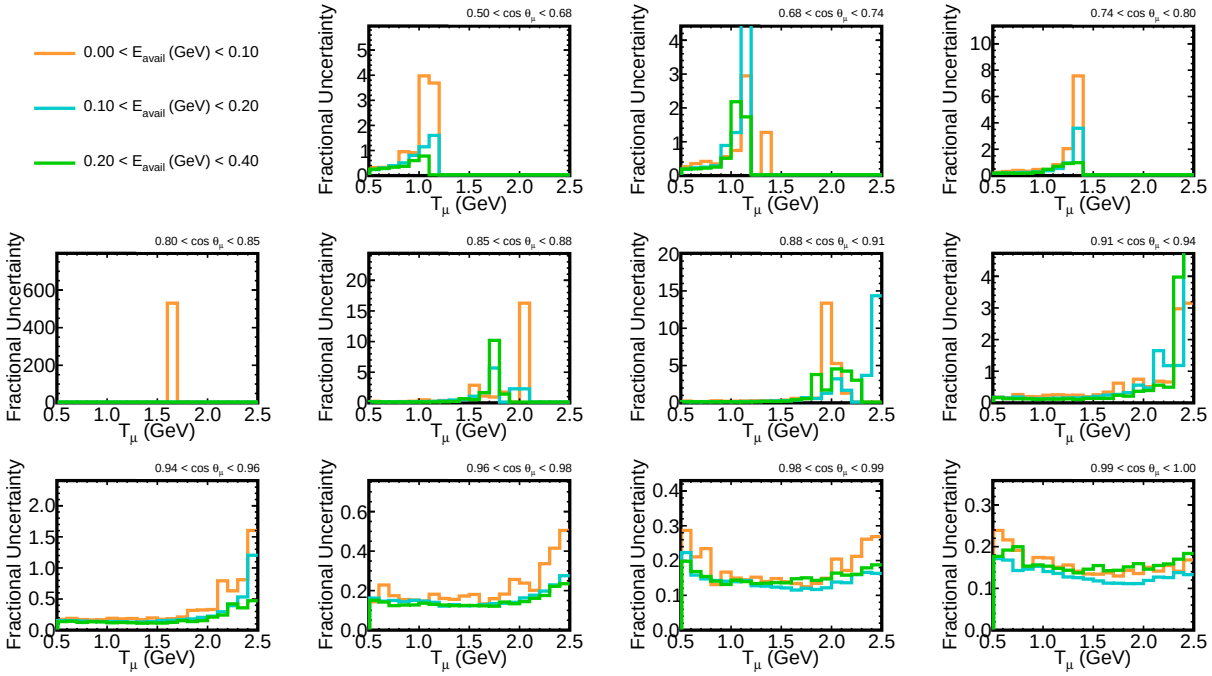

Figure 116: The total fractional uncertainty on the central value cross-section due to all sources of Uncertainty.

Table 10: Average fractional uncertainty from each source of uncertainty on the cross-section from the real data central value.

Source	Contribution
Detector	0.47
Muon Kinematics	0.12
Beam	0.064
GENIE	0.39
PPFX	0.055
Neutron	0.14
MEC Weight	0.030
MEC Model	0.0043
Statistical	0.014
Total	0.62

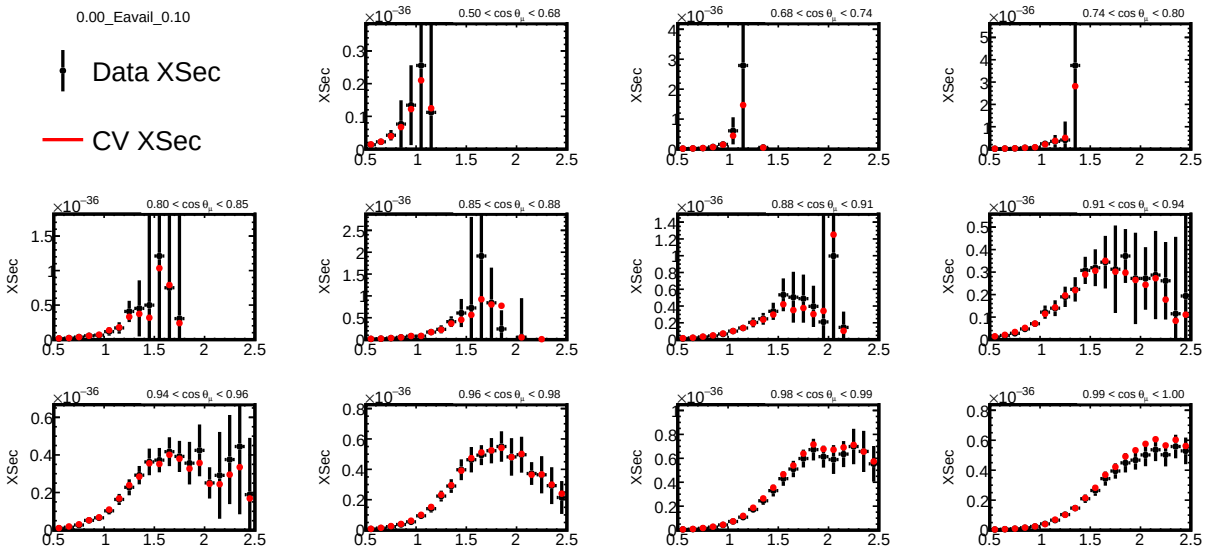

Figure 117: The measured central value cross-section with the total uncertainty applied, comparing the data to NOνA's MC. Shown is the first E-Avail bin

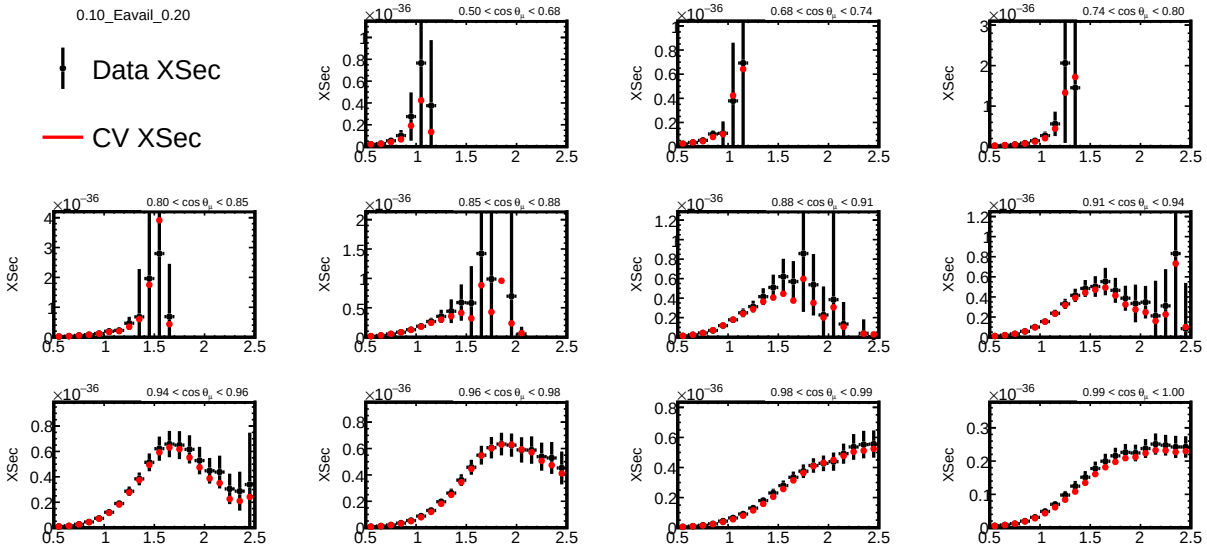

Figure 118: The measured central value cross-section with the total uncertainty applied, comparing the data to NOνA's MC. Shown is the second E-Avail bin

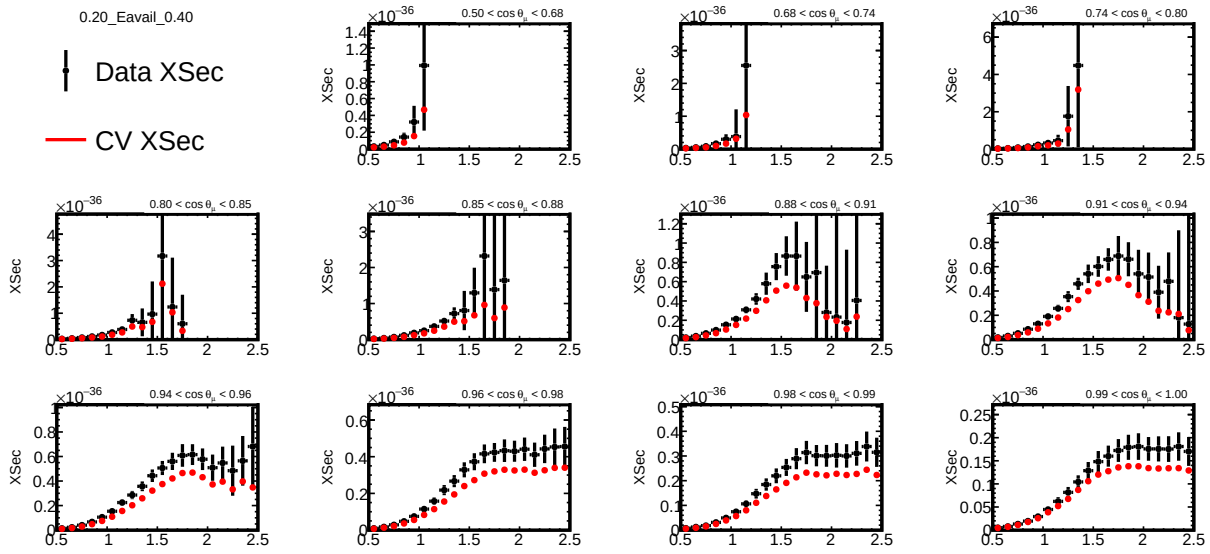

Figure 119: The measured central value cross-section with the total uncertainty applied, comparing the data to NOνA's MC. Shown is the third E-Avail bin

12 Conclusions

This analysis measured the triple-differential cross-section of the muon neutrino charged current interaction in the regime of low hadronic activity. The analysis found that the NOνA predictions under-predicted the data in the 0.2-0.4 GeV E-Avail bin, especially for events with forward going muons, as can be seen in Figures 117, 118, and 119.

Figures 120, 121, and 122 show the data plotted against the predictions of other 2p2h models in addition to NOνA's central-value tune. It shows that NOνA's predictions are better than these models individually in the 0-0.1 GeV E-Avail bin. The SuSA model does as well as the NOνA predictions in many of the $\cos\theta_\mu$ bins in the 0.1-0.2 GeV E-Avail bin, and does a better job than it in some of the $\cos\theta_\mu$ in the 0.2-0.4 GeV E-Avail bin. However the SuSA model ends up over-predicting the data in the $0.99 < \cos\theta_\mu < 1.00$ bin for both the 0.1-0.2 and 0.2-0.4 GeV E-Avail bins.

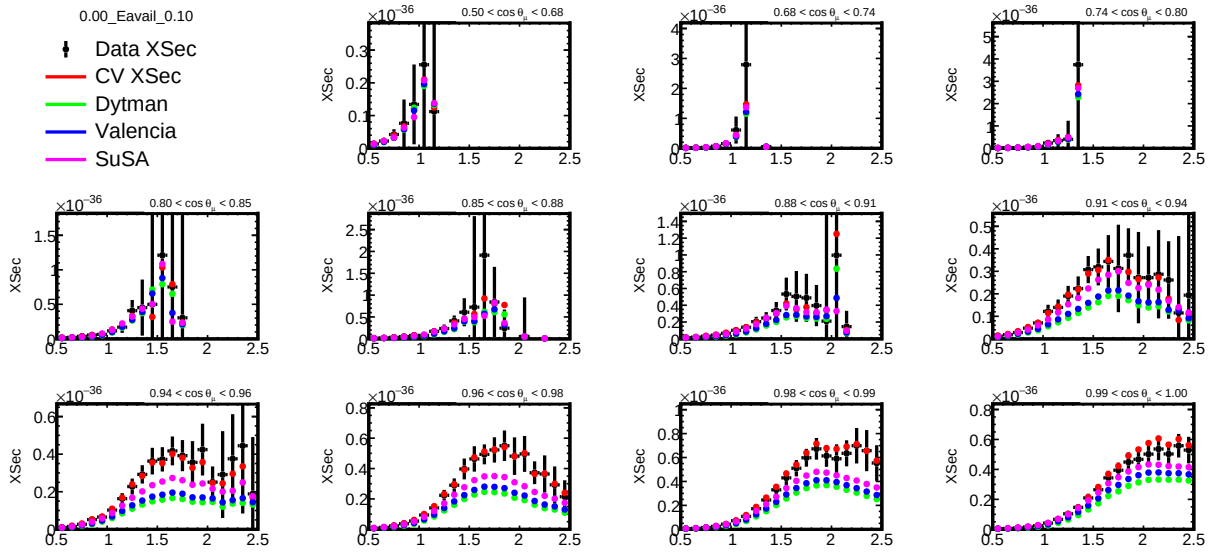

Figure 120: Measured cross-section of the $\nu_\mu CC$ with low hadronic activity, compared with predictions of different 2p2h models

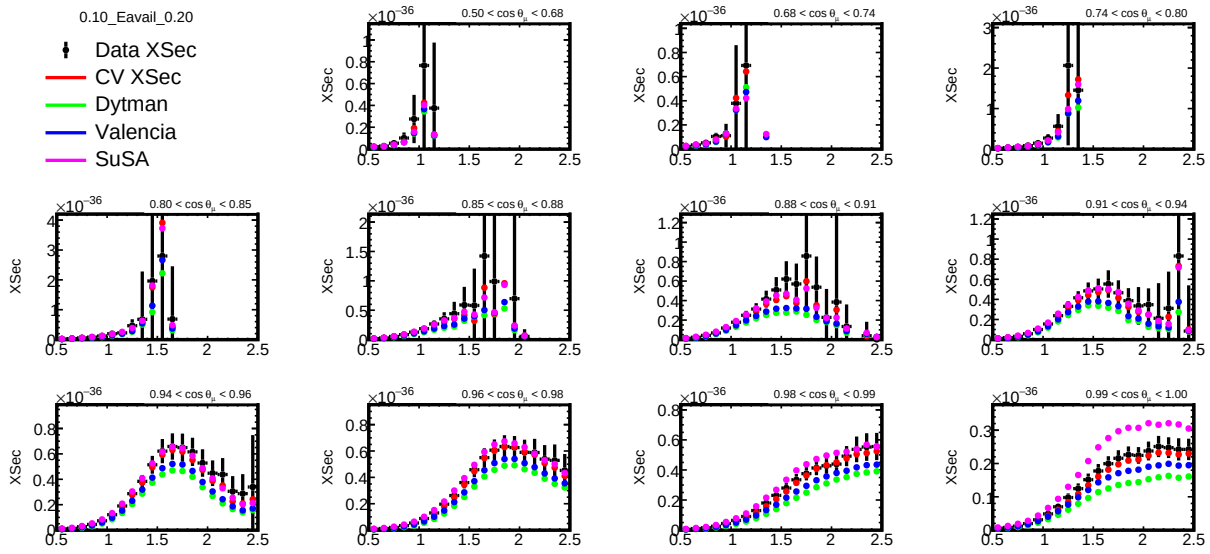

Figure 121: Measured cross-section of the $\nu_\mu CC$ with low hadronic activity, compared with predictions of different 2p2h models

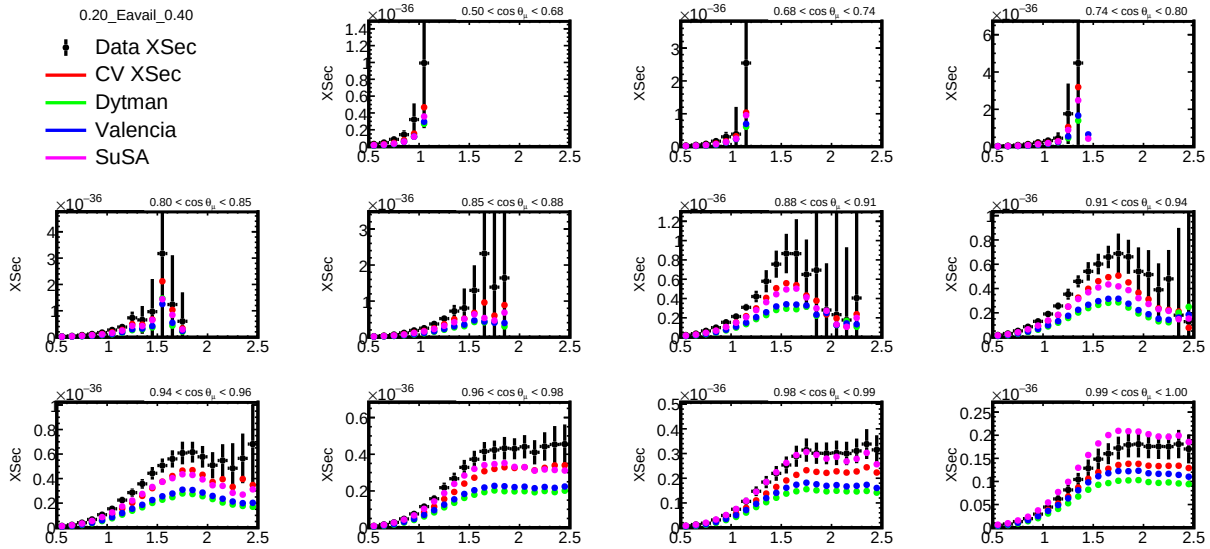

Figure 122: Measured cross-section of the $\nu_\mu CC$ with low hadronic activity, compared with predictions of different 2p2h models

Previously, NOνA found that in the forward going regions there was a disagreement between theory and data [5]. This analysis extended the previous analysis from a two-dimensional analysis to a three-dimensional one. This analysis found that the disagreement was concentrated in the 0.2

- 0.4 GeV region of E-Avail. This disagreement takes the form of a deficit in the cross-section of the NOνA predictions. There is agreement between this analysis and the previous analysis that Valencia [50] under-predicts the data, particularly in the most forward going muon events. However, they also saw the same effect with the SuSA model [49], while in the most forward going muon events in this analysis, the SuSA model over-predicts the data in the higher two E-Avail bins.

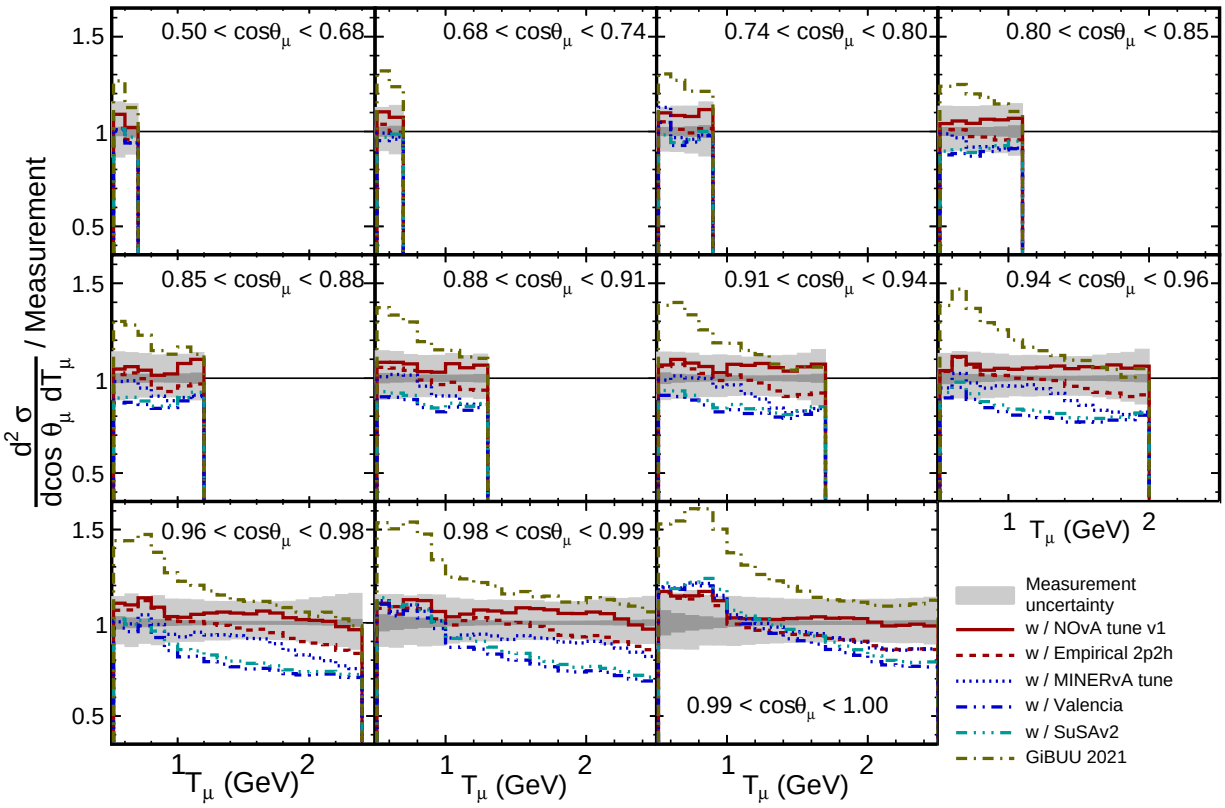

Figure 123: Measured cross-section of the $\nu_\mu CC$ with low hadronic activity, from an earlier NOνA analysis. The measured cross-section is compared with NOνA predictions and predictions from other MEC models [5]

A different NOνA analysis did a $\nu_\mu CC$ inclusive analysis in bins of $|q|$ and available energy [51]. That analysis found that in the region of 0-0.4 GeV range, the Valencia and SuSA models under-predict the cross-section of the $\nu_\mu CC$ interaction, with the data generally agreeing with the NOνA tune, as can be seen in Figure 124. They found that the SuSA model did agree with data predictions in the 0.35-0.50 GeV E-Avail bin. This is in line with the idea that SuSA predicts

more relative to the data in that range of E-Avail, however it doesn't show the same effect of SuSA over-predicting in the forward going muons in that range of E-Avail that this analysis did. Figure 125 shows the double-differential cross-section of the inclusive analysis in bins of E-Avail and slices of $|q|$. This analysis generally agrees with the inclusive analysis on the under-prediction of Valencia.

The MINERvA experiment did a measurement of the inclusive charged-current ν_μ cross-section with low three-momentum transfer ($q_3 < 1.2$ GeV) [52], a related measurement to this analysis. Figure 126 shows the double-differential cross-section in bins of E-Avail and q_3, compared to MINERvA's predictions as well as the predictions of NuWro and GENIE event generators. The GENIE 3 predictions used uses a local Fermi gas (LFG) and the Valencia model for both QE with RPA and 2p2h interactions [52]. Their results also show disagreement between the GENIE predictions and their data, including in the regions of 0.2-0.4 GeV E-Avail in the region of $q_3 < 0.90$ GeV. This shows agreement between MINERvA and this analysis.

The T2K experiment did a measurement of the $\nu_\mu CC$ double-differential cross-section at the on-axis INGRID and off-axis ND280 detectors, in bins of muon kinematics, with the condition that there were zero pions in the final state [53]. This is a different, but related measurement to the low hadronic activity regime, as the choices in selection lead to a reduction in pions in the final-state.

The cross-section measurements for ND280 can be seen in Figures 127 and 128, while the measurements for INGRID can be see in 129. These figures show discrepancies between their data and the predictions of the event generators, for both the ND280 and INGRID detectors. Both this analysis and the T2K analysis agree in that models struggle to predict the data.

Another related measurement was done by the MicroBooNE collaboration. The MicroBooNE collaboration measured the double-differential cross-section of the $\nu_\mu CC$ interaction on argon of quasielastic-like events [54]. They looked for events with a final state muon $0.1 < p_\mu < 1.2$ GeV/c and exactly one proton with $0.3 < p_p < 1$ GeV/c, while any events with neutral pions in the final state are excluded. MicroBooNE also found discrepancy between their data and MC predictions. Their measured flux-integrated double-differential cross-sections can be seen in Figure 130. The version of GENIE used in their analysis (marked as G18) used the SuSA model for MEC events. The

SuSA model ended up over-predicting the data in the region of 0.3-0.6 GeV/c missing transverse momentum (δp_T). MicroBooNE generally agrees with this analysis that there are certain regions where SuSA will over-predict data in events with forward going muons.

This analysis represents another step forward in understanding the $\nu_\mu CC$ interaction and models of the 2p2h interaction.

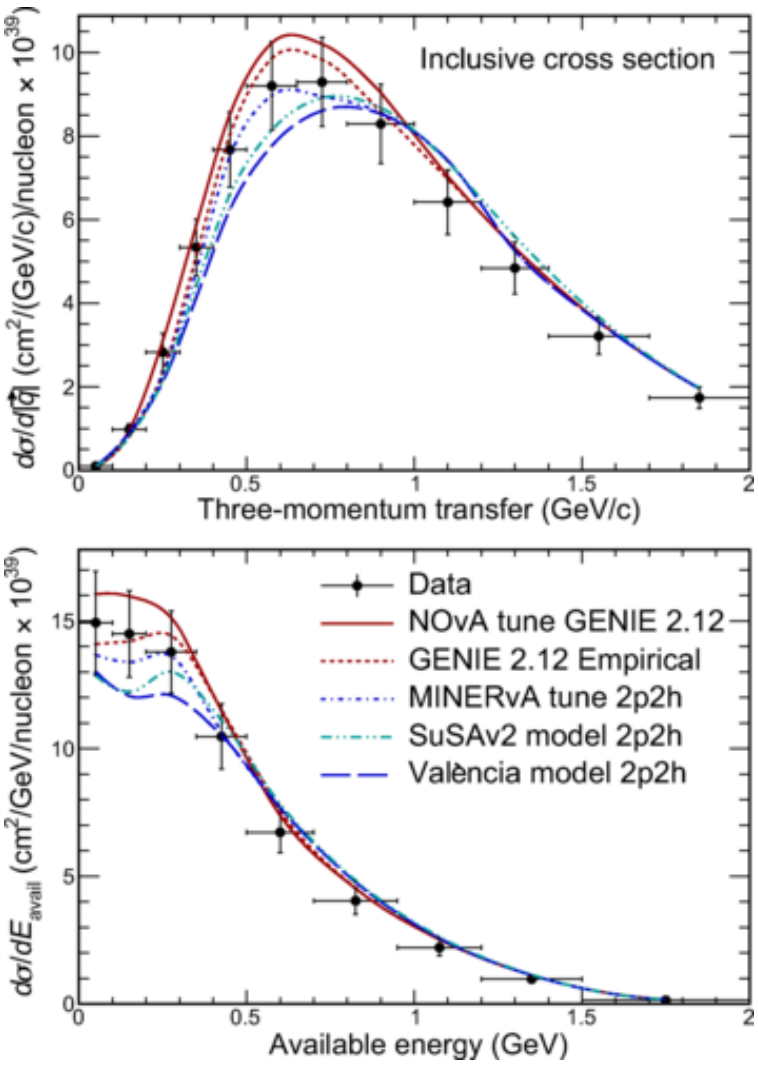

Figure 124: Measured $\nu_\mu CC$ inclusive cross-section in bins of $|q|$ (top) and E-Avail (bottom), from an earlier NOνA analysis [51]. The measured cross-section is compared with MC predictions for different models of 2p2h.

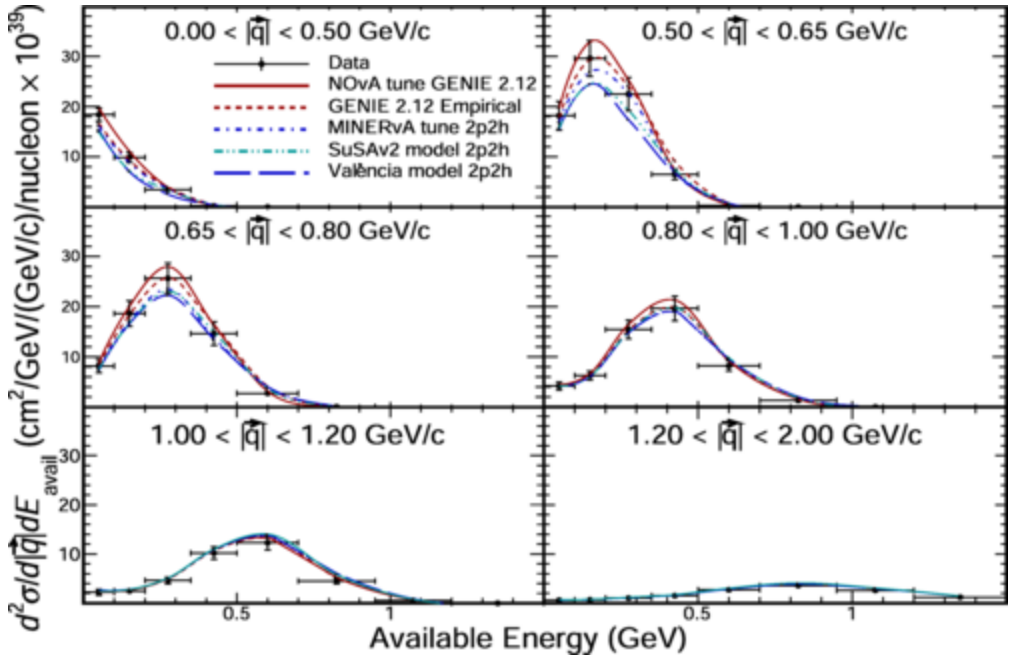

Figure 125: Measured $\nu_\mu CC$ inclusive cross-section in bins of E-Avail in six slices of $|q|$, from an earlier NOνA analysis [51]. The measured cross-section is compared with MC predictions for different models of 2p2h.

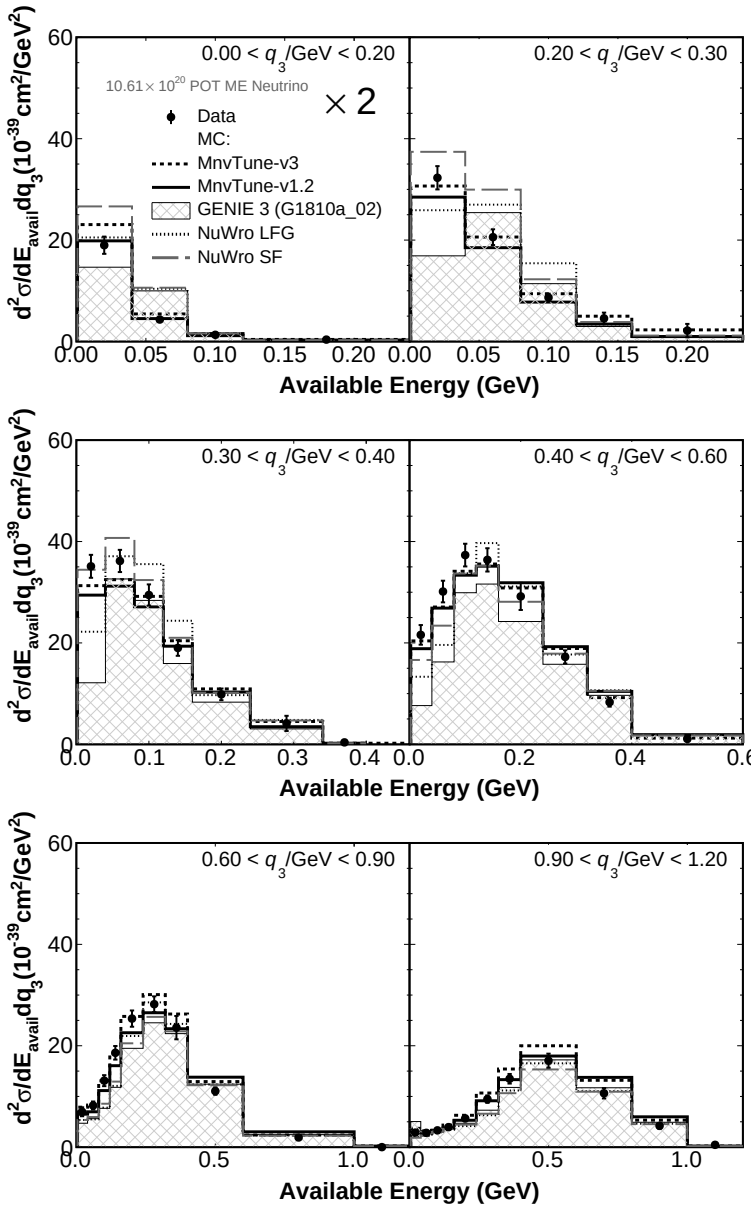

Figure 126: Measured double-differential cross-section in bins of E-Avail and six bins of three-momentum transfer, from the MINERvA experiment [52]. Data is compared to MNVTUNE3 (black dashed line), MVNTUNE1.2 (black solid line), NuWro structure function (gray solid line), NuWro local Fermi gas (dotted gray line), and GENIE3 (gray grid filled histogram). The first q_3 panel is scaled by a factor of two.

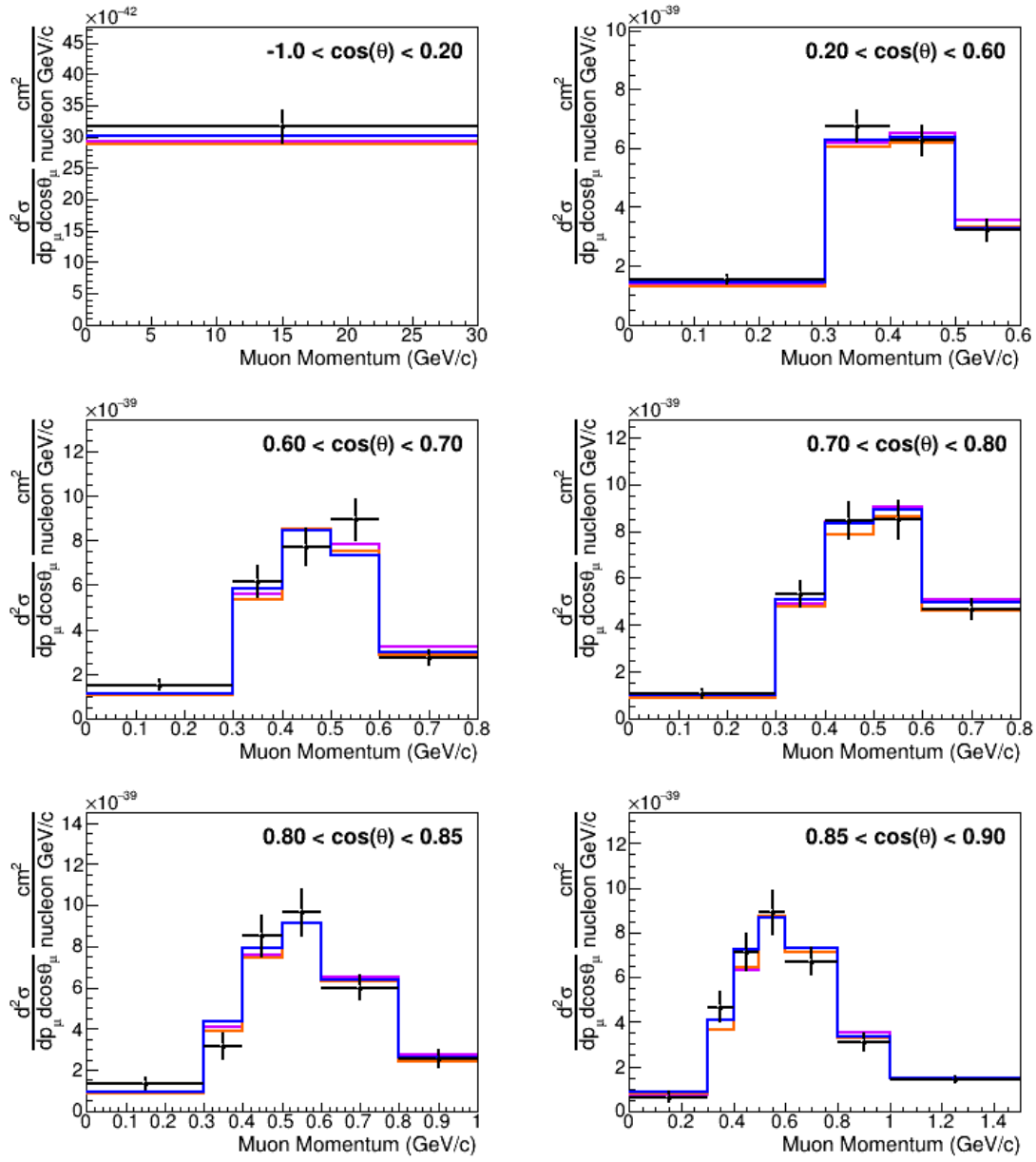

Figure 127: Measured cross-section in the ND280 detector of the T2K experiment as a function of muon momentum in bins of muon angle compared to NEUT, GENIE and NuWro event generator predictions using similar models [53].

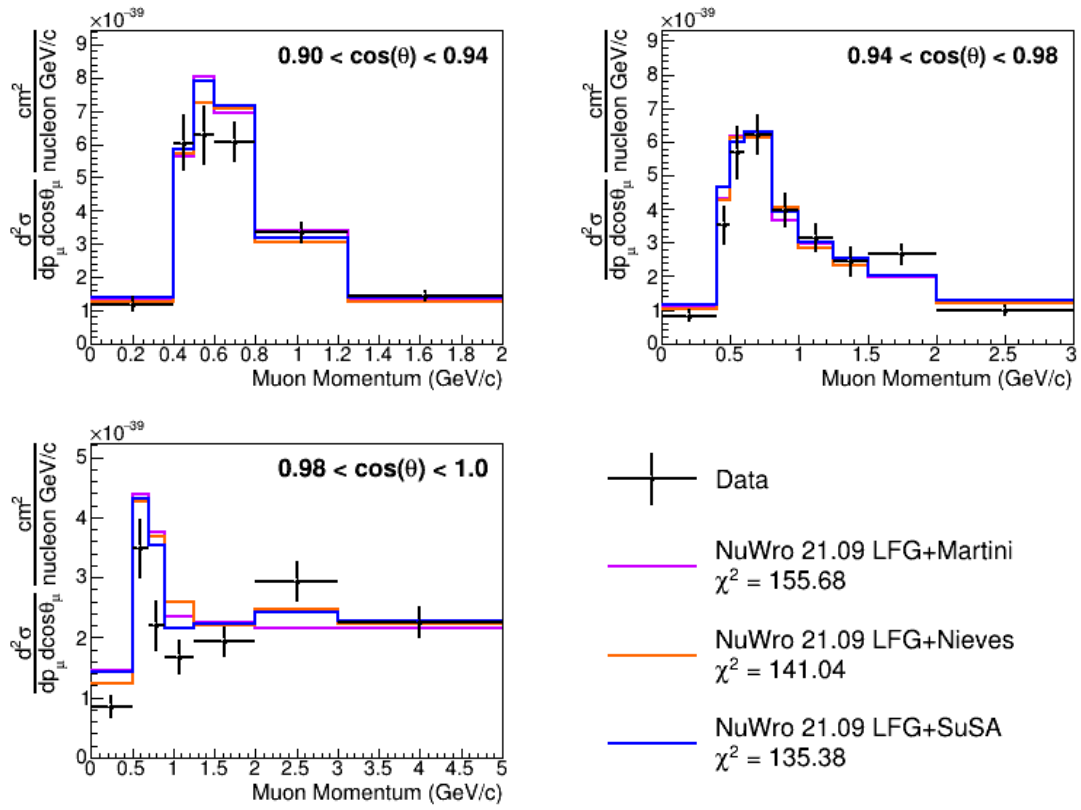

Figure 128: Measured cross-section in the ND280 detector of the T2K experiment as a function of muon momentum in bins of muon angle compared to NEUT, GENIE and NuWro event generator predictions using similar models [53].

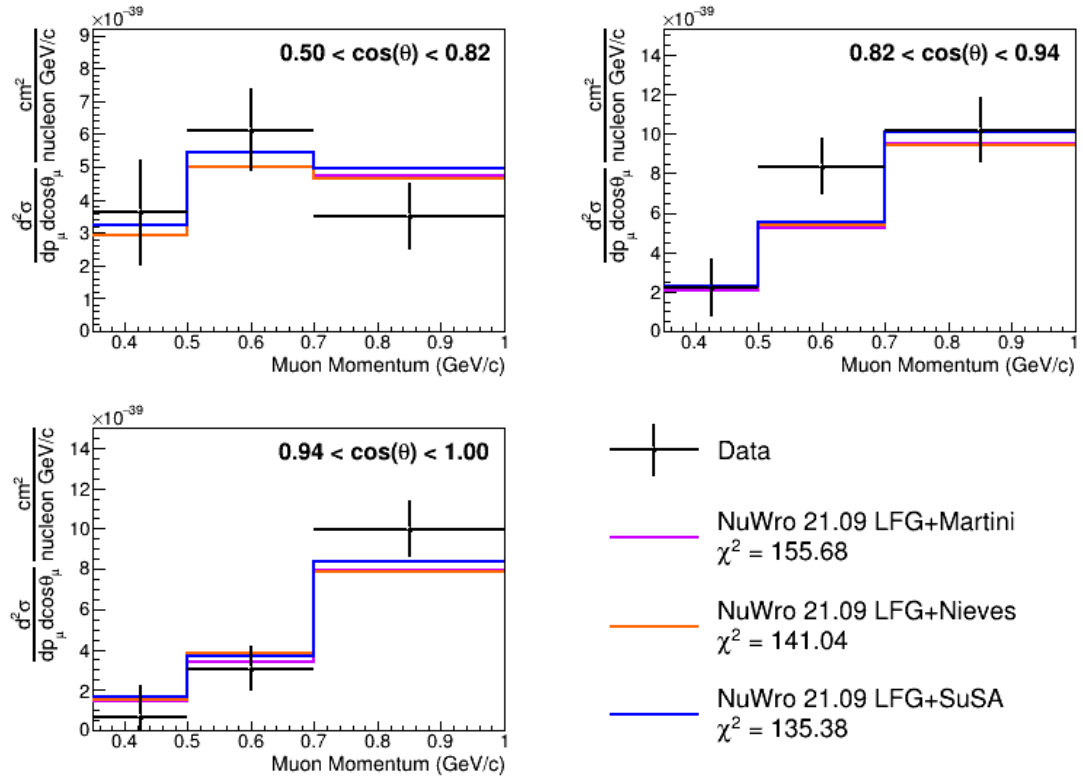

Figure 129: Measured cross-section in the INGRID detector of the T2K experiment as a function of muon momentum in bins of muon angle compared to NEUT, GENIE and NuWro event generator predictions using similar models [53].

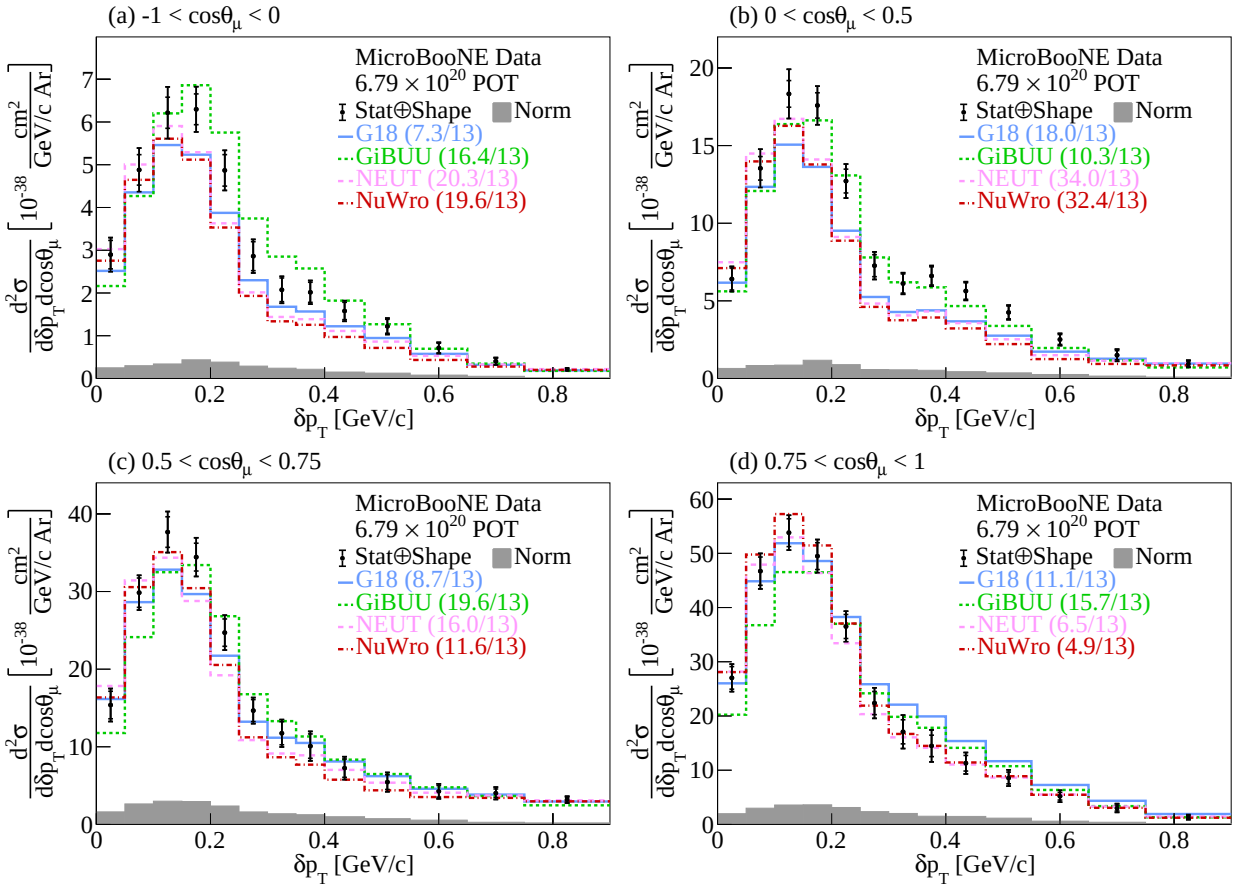

Figure 130: The flux-integrated double-differential cross-sections as a function of δp_T in $\cos\theta_\mu$ bins. MicroBooNE data is plotted against the predictions of multiple event generators.

Bibliography

[1] David J. Griffiths. *INTRODUCTION TO ELEMENTARY PARTICLES*. John Wiley & Sons, 1987.

[2] B. Povh et al. *Particles and nuclei: An introduction to the physical conceptions.* Springer-Verlag Berlin Heidelberg, 1993.

[3] R. L. Workman et al. "Review of Particle Physics". In: *PTEP* 2022 (2022), p. 083C01.

[4] J. A. Formaggio and G. P. Zeller. "From eV to EeV: Neutrino Cross Sections Across Energy Scales". In: *Rev. Mod. Phys.* 84 (2012), pp. 1307–1341. arXiv: 1305.7513 [hep-ex].

[5] M. A. Acero et al. "Measurement of the double-differential cross section of muon-neutrino charged-current interactions with low hadronic energy in the NOvA Near Detector". In: (Oct. 2024). arXiv: 2410.10222 [hep-ex].

[6] W. M. Alberico, Magda Ericson, and A. Molinari. "The Role of Two Particles - Two Holes Excitations in the Spin - Isospin Nuclear Response". In: *Annals Phys.* 154 (1984), p. 356.

[7] M. A. Acero et al. "Adjusting neutrino interaction models and evaluating uncertainties using NOvA near detector data". In: *Eur. Phys. J. C* 80.12 (2020), p. 1119. arXiv: 2006.08727 [hep-ex].

[8] Giampaolo Co'. "Random phase approximation and neutrino-nucleus cross sections". In: *Acta Phys. Polon. B* 37 (2006). Ed. by K. M. Graczyk and J. T. Sobczyk, pp. 2235–2242. arXiv: nucl-th/0605051.

[9] Richard Gran. "Model Uncertainties for Valencia RPA Effect for MINERvA". In: (May 2017). arXiv: 1705.02932 [hep-ex].

[10] L. Alvarez-Ruso et al. "NuSTEC White Paper: Status and challenges of neutrino–nucleus scattering". In: *Prog. Part. Nucl. Phys.* 100 (2018), pp. 1–68. arXiv: 1706.03621 [hep-ph].

[11] Omar Benhar et al. "Neutrino–nucleus interactions and the determination of oscillation parameters". In: *Phys. Rept.* 700 (2017), pp. 1–47. arXiv: 1501.06448 [nucl-th].

[12] Cathal Sweeney. "Measurement of the muon neutrino charged-current single charged pion production cross-section in the NOvA Near Detector". PhD thesis. University College London, University Coll. London, University Coll. London, 2023.

[13] D. S. Ayres et al. "The NOvA Technical Design Report". In: (Oct. 2007).

[14] P. Adamson et al. "The NuMI Neutrino Beam". In: *Nucl. Instrum. Meth. A* 806 (2016), pp. 279–306. arXiv: 1507.06690 [physics.acc-ph].

[15] S. Gariazzo et al. "Neutrino masses and their ordering: Global Data, Priors and Models". In: *JCAP* 03 (2018), p. 011. arXiv: 1801.04946 [hep-ph].

[16] A Ferrari et al. *FLUKA*. CERN Yellow Reports: Monographs. Geneva: CERN, 2005. URL: cds.cern.ch/record/898301.

[17] M. Campanella et al. "First Calorimeter Simulation with the FLUGG Prototype". In: (Dec. 1999).

[18] A. Aurisano et al. "The NOvA simulation chain". In: *J. Phys. Conf. Ser.* 664.7 (2015), p. 072002.

[19] C. Andreopoulos et al. "The GENIE Neutrino Monte Carlo Generator". In: *Nucl. Instrum. Meth. A* 614 (2010), pp. 87–104. arXiv: 0905.2517 [hep-ph].

[20] K. Bays et al. "NOvA 2020 cross-section tune tech note". located on private NOvA server. 2020. URL: nova-docdb.fnal.gov/cgi-bin/private/RetrieveFile?docid=43962&filename=2020_xsec_tech_note%20%281%29.pdf&version=3.

[21] A. Bodek and U. K. Yang. "Modeling neutrino and electron scattering inelastic cross- sections in the few GeV region with effective LO PDFs TV Leading Order". In: *2nd International Workshop on Neutrino-Nucleus Interactions in the Few GeV Region*. Aug. 2003. arXiv: hep-ex/0308007.

[22] E. Catano-Mur et al. "NOvA Production 5.1 Detector Systematics Executive Summary". located on private NOvA server. 2022. URL: nova-docdb.fnal.gov/cgi-bin/private/RetrieveFile?docid=53225&filename=Prod5_1_Detector_Systematics_Executive_Summary-5.pdf&version=5.

[23] M. Baird et al. "Event Reconstruction Techniques in NOvA". In: *J. Phys. Conf. Ser.* 664.7 (2015), p. 072035.

[24] K. Bays et al. "NOvA Cross Section Modeling Technote for Production 5.1". located on private NOvA server. 2024. URL: nova-docdb.fnal.gov/cgi-bin/private/RetrieveFile?docid=61559&filename=NOvA_Cross_Section_Modeling_Technote_For_Production_5_1_v5.pdf&version=8.

[25] D. Mendez. "Second Analysis Calorimetric Energy Scale Calibration of the NOvA detectors". located on private NOvA servers. 2016. URL: nova-docdb.fnal.gov/cgi-bin/private/RetrieveFile?docid=13579&filename=calib_technoteSA.pdf&version=35.

[26] A. Lister. "Calibration: A One Page Summary". located on private NOvA server. 2025. URL: nova-docdb.fnal.gov/cgi-bin/private/RetrieveFile?docid=65198&filename=NOvA_calibration_onepage.pdf&version=1.

[27] W. R. Leo. *Techniques for Nuclear and Particle Physics Experiments: A How to Approach*. Springer-Verlag Berlin Heidelberg, 1987.

[28] L. Aliaga. "Analysis of the NuMu CC with low hadronic activity events in the NOvA near detector". located on private NOvA server. 2023. URL: nova-docdb.fnal.gov/cgi-bin/private/RetrieveFile?docid=49881&filename=NuMuCC_LowHad_v4.pdf&version=4.

[29] J. Hartnell and G. Pawloski. "Summary of the 2016 (Second Analysis) numu Disappearance Analysis". located on private NOvA server. 2016. URL: nova-docdb.fnal.gov/cgi-bin/private/RetrieveFile?docid=15232&filename=numuAnalysis2016.pdf&version=1.

[30] V. Bychkov. "Near Detector Data/MC Comparison". located on private NOvA server. 2016. URL: nova-docdb.fnal.gov/cgi-bin/sso/RetrieveFile?docid=15352&filename=ND%20DataMC%20Comparisons.pdf&version=1.

[31] M. A. Acero et al. "Measurement of the double-differential muon-neutrino charged-current inclusive cross section in the NOvA near detector". In: *Phys. Rev. D* 107.5 (2023), p. 052011. arXiv: 2109.12220 [hep-ex].

[32] N. Raddatz. "KalmanTrack Technical Note". located on private NOvA server. 2015. URL: nova-docdb.fnal.gov/cgi-bin/private/RetrieveFile?docid=13545&filename=technote.pdf&version=1.

[33] L. Aliaga et al. "Measurement of the NuMuCC inclusive cross section in the NOvA near detector". located on private NOvA server. 2019. URL: nova-docdb.fnal.gov/cgi-bin/private/RetrieveFile?docid=53925&filename=Measurement_of_the_Muon_Anti_Neutrino_Charged_Current_Inclusive_Cross_Section_in_the_NOvA_Near_Detector_v4.pdf&version=11.

[34] P. A. Rodrigues et al. "Identification of nuclear effects in neutrino-carbon interactions at low three-momentum transfer". In: *Phys. Rev. Lett.* 116 (2016). [Addendum: Phys.Rev.Lett. 121, 209902 (2018)], p. 071802. arXiv: 1511.05944 [hep-ex].

[35] Travis Grant Olson. "Measurement of $d^2\sigma/d|\vec{q}|dE_{avail}$ and 2p2h contribution using charged current ν_μ interactions in the NOvA Near Detector". PhD thesis. Tufts U., Tufts U., 2021.

[36] G. D'Agostini. "A multidimensional unfolding method based on Bayes' theorem". In: *Nuclear Instruments and Methods in Physics Research Section A: Accelerators, Spectrometers, Detectors and Associated Equipment* 362.2 (1995), pp. 487–498. URL: www.sciencedirect.com/science/article/pii/016890029500274X.

[37] L. Aliaga et al. "NuMI flux systematic uncertainties for the NOvA1 third analyses". located on private NOvA server. 2017. URL: nova-docdb.fnal.gov/cgi-bin/private/RetrieveFile?docid=17608&filename=BeamSystTN_2017Jul27.pdf&version=5.

[38] L. Aliaga and P. Snopok. "New NuMI Target Systematics". located on private NOvA server. 2019. URL: nova-docdb.fnal.gov/cgi-bin/private/RetrieveFile?docid=41931&filename=new_target_systematics.pdf&version=1.

[39] S. Lin. "GENIE Systematic Uncertainties with the Multi-universe Approach in CAFAna". located on private NOvA server. 2017. URL: nova-docdb.fnal.gov/cgi-bin/private/RetrieveFile?docid=21635&filename=genie_multiverse_cafana_class.pdf&version=2.

[40] Costas Andreopoulos et al. "The GENIE Neutrino Monte Carlo Generator: Physics and User Manual". In: (Oct. 2015). arXiv: 1510.05494 [hep-ph].

[41] A. Bodek and U. K. Yang. "Modeling neutrino and electron scattering inelastic cross- sections in the few GeV region with effective LO PDFs TV Leading Order". In: *2nd International Workshop on Neutrino-Nucleus Interactions in the Few GeV Region*. Aug. 2003. arXiv: hep-ex/0308007.

[42] K. Bays et al. "NOvA Cross-Section Modeling Internal Technical Note For Production 5.1". located on private NOvA server. 2024. URL: nova-docdb.fnal.gov/cgi-bin/private/RetrieveFile?docid=61559&filename=NOvA_Cross_Section_Modeling_Technote_For_Production_5_1_v5.pdf&version=8.

[43] J. Wolcott and K. Bays. "Cross section central value tune and uncertainties for the 2017 analyses". located on private NOvA server. 2017. URL: nova-docdb.fnal.gov/cgi-bin/private/ShowDocument?docid=23264.

[44] K. Abe et al. "Measurement of neutrino and antineutrino oscillations by the T2K experiment including a new additional sample of ν_e interactions at the far detector". In: *Phys. Rev. D* 96.9 (2017). [Erratum: Phys.Rev.D 98, 019902 (2018)], p. 092006. arXiv: 1707.01048 [hep-ex].

[45] Leo (Fermilab) Aliaga and the Beam Group. "NuMI Beam Prediction for the NOvA 2017 Analyses". located on private NOvA server. 2017. URL: nova-docdb.fnal.gov/cgi-bin/private/RetrieveFile?docid=23441&filename=PPFX_technote.pdf&version=4.

[46] Z. Kohley et al. “Modeling interactions of intermediate-energy neutrons in a plastic scintillator array with Geant4”. In: *Nucl. Instrum. Meth. A* 682 (2012), pp. 59–65.

[47] B. Shivam Bhuyan and A. Norrick. “MEC Systematics for the joint FHC-RHC Analysis”. located on private NOvA server. 2024. URL: nova-docdb.fnal.gov/cgi-bin/private/RetrieveFile?docid=64481&filename=MECWeights_technote_v3.pdf&version=3.

[48] Teppei Katori. “Meson Exchange Current (MEC) Models in Neutrino Interaction Generators”. In: 1663 (Apr. 2013).

[49] S. Dolan, G. D. Megias, and S. Bolognesi. “Implementation of the SuSAv2-meson exchange current 1p1h and 2p2h models in GENIE and analysis of nuclear effects in T2K measurements”. In: *Phys. Rev. D* 101 (3 Feb. 2020), p. 033003. URL: link.aps.org/doi/10.1103/PhysRevD.101.033003.

[50] J. Nieves, I. Ruiz Simo, and M. J. Vicente Vacas. “Inclusive Charged–Current Neutrino–Nucleus Reactions”. In: *Phys. Rev. C* 83 (2011), p. 045501. arXiv: 1102.2777 [hep-ph].

[51] M. A. Acero et al. “Measurement of d2σ/d—q→—dEavail in charged current $\nu\mu$-nucleus interactions at <Eν>=1.86 GeV using the NOvA Near Detector”. In: *Phys. Rev. D* 111.5 (2025), p. 052009. arXiv: 2410.05526 [hep-ex].

[52] M. V. Ascencio et al. “Measurement of inclusive charged-current $\nu\mu$ scattering on hydrocarbon at <Eν>∼6 GeV with low three-momentum transfer”. In: *Phys. Rev. D* 106.3 (2022), p. 032001. arXiv: 2110.13372 [hep-ex].

[53] K. Abe et al. “First measurement of muon neutrino charged-current interactions on hydrocarbon without pions in the final state using multiple detectors with correlated energy spectra at T2K”. In: *Phys. Rev. D* 108.11 (2023), p. 112009. arXiv: 2303.14228 [hep-ex].

[54] P. Abratenko et al. “Multidifferential cross section measurements of $\nu\mu$-argon quasielasticlike reactions with the MicroBooNE detector”. In: *Phys. Rev. D* 108.5 (2023), p. 053002. arXiv: 2301.03700 [hep-ex].